NASA CR-72066

EXTREME VACUUM TECHNOLOGY INCLUDING CRYOPUMP, GETTER-ION PUMP, DIFFUSION PUMP AND PRESSURE STANDARDIZATION STUDIES

by

Paul J. Bryant and Charles M. Gosselin

prepared for

NATIONAL AERONAUTICS AND SPACE ADMINISTRATION

CONTRACT NAS 3-8914

MIDWEST RESEARCH INSTITUTE
425 VOLKER BOULEVARD/KANSAS CITY, MISSOURI 64110/AC 816 LO 1-0202

Requests for copies of this report should be referred to

National Aeronautics and Space Administration
Office of Scientific and Technical Information
Attention: AFSS-A
Washington, D.C. 20546

NASA CR-72066

SUMMARY TECHNICAL REPORT

EXTREME VACUUM TECHNOLOGY INCLUDING CRYOPUMP, GETTER-ION PUMP, DIFFUSION PUMP AND PRESSURE STANDARDIZATION STUDIES

by

Paul J. Bryant and Charles M. Gosselin

prepared for

NATIONAL AERONAUTICS AND SPACE ADMINISTRATION

17 July 1967

CONTRACT NAS 3-8914

Technical Management
NASA Lewis Research Center
Cleveland, Ohio
Spacecraft Technology Division
Daniel C. Briehl

MIDWEST RESEARCH INSTITUTE
425 Volker Boulevard
Kansas City, Missouri 64111

PREFACE

The subject of this report is the development of extreme vacuum technology including UHV pumping techniques and UHV pressure measurement techniques. The program, which has been supported by NASA under Contract No. NAS3-8914, was monitored by Mr. D. Briehl of the NASA - Lewis Research Center. This report describes the research accomplished during the period 16 June 1966 - 16 June 1967. However, for the sake of completeness, selected material on gauge characteristics and data on a dual-expansion diffusion pump nozzle have been included in this report although they have previously been reported in a Summary Technical Report dated 31 March 1966, under Contract NASr-63(06).

The program was conducted in the Physics Section of Midwest Research Institute under the direction of Mr. Gordon Gross, Physics Section Head, and Dr. Paul J. Bryant, Project Leader. Mr. Charles Gosselin and Mr. Gerald Swanson have contributed significantly to the successful completion of this program. Dr. William W. Longley has been of great help with his comments and critical analysis of this work during frequent discussions.

Approved for:

MIDWEST RESEARCH INSTITUTE

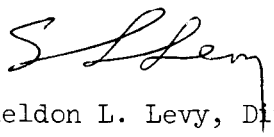

Sheldon L. Levy, Director
Mathematics and Physics Division

17 July 1967

jd

TABLE OF CONTENTS

TABLE OF CONTENTS (Continued)

List of Figures

TABLE OF CONTENTS (Continued)

List of Figures

TABLE OF CONTENTS (Concluded)

List of Figures

EXTREME VACUUM TECHNOLOGY INCLUDING CRYOPUMP, GETTER-ION PUMP, DIFFUSION PUMP AND PRESSURE STANDARDIZATION STUDIES

by

Paul J. Bryant and Charles M. Gosselin

ABSTRACT

The program reported here is divided into two major areas of concern: UHV pumping techniques and UHV pressure measurement. In the pumping technique studies gross cryopumping capacities for helium and hydrogen on type 304 stainless steel were determined, getter-ion pumping mechanisms were studied, and diffusion pump nozzle designs were investigated. In the pressure measurement studies an independent pressure reference employing an electron field emission microscope was established and the ion current vs. pressure response curves were determined for three commercial cold cathode gauges; NRC type 552, GCA Model 1410, and G. E. 22 CT 214.

SUMMARY

This report reviews the results of the two phases of work, UHV pumping and UHV pressure measurement. The pumping studies include cryopumping, getter-ion pumping, and diffusion pumping. The UHV pressure measuring studies include a verification of low pressure measurements, and selected gauge calibrations.

Cryopumping

The cryosorption studies have included the simplification of a physical absorption isotherm theory based on a triangular site model, the development of a quartz crystal oscillation microbalance, and the development of a technique to correlate gross cryopumping capacity to equilibrium pressure above a cryopumping surface. Data for helium and hydrogen adsorbed on a surface (304 S.S.) maintained at 4.2°K and near 20°K, respectively, are presented. The data indicate that the equilibrium pressure above the cryosurface begins a rapid increase at approximately one-half monolayer coverage. Also residual gas analysis has been conducted for the cryopumped system and is presented.

Getter-Ion Pumping

The pumping characteristics of Penning cells have been investigated as a function of pressure and of the cathode to anode voltage. A fundamental study of Penning discharge phenomena and a detailed study of the pumping effect for various gas species has been included. An experimental Penning cell has been fabricated and employed to measure geometric changes in the discharge activity as a function of pressure. The observed variance in discharge activity has been related to the mode change reported by Rutherford for getter-ion pumps and to the sensitivity change observed in pressure measuring devices employing Penning discharges.

Diffusion Pumping

Improved operation of a diffusion pump has been obtained by means of a dual expansion nozzle. The special nozzle design permits operation of a diffusion pump at higher vapor jet densities without the loss of pumping speed. Thus lower back diffusion rates can be maintained. This technique will be of particular value in multi-stage diffusion pumps where interstage desorption limits the net pumping speed.

Independent Verification of Low Pressure Measurements

Extreme vacuum measurement techniques have been placed on a firmer footing by the use of an electron field emission microscope to determine strike rates of molecules at pressures in the 10^{-9} torr range. The field emission microscope experiment described has been performed at xenon pressures in the 1.3 to 7.9 x 10^{-9} torr range. Agreement between the striking rates and vacuum gauge response has been found in the pressure range studied.

Selected Gauge Calibration

The ion current vs. pressure response curves for the Redhead (NRC Type 552), Kreisman (GCA Model 1410), and Trigger Discharge (GE 22 CT 214) are presented. Also a discussion of characteristics of the response curves based on an investigation of Penning discharge phenomena is included.

I. INTRODUCTION

The field of applied vacuum technology can be divided into two major areas of concern, (1) the production of vacuum environments and (2) the measurement of the degree of evacuation which exists within each environment. The extreme-vacuum technology research program at MRI has investigated aspects of each of these areas of concern. The studies related to evacuation deal with three pumping techniques: cryogenic, getter-ion, and diffusion. The studies related to the measurement of low pressure deal with the development of methods to independently verify the levels of evacuation as indicated by present gauging techniques and the determination of the ion current to pressure response curves for the three commercial gauges employing Penning discharges.

Cryogenic Pumping

In general, extremely low pressures ($<10^{-12}$ torr) are achieved primarily by cryopumping techniques. However, this method of pumping is limited in that only a certain quantity of gas can be absorbed onto a cryopanel before the panel becomes saturated and can no longer maintain a low pressure above its surface. Consequently, the gross cryopumping capacity for specific gases is of interest to people designing and using cryopumps. Therefore, our studies have endeavored to determine the gross cryopumping capacity of type 304 stainless steel for He and H_2 and to determine the composition of residual gases which are found in metal cryogenically pumped vacuum systems.

Getter-Ion Pumping

The technique of getter-ion pumping has proved to be a valuable means of producing evacuation in the high and ultrahigh vacuum (UHV) ranges. A review of the getter-ion technique reveals that two major processes occur. Gas molecules are pumped either as neutral gas species or as gas ions. The first process is not directly dependent on the discharge activity (although it does depend on the condition of the gettering surfaces resulting from ion bombardment sputtering) and is relatively independent of pressure in the UHV range. The second process (ion pumping) is dependent on the discharge activity within the pump which, in turn, varies with pressure in the UHV range.

Since a getter-ion pump is basically an array of Penning cells (with gettering material on the cathodes), the discharge phenomenon follows the characteristic Penning discharge behavior. This type of discharge forms a virtual cathode (Ref. 1) (a dense electron cloud) between the end plates of the cell when operating in the high vacuum range (above 10^{-8} torr). However, if the pressure is lowered, a range is reached in which the virtual cathode is not sustained. The characteristics of the Penning discharge in this pressure range ($<10^{-8}$ torr) have not been well known, and, therefore, the potentialities and limitations of this phenomenon have not been well established. These characteristics were investigated during this research program, and substantial insights into the pumping mechanisms and limitations of getter-ion pumps have been gained.

Diffusion Pumping

The pumping effect of the diffusion pump is based on a transfer of momentum from the expanding jet (1) to incoming molecules from a vacuum chamber, and (2) to gas molecules which are back-diffusing through the jet region into the vacuum chamber. The vector sense of the momentum transfer is such that the direction of gas flow is established away from the vacuum chamber.

The first process, which amounts to molecule entrainment by the vapor jet, determines the pumping speed. The critical parameter in this operation is the degree of uniformity with which momentum is transferred from the vapor jet to incoming gas molecules. This is particularly true at the upper boundary of the jet where the incoming gas first encounters the vapor stream. If there is turbulence at this boundary, significant amounts of gas can be repelled back into the vacuum chamber. The amount of such turbulence is a function of nozzle design and vapor density, i.e., lower density jets generate less turbulence.

The second process, back diffusion, determines the pressure drop which can be maintained across the vapor jet. Back-diffusion reduction is highly dependent on jet vapor density, i.e., higher-density jets can maintain a greater pressure differential than low density jets.

A dilemma arises when back diffusion is reduced by increasing boiler pressure, because the corresponding increase of turbulence in the vapor jet reduces the ability to entrain gases. It has been postulated that a dual expansion nozzle would aid in resolving the dilemma (Refs. 2 and 3). Such a nozzle should generate a high-density main jet surrounded by a low-density umbrella jet. Therefore, one of the purposes of the present work has been to determine the relative pumping efficiency of a dual expansion nozzle versus a single expansion nozzle.

Independent Verification of Low-Pressure Measurement

Pressure is defined as the force per unit area exerted on a surface. In the field of vacuum measurement, pressure can be measured directly down to a level of approximately 10^{-5} torr. Below this level no practical direct pressure measurement techniques exist and molecular densities are generally measured to determine the degree of evacuation. Therefore, calibration procedures have been developed which are not based on direct pressure measurements, but rather on physical-system processes.

One such process is used in the pressure-ratio technique, in which two gauges are mounted in separate vacuum chambers and connected via a known conductance. A test gas is introduced into one of the chambers and is permitted to flow through the conductor between the chamber into the second chamber, and then pumped out of the system. This flow condition establishes a pressure differential between the chambers. It can be argued that the upstream pressure is related to the downstream pressure via the flow conditions. Therefore, calibration of gauges should be extendable from a direct-pressure measurement range to molecular-density measurement ranges via a system of sequential pressure ratio experiments. However, vacuum gauges are subject to various spurious effects such as photo-generated background currents, changes in sensitivity with molecular densities and gas species, ion desorption, and other effects depending on the operational history of a particular gauge. Since all these effects can bias a vacuum gauge measurement, it is desirable to establish a method which is independent of vacuum gauges to verify molecular-density measurements.

A way in which molecular densities can be determined directly is by determining the molecular striking rate per unit area on the surfaces of a vacuum system. One technique to determine this striking rate is to observe the image patterns of an electron field emission microscope (FEM).

During this program we have attempted to correlate the spot pattern of the FEM to pressures in the 10^{-9} torr range, thus providing increased confidence in such calibration techniques as the pressure-ratio technique described above.

Gauge Calibration

In the present state of the art in vacuum technology it is possible to produce pressures at levels below the operational limits of available vacuum gauges. Since gauges are now required to function near their operational limit, it is of prime importance to establish their respective operational limits and their response characteristics (ion current vs. pressure). We have applied the pressure-ratio technique described above to three commercial gauges which employ Penning type discharges. In this work we have correlated the experimental and theoretical aspects of the Penning discharge.

II. PUMPING TECHNIQUES FOR UHV APPLICATION INCLUDING CRYOPUMPING, GETTER-ION PUMPING, AND DIFFUSION PUMPING

Three UHV pumping techniques, cryogenic, getter-ion, and diffusion, have been investigated by both theoretical and empirical studies. These studies have included; the development of an adsorption isotherm theory for physical adsorption on cryogenically cooled surfaces, the measurement of selected gross cryopumping capacities, an investigation of the residual gases in both a cryopumped and getter-ion pumped system, an investigation of Penning discharge phenomena as a function of pressure and applied voltage, an investigation of the effect of Penning type discharge activity on the pumping of various gas species, and the investigation of dual-expansion nozzle for use in diffusion pumps.

A. Cryosorption Studies Including Gross Cryopumping Capacity Data and Residual Gas Analysis

The triangular site physical adsorption isotherm theory developed on this program earlier (Refs. 3, 4 and 5) has been simplified by an approximation which has resulted in reducing the computer time needed in fitting the theoretical curves to adsorption data. The study includes the development of a special piezoelectric crystal oscillator which is used as a sensitive microbalance and the experimental techniques employed. The data which have been collected with the piezoelectric crystal are difficult to interpret because the crystal response does not display a clear relationship to system

pressure. However, a second technique, (Section II-A-3) which employs the sequential adsorption of discrete quantities of gas has been used to obtain gross cryopumping capacity data for He and H_2 on stainless steel (Type 304) cryopanels.

1. Physical adsorption isotherm theory: Although the physical adsorption isotherm theory developed earlier[3,5] has many useful features, it is not convenient to use in interpreting experimental data. Therefore, the theory was modified in that an assumption was made that at most two layers are active at any time. Both the triangular site model, as shown in Figure 1, and the interaction between absorbed molecules were retained. For completeness, the theoretical isotherm equations have been specialized to the Lennard-Jones 6-12 intermolecular potential and closest packing of the adsorbed atoms (in previous notation this infers that R' = R). Development of the isotherm is briefly summarized below.

Let the intermolecular potential between two adsorbed atoms be given by

$$\varphi(\rho) = 4\epsilon\left[\left(\frac{\sigma}{r}\right)^{12} - \left(\frac{\sigma}{r}\right)^{6}\right] \qquad (1)$$

where r is the distance between the molecules, ϵ is the maximum energy of attraction of the two atoms, and $R = 2^{1/6}\sigma$ is the equilibrium distance between the atoms as shown in Figure 2. All energies will actually be divided by the Boltzmann's constant and expressed as degrees Kelvin. Equation (1) can be integrated over the various layers to give effective interaction energies which exclude the nearest neighbor interactions:

$$z(r) = 4\pi\epsilon\sigma_o r^2\left[\frac{1}{4}\left(\frac{\sigma}{r}\right)^{6} - \frac{1}{10}\left(\frac{\sigma}{r}\right)^{12}\right] \quad , \quad \sigma_o = \frac{1.1547}{R^2} \qquad (2)$$

where the values of r to be used (see Figure 2) are given by

$$w = \left(\frac{\pi\sigma_o R^2}{4}\right)^{1/4}\sqrt{3}\ R \quad ,$$

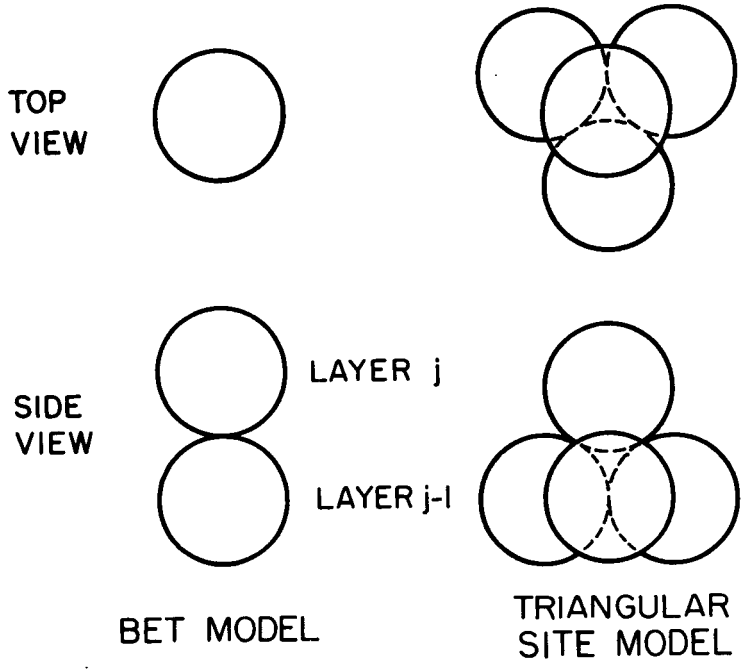

Figure 1 - Adsorption Site Models for the Atomic Arrangement Used in the Development of the BET Theory (left) and Triangular Site Model (right).

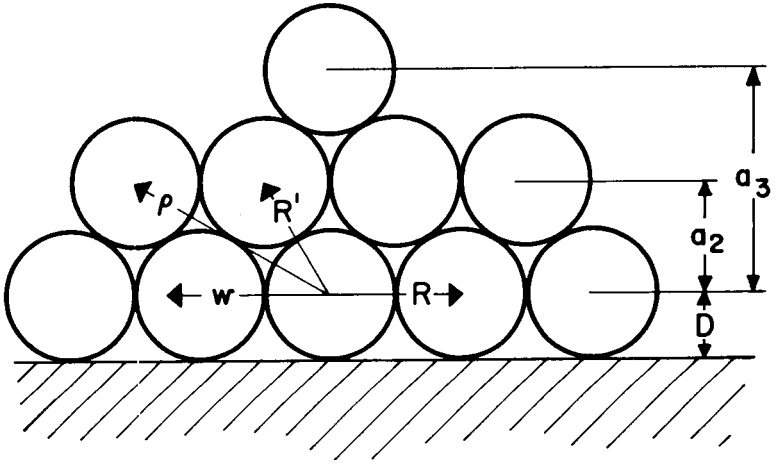

Figure 2 - Adsorption Geometry for the Triangular Model Showing: Nearest and Next Nearest Neighbor, and Interlayer Spacings; and First Adsorbed to Adsorbent Spacing, D.

$$a = 0.81649\ R \quad , \quad a_j = (j-1)a \quad ,$$

$$\rho = \left[\frac{\pi\sigma_o(4R^2+3a^2)}{18}\right]^{1/4} \sqrt{\frac{4}{3}R^2+a^2} \quad . \tag{3}$$

The nearest neighbor interaction energy is simply ϵ per pair interaction.

The interaction between an adsorbed atom and the adsorbent is treated as above with the energy for an atom in the first layer being given by

$$W_s = 10\ \pi\epsilon_s N_o\ D^3/9 \quad , \quad D = (0.4)^{1/6}\sigma_s \tag{4}$$

where N_o is the number of adsorbent atoms per unit volume and ϵ_s , σ_s are analogous to ϵ , σ , respectively. For the j^{th} layer this energy becomes

$$W_{sj} = \frac{W_s}{6}\left[\frac{9}{(1+d_j)^3} - \frac{3}{(1+d_j)^9}\right] \quad , \quad d_j = a_j/D \quad . \tag{5}$$

Using θ_j for the fractional occupancy of the j^{th} layer, the effective adsorption energy, E_j , can be written as

$$E_j = W_{sj} + 2P_{j-1}\epsilon + \frac{1}{2}(3+P_{j-1}\theta_{j-1}/\theta_j)f_j'\epsilon - \sum_{i=j+1}^{J}\frac{2^{i-j-1}\theta_i(P_{i-1}+P_i)\epsilon}{\theta_j}$$

$$+ 2\theta_j z(w) + 2(f_j'\theta_{j-1}+\theta_{j+1})z(\rho)+2\sum_{i=1}^{j-2}\theta_i z(a_j-a_i)+2\sum_{i=j+2}^{J}\theta_i z(a_i-a_j) \tag{6}$$

where $f_j' = 1 - \delta_j'$, $P_j = \frac{\theta_{j+1}}{3\theta_j^3}P_{j-1}^2$, $P_o = 3\theta_1$ is a probability function for determining the likelihood of nearest neighbors and j is the number of the top layer.

Let

$$\gamma_j = (KM^{3/2}\, T^{5/2}/p)\, \exp(-E_j/T) \qquad (7)$$

where $K = 0.0256054$, M is the atomic mass of an adsorbed atom, T is the absolute temperature, and p is the gas pressure in torr. The isotherm can then be calculated by iterating the j functions

$$\theta_j = \theta_{j-1}^3 \left[1+\gamma_j \left(1-\theta_{j+1}\theta_j^{-3}\right)^{3\theta_j^2} \right]^{-1} \quad , \ \theta_0 = 1 \quad , \qquad (8)$$

and summing over j to give the total number of adsorbed monolayers, θ .

The above equations yield isotherms which can exhibit discrete steps or can be quite smooth (Ref. 5). However, the equations are complicated and necessitate long computer times for their evaluation. An approximation which retains the essentials of the theory but needs only short computer times is the two-active layer approximation (the TAL theory). The TAL theory sets all N values of θ_j greater than, say, 0.99 equal to 1 exactly and assumes that there are only two layers, the $N+1$ and the $N+2$ layers, which have θ_j values between 0 and 1 . The exact theory then reduces to a much simpler system. Let

$$V_{N+1} = W_{s,N+1} + \left[2 \sum_{i=1}^{N-1} z(a_j-a_i) + 3\epsilon + 2z(\rho) \right] f'_{N+1} \quad ,$$

$$U_{N+2} = W_{s,N+2} + 2 \sum_{i=1}^{N} z(a_j-a_i) + 3\epsilon \quad , \qquad (9)$$

then the TAL theory is given by Eq. (8) for $j = N+1$ and $N+2$ and the coverage and effective adsorption energies

$$\theta = N + \theta_{N+1} + \theta_{N+2} \quad ,$$

$$E_{N+1} = V_{N+1} + \left[2\theta_{N+1} - \left(\frac{\theta_{N+2}}{\theta_{N+1}} \right)^2 \right] 3\epsilon + 2\theta_{N+1} z(w) + 2\theta_{N+2} z(\rho) \quad ,$$

$$E_{N+2} = U_{N+2} + 6 \frac{\theta_{N+2}}{\theta_{N+1}} \epsilon + 2\theta_{N+1} z(\rho) + 2\theta_{N+2} z(w) \quad . \qquad (10)$$

This TAL theory still produces either the discrete steps or smooth isotherms depending on temperature, W_s , E , and θ .

Because the TAL theory requires a short computation time it was employed to develop a series of coverage-vs-pressure curves for various temperatures, W_s , and D values. These curves were made to fit the preliminary data obtained with the microbalance technique (II-A-2). Although the initial data were not as expected, the best fit suggested that a crystal temperature near 12°K was limiting the data collection and that the low W_s value could only result from a contaminated surface. However, improved experimental techniques did not produce interpretable data. The theory can be applied best when the experimental data show a step or series of steps in coverage at definable pressures.

2. Piezoelectric crystal employed for sensitive adsorption measurement: A special piezoelectric crystal oscillator was developed for use as a microbalance to measure the progressive loading of adsorbed layers as the pressure was gradually increased. The total pressure and the crystal's vibrational frequency, which should decrease in proportion to the amount of adsorbed material, were monitored during a series of experiments. However, no satisfactory relationship could be deduced between the system pressure and the crystal frequency shifts. Therefore, another technique which was developed to collect gross cryopumping data for He and H_2 on type 304 stainless steel is discussed in Section II-A-3.

The equipment needed to perform an adsorption isotherm measurement via the piezoelectric crystal technique is described here under two major categories: (a) environmental, and (b) electronic.

(a) The environmental equipment requirements are determined by the following operational conditions: (1) the quartz crystal surfaces and its electrodes must be maintained in a noncontaminating atmosphere, viz., ultrahigh vacuum; (2) the crystal must be maintained at a constant temperature, the level of which is established for the isotherm to be

determined, and (3) an adequate source of test gas must be supplied for the range of adsorption phenomena to be studied.

A UHV system incorporating the above requirement has been fabricated. The system consists of a crystal chamber (1-1/2 in. diameter by 20 in. long), a specially designed coaxial vacuum feedthrough unit to which the quartz crystal is attached, gas inlet system and associated vacuum plumbing. This system is attached to the Partial Pressure Analyzer System (PPAS) (Ref. 3) via a bakeable high conductance isolation valve. Both the UHV pumping facilities of the PPAS and its gas analysis capabilities are utilized. The entire system is bakeable to 400°C and can maintain a pressure of 1×10^{-9} torr with only the 8 liter/sec getter-ion pump operating. Analysis of the residual gas in this system indicates that H_2 and CO are the major constituents and that all other gases have partial pressures below 1×10^{-10} torr.

The temperature of the crystal is established by submerging the crystal zone (the lower 10 in. of the crystal chamber) into a dewar of liquid helium. To avoid excessive boil-off of the cryogenic liquid, the lower end of the crystal chamber is fabricated from glass (see Figure 3). The dewar mounting is such that a mechanical vacuum pump can be used to vary the pressure above the cryogenic liquid thus making some temperature variance possible.

The quartz crystal can be mounted directly at the end of two specially designed coaxial leads as shown in Figure 4, or by means of two kovar support rods as shown in Figure 5. The coaxial leads are fabricated from thin-wall stainless steel tubing with ceramic insulators at various positions along their 22-in. length. Outgassing slots have been cut in both the outer and inner tubes.

Figure 4b shows in detail the lower end of the coaxial leads. A platform is fixed between the outer tubes and supports a system of carefully positioned beryllium copper leaf springs which press against the tubular wall of the vacuum chamber. The springs are arranged in a spiral staircase configuration such that the array is optically dense, but maintains a high conductance value for gas flow. This assembly performs two functions: it shields the crystal chamber from radiation from the warmer parts of the vacuum system, and it conducts heat from the coaxial leads to the cryogenically cooled vacuum finger wall. The cryogenic liquid level is maintained at a point at least 2 in. above the spring assembly during data collection periods. Thus, in operation the crystal is surrounded by cold surfaces. Note the crystal does not cool as rapidly as the vacuum vessel walls which are in direct contact with cryogenic fluids. Therefore, when LHe is used, contaminating gases are trapped on the vacuum chamber walls before the crystal can begin significant adsorption.

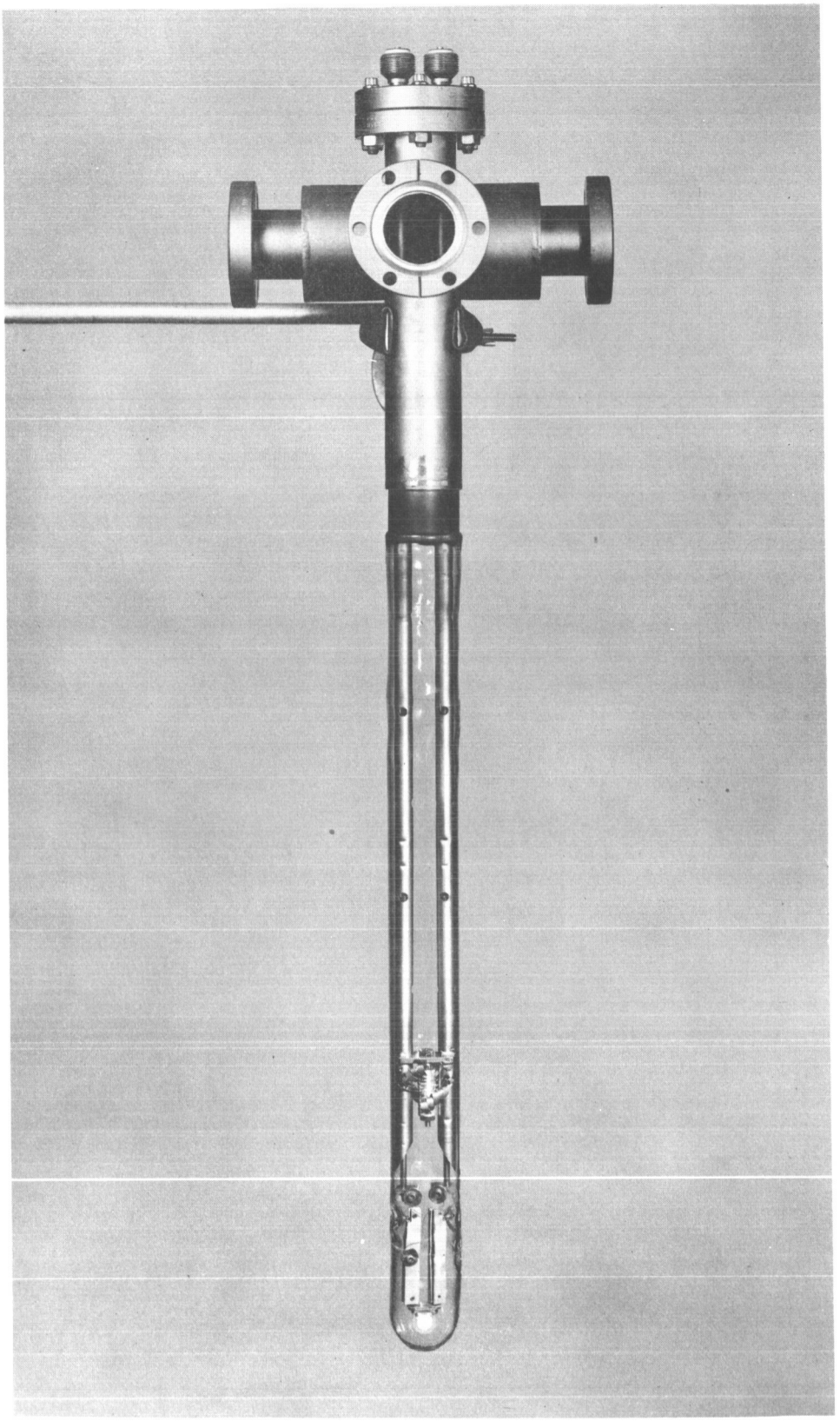

Figure 3 - Glass Cryofinger Used to House Piezoelectric Crystal (Microbalance) During Adsorption Experiments. The lower end of the cryofinger is submerged into a dewar of liquid helium (LHe) during an experiment and it is evacuated via the stainless steel vacuum manifold at the top of the photograph. The vacuum gauges used to monitor pressure are attached to the manifold during an adsorption run.

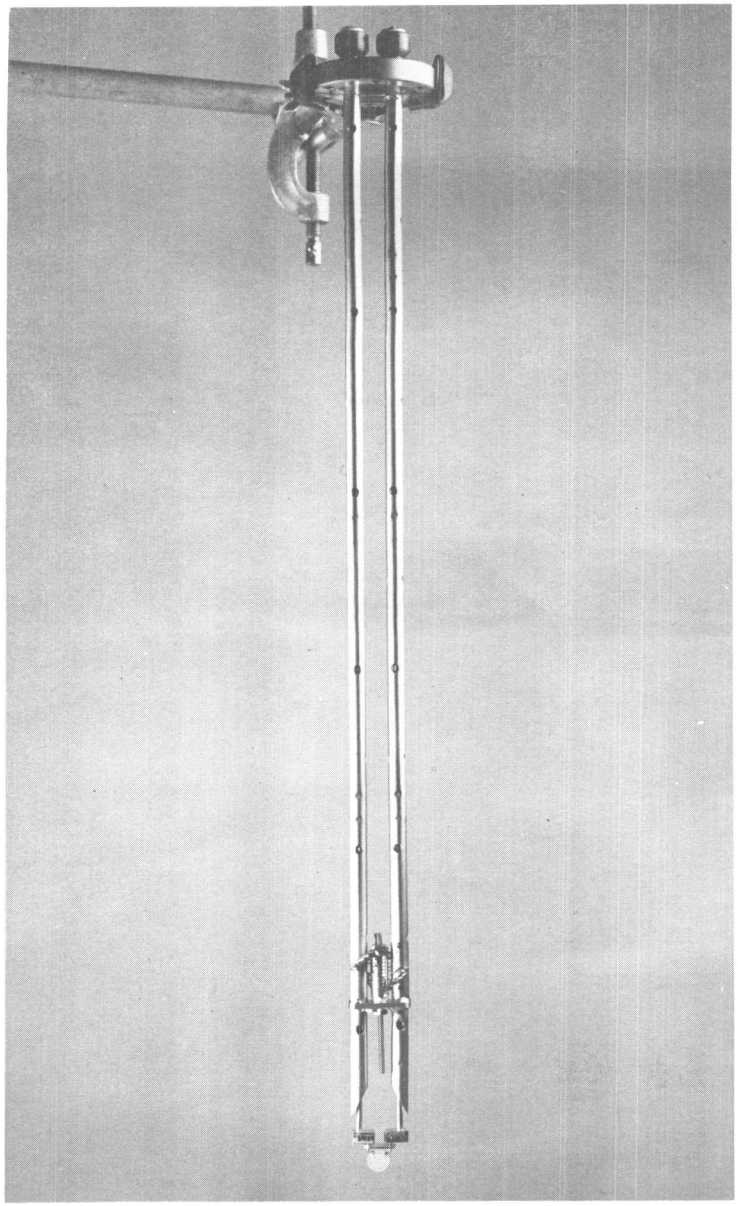

Figure 4a - Coaxial Vacuum Lead Assembly on which Quartz Crystals are Mounted. Leads are fabricated from thin wall stainless steel tubing and have been slotted to insure thorough outgassing during bake periods.

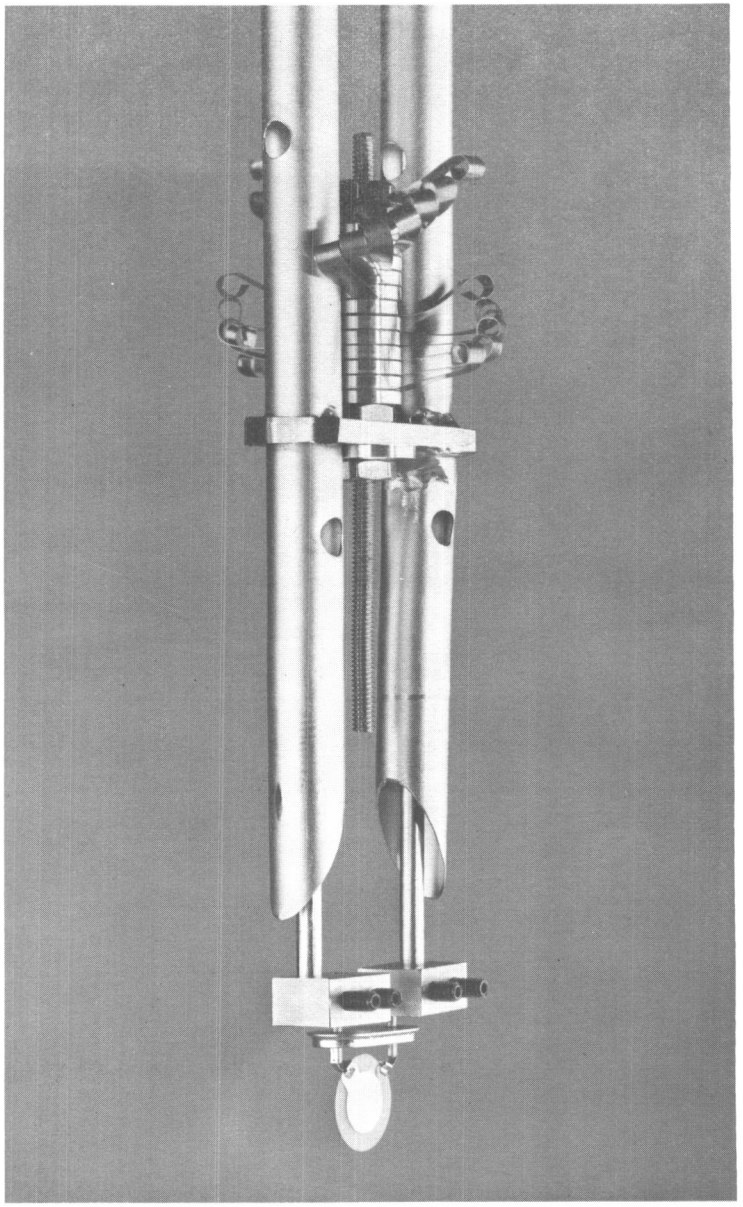

Figure 4b - Initial Crystal Mounting to Lower End of Coaxial Vacuum Leads. A beryllium copper spring assembly establishes thermal conduction to the cryofinger wall and forms a radiation shield.

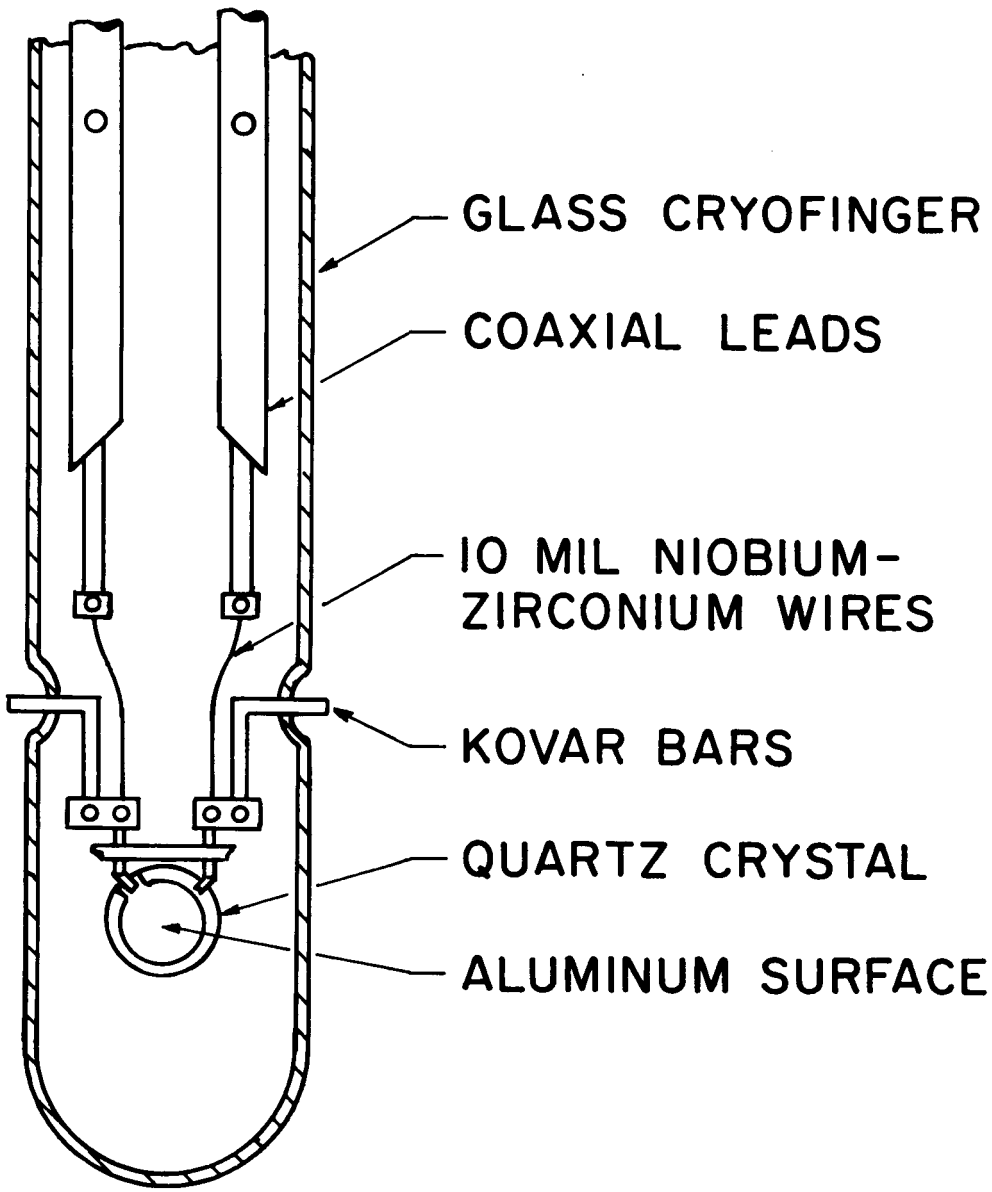

Figure 5 - Modified Quartz Crystal Mounting Technique. To insure lower crystal temperature the glass cryofinger is submerged into a dewar of liquid helium (LHe). The Kovar bars which penetrate the glass wall are in direct contact with the LHe.

Chronologically the crystal was first mounted as described in Figure 4. However, as data were collected it became apparent that the crystal was not responding as expected to helium gas pressure changes. Comparison of the data to theoretical predictions indicated that the crystal was not at 4.2°K, but possibly as high as 12°K. Therefore, the second method of crystal mounting, see Figure 5, was used for later experiments. The second method employs crystal mounting rods which penetrate the glass wall of the vacuum chamber and thus provide improved thermal contact between the LHe and the crystal. Electrical connections are completed between the kovar mounting rods and the coaxial assembly described above via 0.010 in. diameter Nb-Zr wire. This wire becomes superconducting at $\sim$ 13°K and has poor thermal conductivity.

When the vacuum finger is cooled to LHe temperature and the isolation valve is closed thus eliminating all pumps from the system except for the ion gauge and cryofinger, the air-equivalent pressure in the room temperature part of the system is 1×10^{-10} torr or lower. Using a thermal transpiration correction it is determined that the pressure in the crystal zone is below 1×10^{-11} torr. This pressure level for contaminating gases is sufficiently low to present no significant effect on the adsorption measurement. After an equilibrium condition is established for pressure, temperature, and crystal frequency, a test gas is admitted to the crystal chamber. Since this study deals with the adsorption of helium onto liquid helium temperature surfaces, a 6-in. vycor diffuser is used for the gas inlet system. The pressure can be slowly raised in the system by gradually increasing the diffuser operation up to a maximum level of 0.1 micron liter/sec.

(b) The electronic equipment requirements are determined by the following needs: (1) a 5 Mc oscillator system with which to operate the microbalance, and (2) a data detection and recording system.

A stable 5 Mc oscillator system has been reported by P. A. Simpson and A. H. Morgan (Ref. 6). Based on their design a similar system was assembled for this set of experiments and a schematic diagram is shown in Figure 6. Care was taken in the layout of components to shield one stage from another, as is shown by the dashed lines in the diagram. Basically the system consists of a 5 Mc crystal controlled oscillator circuit followed by a single stage amplifier which delivers a signal to an automatic gain control circuit (AGC) and to additional amplifier stages. The AGC supplies a feedback loop to the 5 Mc oscillator circuit. The additional stages supply output signals via a discriminator to a digital counter and a microamp meter. The meter is used to monitor the power required to operate the fundamental mode of the crystal. A detailed analysis of this circuit can be found in Ref. 6.

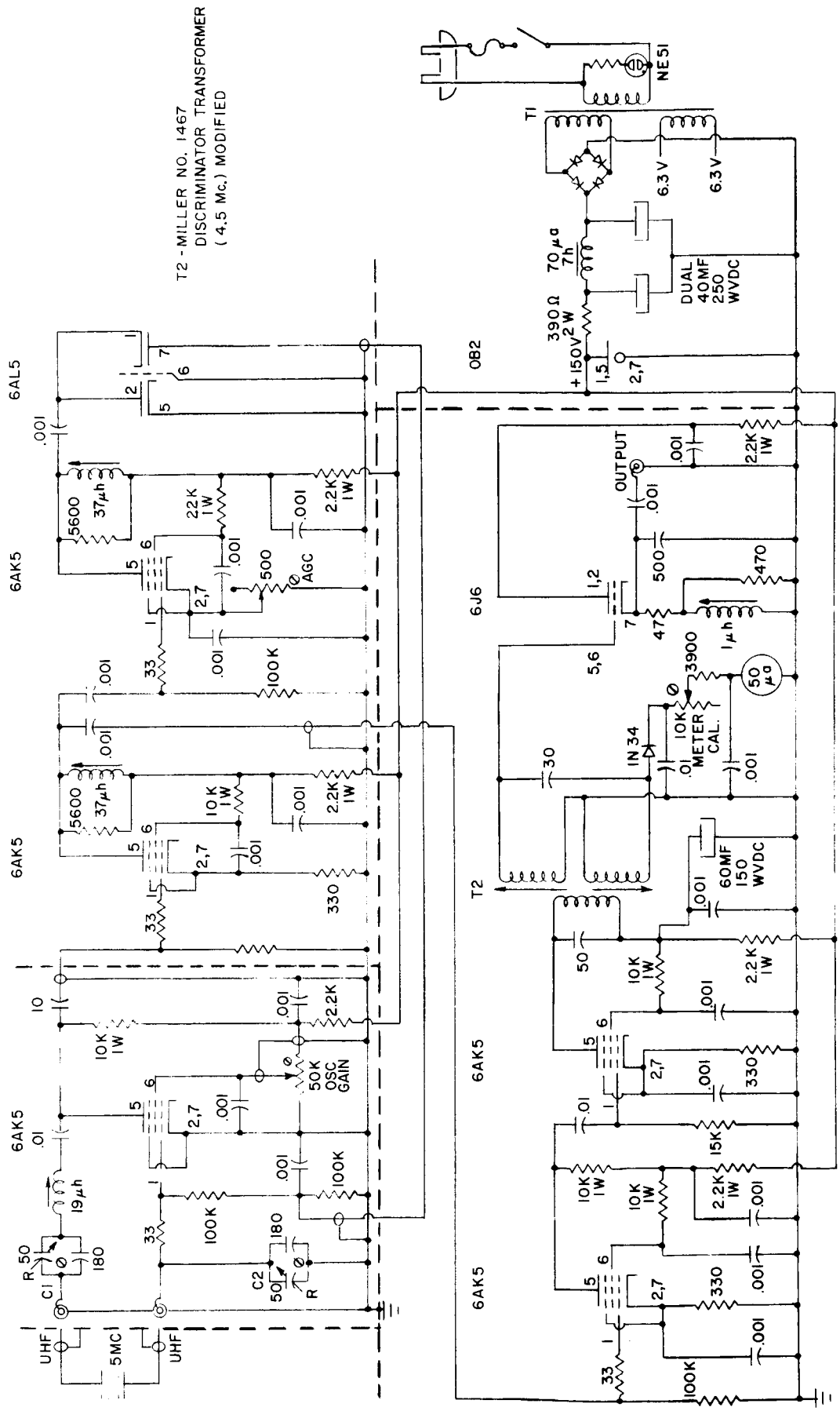

Figure 6 - Schematic Diagram of a Stable 5 Mc. Oscillator (see Ref. 6).

The 5 Mc crystals used in this study were obtained from AT cuts of synthetic quartz and have a 0.550 in. diameter. The edges of the crystal have a slight 20 diopter biconvex bevel. Figure 4 displays a typical crystal mounted on the ends of the specially fabricated coaxial leads. An electrode is deposited on each side of the crystal and each electrode is connected to one of the coaxial leads via a spring clip unit. It has been determined that the crystals and the mounting units continue to function reliably after repeated exposures to the temperature extremes of the experiment, viz., 4°K to 673°K. Silver and aluminum have been used as electrode materials. However, the silver electrodes are not satisfactory because electrical continuity is lost during initial operation. It has been determined that the failure occurs between the clips holding the crystals and the main body of the electrode.

Aluminum electrodes have been tested and found to be satisfactory throughout the entire operational range of pressure and temperature. It should be noted, however, that the effort on this study is not directed toward developing any particular electrode material or geometry. The only interest is to determine the value of the microbalance technique for cryopanel studies. It should be possible to use many conducting materials as electrodes including silver.

A summary of the data collection and recording system is given by the schematic diagram in Figure 7. The system pressure is monitored by a Bayard-Alpert type gauge (BAG), i.e., a Varian UHV-12. Pressure data are fed from the gauge control unit to the y coordinate of an x-y plotter. The frequency at which the oscillator is operating is monitored by a digital counter which feeds frequency data to a digital-to-analog converter. The converter monitors the last three significant figures of the incoming data and generates a signal which is then fed to the x coordinate of the x-y plotter and to a strip chart recorder.

Although the above described electronic data collection system seemed to operate properly, the data were not reproducible. Even after improving the environmental system by incorporating the second crystal mounting technique (see Figure 5), which provides a more certain temperature condition for the crystal, it was determined that no clear relationship could be deduced between the system pressure and crystal response. Therefore, an alternate technique has been used to collect gross cryopumping capacity data for He and H_2 on type 304 stainless steel.

3. Technique to measure gross cryopumping capacities: A technique has been developed by which a known quantity of a test gas can be pumped on to a cryopanel and the equilibrium pressure of the test gas can be monitored as a function of cryopanel coverage. Thus gross cryopumping capacity data can be obtained by data plots of cryopanel coverage vs. equilibrium pressure above the panel.

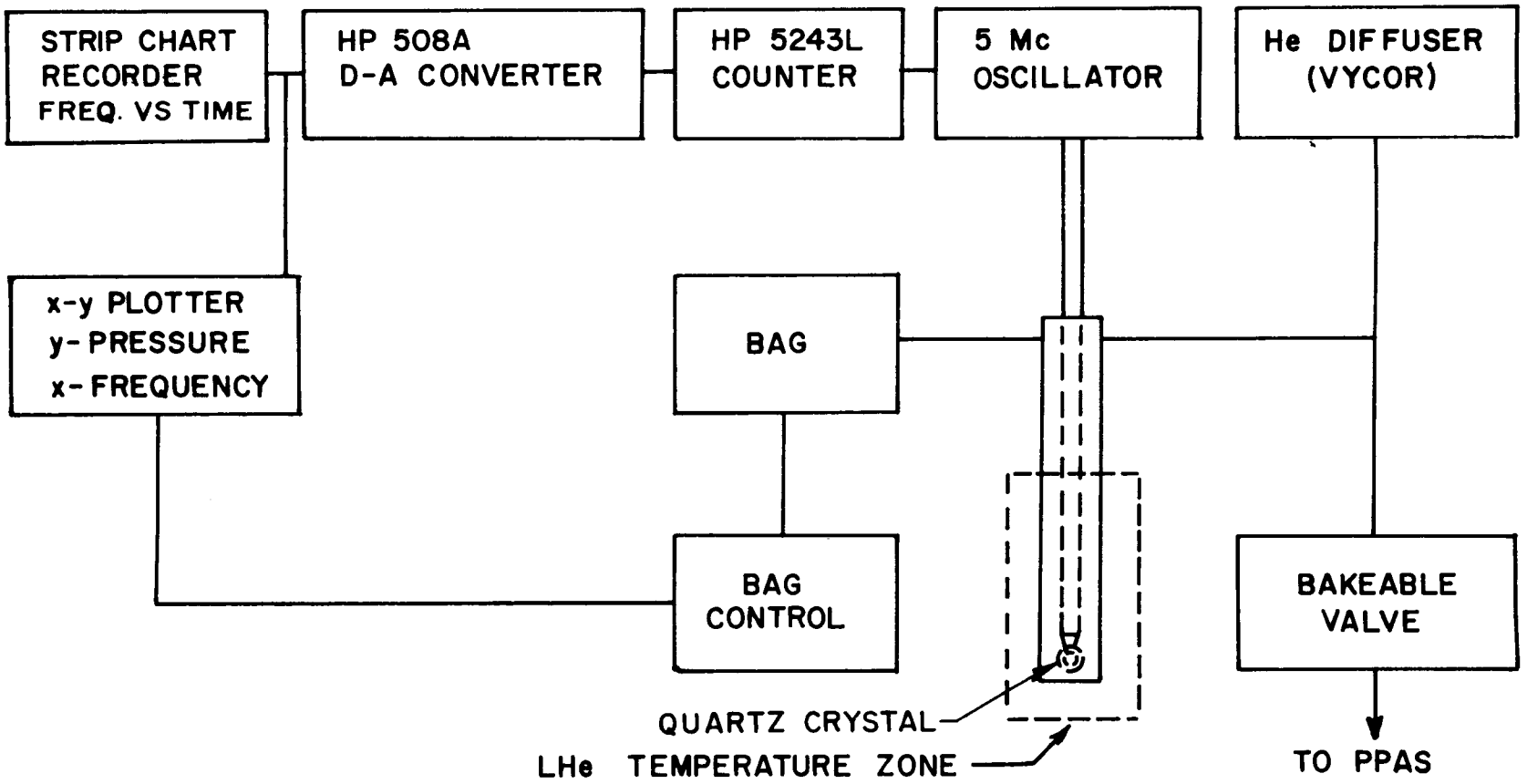

Figure 7 - Block Diagram of the Major Electronic and Environmental Components Used with the Microbalance System. Gas pressure in the system is monitored by a Varian UHV-12 ion gauge (BAG) and plotted on the y coordinate of the x-y plotter. The crystal frequency shift is plotted on the x coordinate.

A special LHe cryofinger was fabricated from type 304 stainless steel and is shown diagrammatically in Figure 8. During an experiment this cryofinger is inserted into a dewar of LHe. The lower portion of the cryofinger comes in contact with the LHe whereas the upper portion is protected by a vacuum jacket. Thus, a fixed pumping area can be maintained as the LHe level rises and falls as long as the level remains in contact with the auxiliary vacuum jacket. The internal surface of the finger has been maintained in an as-supplied state, i.e., no polishing procedures have been used. Therefore, data collected with the cryopump were recorded as a function of projected area, i.e., no corrections for surface roughness were made.

The LHe cryopump is attached to a UHV vacuum system as shown in the block diagram, Figure 9. The test volume, including a UHV gauge and the cryofinger is attached to a reference volume via two paths, viz., a 1-1/2 in. isolation valve and 1-1/2 in. isolation valve in series with a known conductance orifice (0.081 in. thick by 0.250 in. diameter). The conductance values for the orifice at room temperature are 7.8 liters/sec for helium and 11.1 liters/sec for hydrogen. After isolating the test volume from the reference volume He and H_2 are admitted into the reference volume via a vycor diffuser and a palladium diffuser, respectively. A partial pressure analyzer (PPA) (Ref. 3), reference gauge, and UHV diffusion pumping station are also attached to the reference volume. During an operational cycle the entire system is baked to 350° to 400°C for 12 hr. Following the cool down and isolation of the test volume, the background pressure is $\sim 2 \times 10^{-9}$ torr in the reference volume and $\sim 4 \times 10^{-10}$ torr in the test volume. The test volume is pumped by only a nude ionization gauge. A pressure in the 10^{-6} torr range of a test gas is established in the reference volume by activating one of the diffusers and by pumping on the system with the diffusion pump station.

The cryofinger can be operated in two modes (a) submerged directly in LHe and (b) insulated from the LHe by a styrofoam cap and wrapped with a chromel heating element. The latter mode is used to collect data on H_2 at a temperature of $\sim 20°K$. Measured quantities of gas can be admitted into the test volume by opening the valve which is in series with the orifice C. The quantity of gas (Q) admitted is given by the expression:

$$Q = C(P_r - P_t)t \qquad (11)$$

where:

C = conductance of orifice
P_r = pressure in reference volume
P_t = pressure in test volume
t = time the test volume is exposed to the reference volume via C

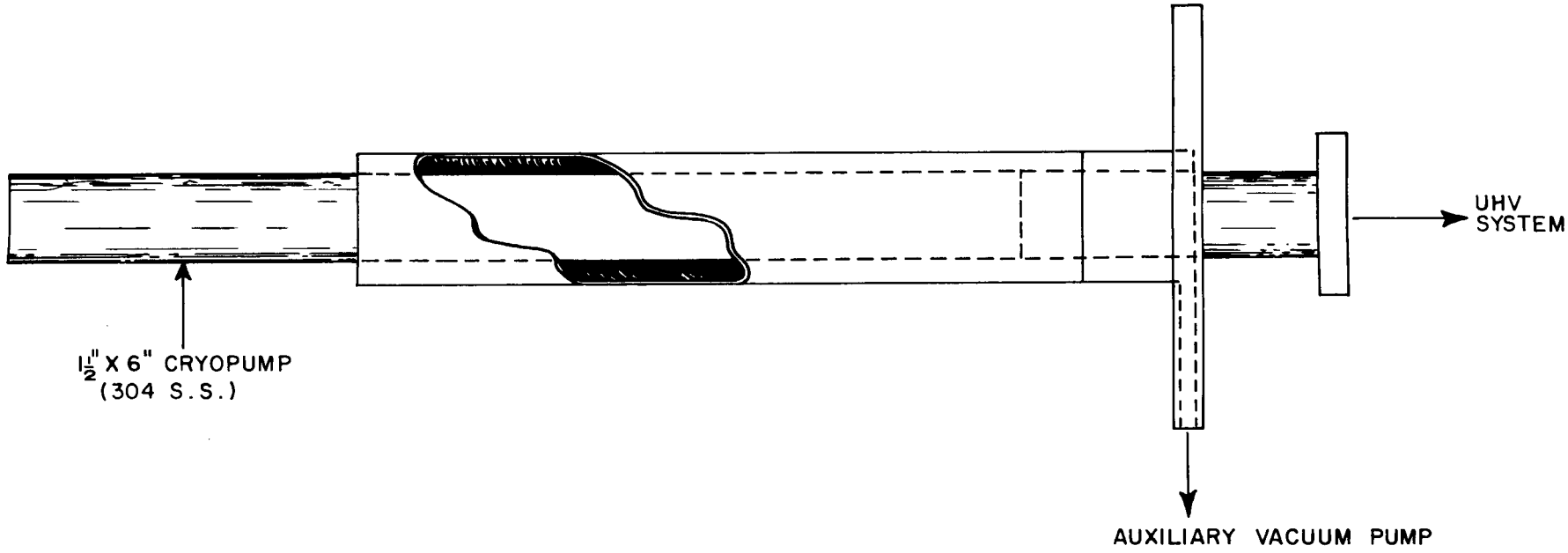

Figure 8 - Special Stainless Steel (Type 304) Cryofinger Used to Measure Gross Cryopumping Capacities for Helium and Hydrogen. An auxiliary vacuum jacket thermally isolates the region of the cryofinger which is not used for pumping.

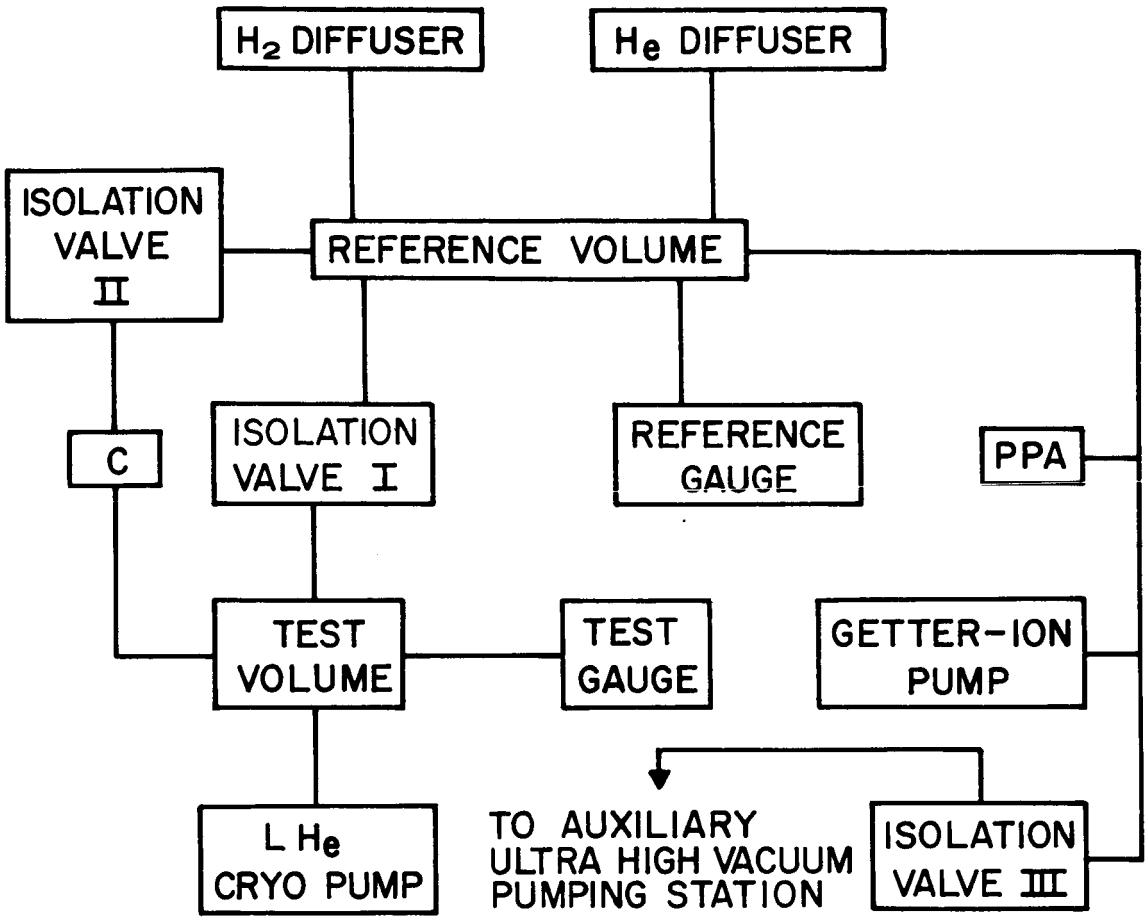

Figure 9 - Block Diagram of UHV System Used to Determine the Gross Cryopumping Capacities of Type 304 Stainless Steel. Helium and hydrogen gas are admitted into the system via a vycor and a palladium diffuser, respectively.

Following each admission of gas the test chamber is isolated and the pressure is monitored until an equilibrium condition exists. Then another charge of gas is admitted in a similar fashion. This procedure can be continued until the cryosurfaces are saturated.

4. Cryopump operation and residual gas analysis: Two sets of data have been collected which have established some operating characteristics for the special LHe cryofinger described in Section 3. They are (1) the determination of the residual gases present in a LHe cryopumped UHV system, and (2) gross cryopumping capacities for helium and hydrogen on type 304 stainless steel at 4.2°K and 18 - 21°K, respectively.

Figure 10 displays a spectrum made when the system was being pumped by an 8 liters/sec getter-ion pump following a bake of 350°C for 12 hr. Although the pressure in the system is 2×10^{-9} torr, it is clear from the spectrum that there is a slight air leak in the system as evidenced by the pressure of a mass 32 peak and an excessively large mass 14 peak. However, the air contribution to the total pressure is quite small in comparison to the limiting residual gases of monoatomic hydrogen and carbon monoxide. The H_1, which is found in great abundance, is being generated from H_2 in the closed system by the getter-ion pump and hot filament ionization sources. This condition can be reversed readily by opening the system to a diffusion pump. The source of He (mass peak 4) is the getter ion pump which has been previously exposed to relatively large quantities of helium. Normally helium is not found in significant quantities in a metal UHV system. The peaks marked Li^+, O^+, F^+ and Cl^+ are not part of the residual gas spectrum but are surface generated ions (Refs. 4 and 7). These ions are produced at the surfaces of metal parts in the PPA ion source due to electron bombardment.

Figure 11 displays a spectrum which was made when the system was being pumped by the LHe cooled cryofinger. Note again the presence of the surface generated ion peaks which cannot be attributed to the residual gas. The total pressure in the system is $\sim 6 \times 10^{-11}$ torr which is established primarily by H_1, CO and H_2O. It is somewhat unusual to have as much water vapor in the system as is shown in the spectrum. This condition indicates that the system is slightly contaminated in spite of a 350°C bake for 12 hr. Also note that He is no longer detectable since the system has been isolated from the getter-ion pump.

Table I compares the analysis of the spectra for both pumping conditions. The greatest effect on the residual gas components in the system is to H_1 and CO which are reduced by factors of $\sim$ 22 and $\sim$ 57, respectively. The other gas partial pressures change by a factor of $\sim$ 2 to 6 or are lost in ion detector noise. The peaks which occur at mass 26 (see Figures 10 and 11)

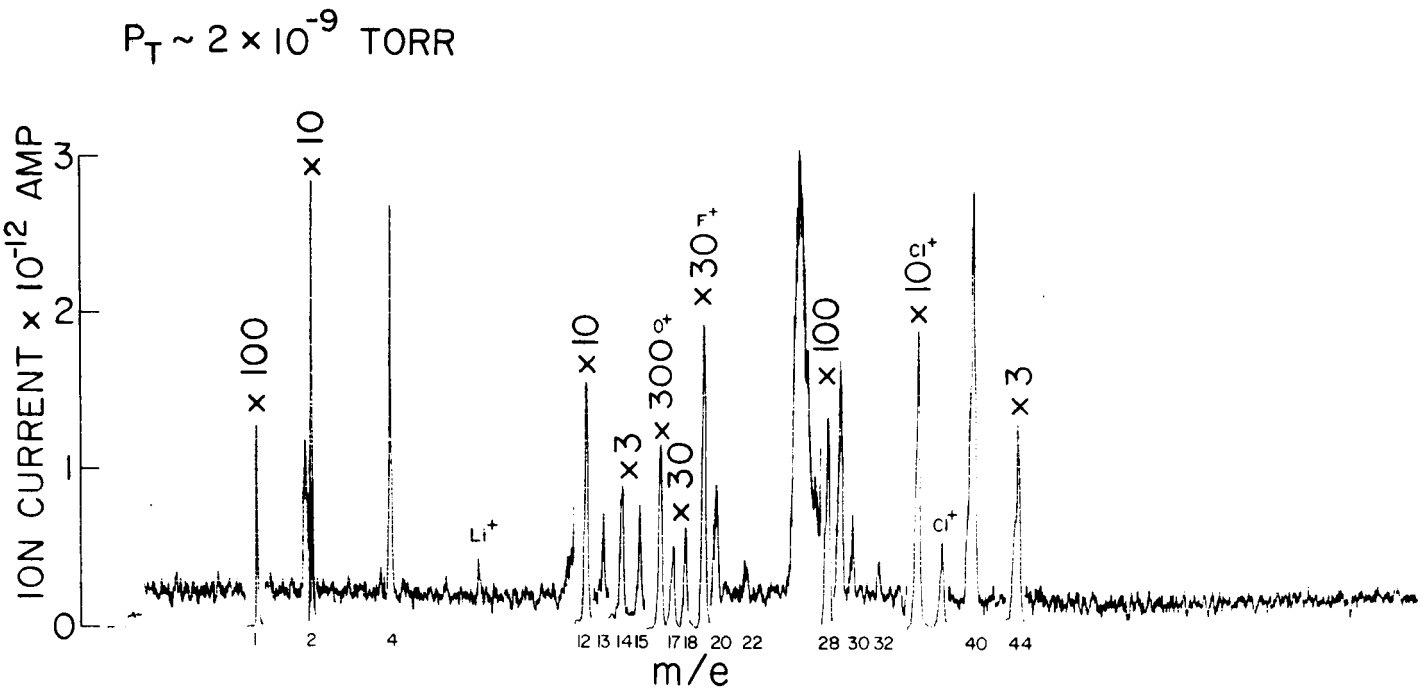

Figure 10 - Residual Gas Spectrum in UHV System Prior to Activation of LHe Cryopump. The spectrum indicates that the limiting gases in the system are H and CO (mass peaks 1 and 28, respectively). The presence of He (mass 4) is due primarily from desorption within the 8 liter/sec getter ion-pump which had been previously exposed to considerable quantities of helium.

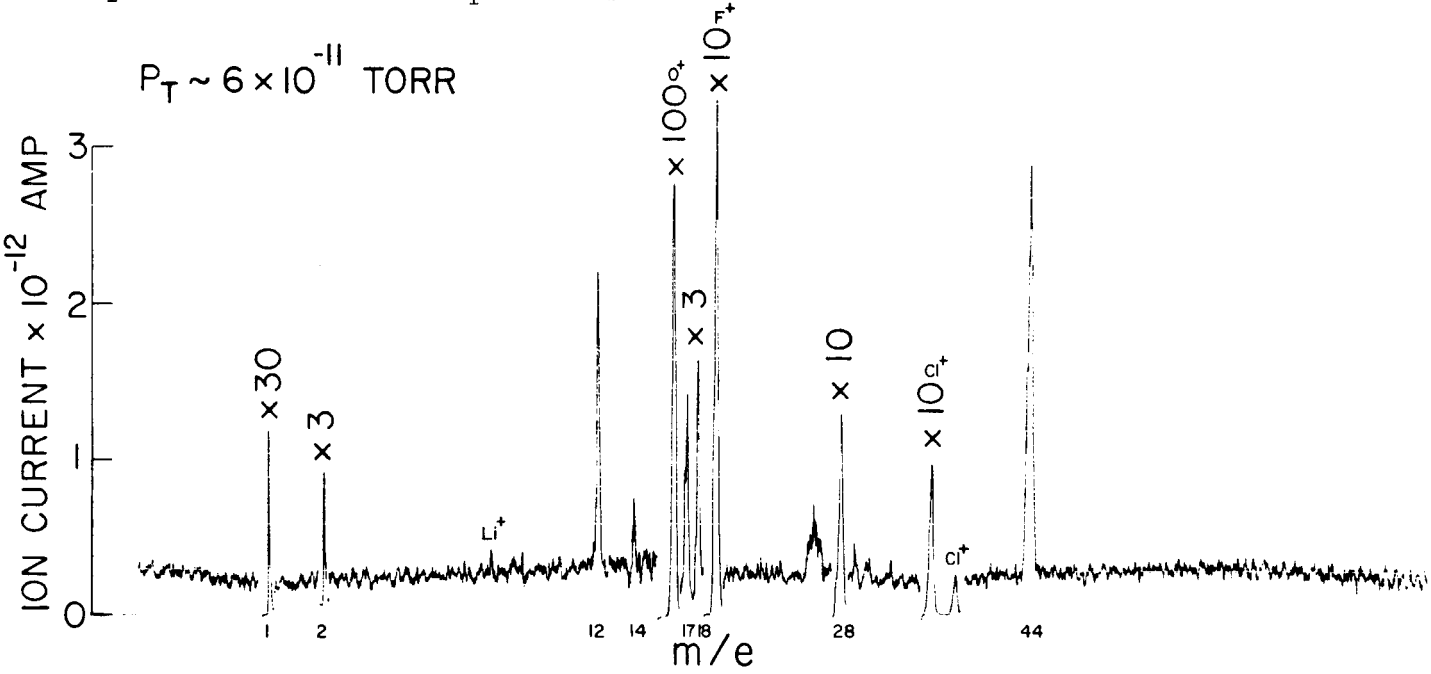

Figure 11 - Residual Gas Spectrum in UHV System After Activation of LHe Cryopump. The system has been isolated from the 8 liter/sec getter-ion pump for this spectrum. The limiting gases in the system are H and CO.

TABLE 1

COMPARISON OF THE RESIDUAL GAS PRESENT IN A UHV SYSTEM FOR TWO METHODS OF EVACUATION

	Getter-Ion Pump	LHe Cryopump (Type 304 stainless steel)
H_1	7.4×10^{-10}	3.4×10^{-11}
H_2	1.5×10^{-11}	2.5×10^{-12}
He	1.4×10^{-12}	-
CH_4	3.0×10^{-12}	-
H_2O	1.4×10^{-11}	5.8×10^{-12}
Mass 26	1.4×10^{-12}	$\sim 4 \times 10^{-13}$
CO	6.3×10^{-10}	1.1×10^{-11}
N_2	2.4×10^{-11}	8.3×10^{-12}
O_2	$\sim 1 \times 10^{-13}$	$\sim 1 \times 10^{-13}$
Ar	1.8×10^{-12}	-
CO_2	2.4×10^{-12}	2.3×10^{-12}
Total	2.0×10^{-9}	6.5×10^{-11}

are due to an unresolvable hydrocarbon group. It is not clear why the CO_2 peak does not respond significantly to the mode change in pumping unless the source for CO_2 is within the analyzer itself. Since the PPA ion source is connected to the system via a 1-in. diameter by 5-in. long tubulation, the pumping speed for gas generated within the PPA would be conductance limited. A CO_2 generation rate of $\sim 1 \times 10^{-11}$ torr liters/sec could account for the steady background of CO_2 observed in the system.

Figures 12 and 13 display the data collected for the gross cryopumping capacity of type 304 stainless steel for He and H_2 at 4.2°K and 18 - 21°K, respectively. The data presented in these curves have been normalized to the active geometrical surface area of the cryofinger. If it is assumed that there are $\sim 2.4 \times 10^{15}$ adsorption sites/cm^2 for He and 1.5×10^{15} adsorption sites/cm^2 for H_2 on a metal surface (Ref. 8), then one monolayer of gas would correspond to $\sim 7 \times 10^{-5}$ torr liters/cm^2 of He or $\sim 4 \times 10^{-5}$ torr liters/cm^2 of H_2. These values agree with the flat portions of both curves if a surface roughness factor of ~ 1.5 is assumed. Based on the above assumptions, the rapid increase in pressure begins at approximately 1/2 monolayer coverage.

B. Getter-Ion Pumping Including a Study of the Characteristics of Penning Discharge Phenomena

Vacuum pumps and gauges which employ a pressure dependent gaseous discharge of the Penning type have been analyzed. Their operational characteristics are described below. Details which are presented include a discussion of the collapse of the central electron cloud, an explanation of the upper and lower modes of the discharge, and a description of pumping speed changes and sensitivity variations. The experiments with pumps have also provided data for determination of the residual gases present in an ultrahigh vacuum stainless steel system using the getter-ion pumping technique.

1. A study of getter-ion pump operation: A series of experiments has been conducted to determine the effect of the cathode to anode voltage on the pumping speed of a getter-ion pump. The pump used in these studies was a Varian 8 liters/sec diode pump consisting of 36 square cells, 1/2 in. by 1/2 in. The cathode to anode voltage was varied from 600 to 7,700 v. The residual gases present in the system were determined by means of a General Electric Model 514 partial pressure analyzer, PPA. A data plot displaying the relative changes in the residual gas composition vs. the applied voltage is given.

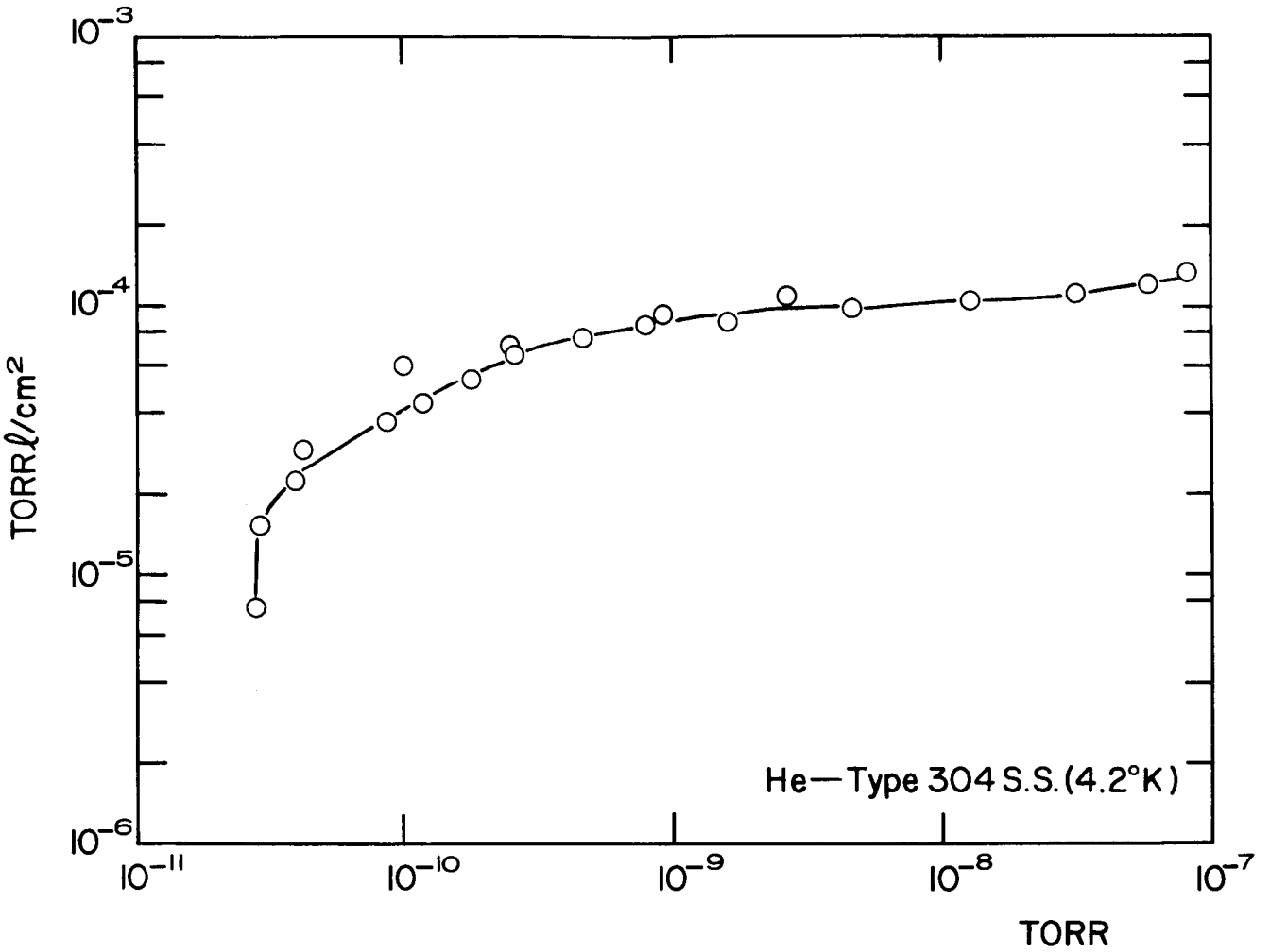

Figure 12 - Gross Cryopumping Capacity Data for Helium Adsorbed on Type 304 Stainless Steel. The temperature of the cryofinger was maintained at 4.2°K.

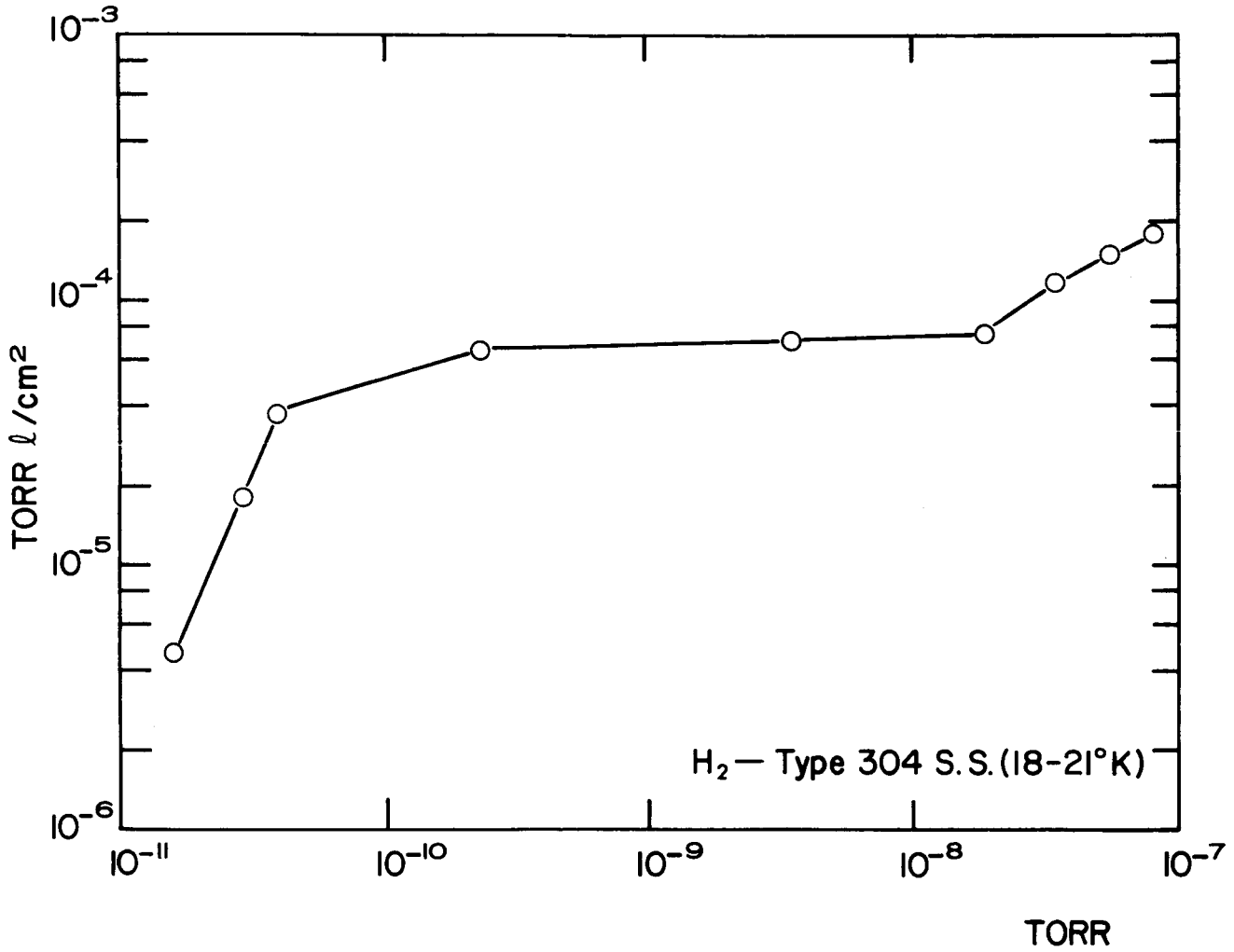

Figure 13 - Gross Cryopumping Capacity Data for Hydrogen Adsorbed on Type 304 Stainless Steel. The temperature of the Cryofinger was maintained between 18 - 21°K.

The 8 liters/sec getter-ion pump was mounted on the partial pressure analyzer system (PPAS) with a line of sight path between the analyzer ion source and the getter-ion pump anode. The system including the getter-ion pump was baked to 350°C. Following degassing of the analyzer and the ionization gauge by electron bombardment, the getter-ion pump was activated. We experienced difficulty in starting the getter-ion pump below 10^{-8} torr until at least 4,000 v. was applied to the anode. After the pump was operating and the UHV system was isolated from the auxiliary diffusion pumped bake out system the ultimate pressure attained by the system was $\sim 8 \times 10^{-11}$ torr.

Total pressure in the getter-ion pump system was measured as a function of various cathode to anode voltage values (see Figure 14, Curve A). It is interesting to note the sharp increase in pressure (decrease in pumping speed) for voltage values below 1,000, corresponding to a decay of the discharge activity in the getter-ion pump. The last set of data was recorded for a 600-v. setting. Pump voltage was then reduced to zero. The background pressure resulting from the pumping action of the ionization gauge and the analyzer was determined to be 4.2×10^{-10} torr.

A study of the residual gases in a getter-ion pump system was conducted for various pump voltages. A typical residual gas spectrum is shown in Figure 15. This curve was recorded at a pressure of $\sim 8 \times 10^{-11}$ torr while using 3,000 v. on the getter ion pump anode. The residual gases consist primarily of CO, H, and H_2 with lesser amounts of CH_4, H_2O, Ar, CO_2 and He. The peaks at mass numbers 16, 19, 35 and 37 have been shown (Refs. 4 and 7) to be recordings of surface generated ion fragments resulting from electron bombardment of adsorbed molecules on metal parts of the analyzer.

A background current of $\sim$ 1 to 2 microamperes was measured in the getter ion pump for the higher voltage settings. Under the assumption that this current was due to field emission, a 10,000 v. AC signal was applied to the pump for 10 sec. Such a high voltage application should destroy field emitting tips. Following this treatment the background current was < 0.1 microampere with an anode voltage of 7,700 v. Thus, the reduction by over an order of magnitude of the background current supports the field emission hypothesis.

During the high voltage application just described it was necessary to open the analyzer system to an auxiliary diffusion pump, because of the increased gas load. Although the pressure in the system was subsequently reduced, the inner walls were contaminated by some atmospheric gases. Figure 16 is a partial pressure spectrum taken after the high voltage treatment and after the system had returned to a stable low pressure. The getter-ion pump was operating at 3,000 v. Note the increase of CH_3, Ar,

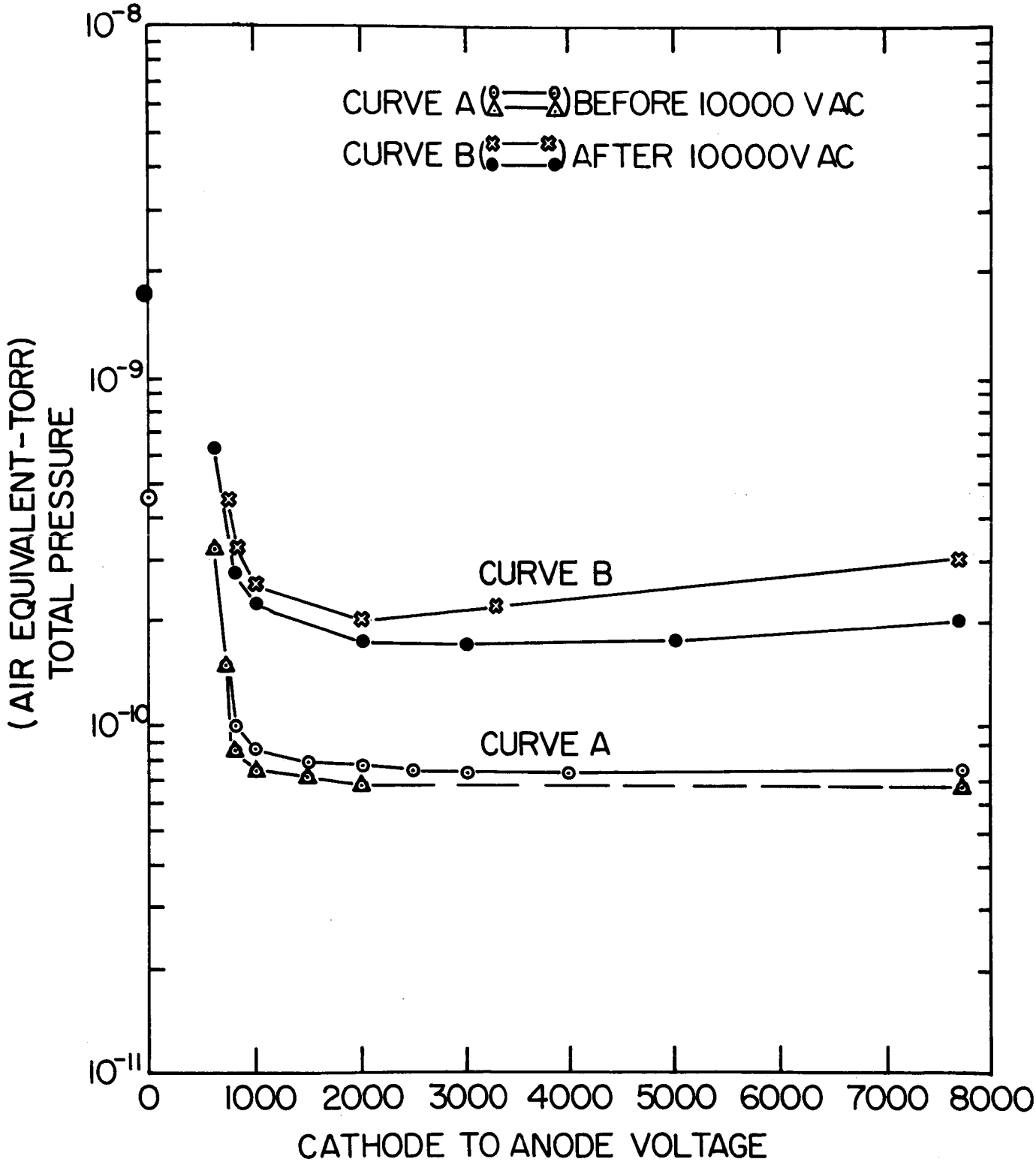

Figure 14 - Plot of Total Pressure vs. Cathode to Anode Voltage for a Getter-Ion Pump Employing 36 1/2-in. Square Cells. Data for Curve A were collected following a 350°C bake of the pump. Data for Curve B were collected after pump had been exposed to some contaminating gases.

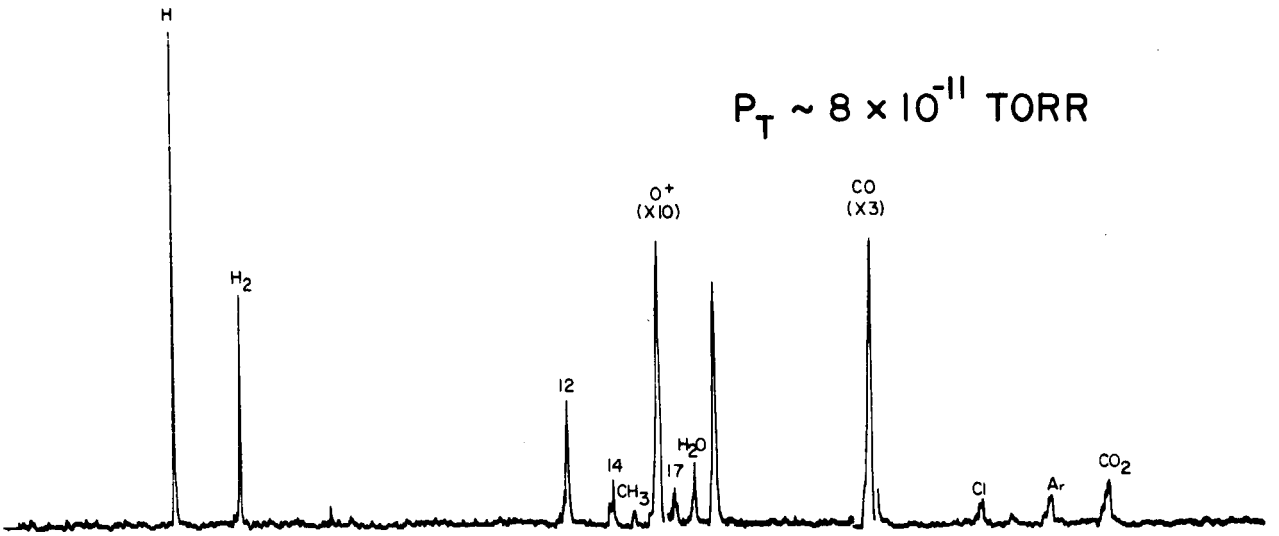

Figure 15 - Residual Gas Spectrum in a UHV System Following a 350°C bake. System Evacuated by a Getter-Ion Pump Operating at 3,000 v.; Total Pressure $\sim 8 \times 10^{-11}$ Torr.

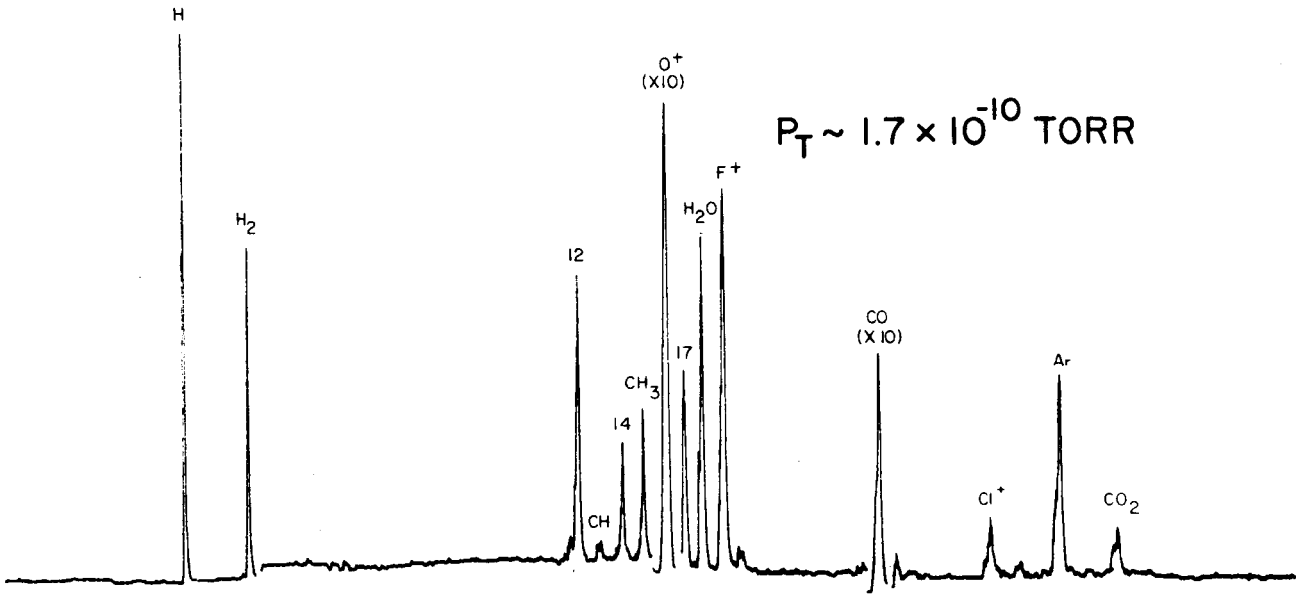

Figure 16 - Residual Gas Spectrum in a UHV System Following Exposure to Some Contaminating Atmospheric Gases. System Evacuated by a Getter-Ion Pump Operating at 3,000 v.; Pressure $\sim 1.7 \times 10^{-10}$ Torr.

CO, H_2O, and H_2 which indicates that the interior surfaces of the system had been contaminated. Since a reasonably constant desorption rate was established by heating the filaments in the ionization gauge and partial pressure analyzer, an ideal condition was established to study the pumping efficiency of the getter-ion pump in the UHV range for the gases listed above. Both the total pressure (see Figure 14, Curve B) and the gas composition in the system were studied as functions of cathode to anode voltage. Figure 17 is a summary plot of the relative changes of residual gases within the system for an anode voltage variation between 600 v. and 7,700 v. H, H_2, H_2O, and CO_2 demonstrate little effect due to discharge activity within the pump. However, the ionically pumped species CO, Ar, CH_4 and He undergo a large variation with discharge activity.

It is interesting to note the slight increase which occurs at the high voltage end of the CO and Ar curves. These data suggest that above 5,000 v. the desorption of CO and Ar due to the discharge increases beyond the pumping speed for these species at lower voltages. This effect is noted also on the total pressure curve, (Figure 14, Curve B) by a pressure increase at higher voltages. On the other hand, the pumping speed for He and CH_4 increases with anode voltage. If the pump is deactivated (zero voltage) the various gases take on the relative levels shown on the ordinate of Figure 17.

Two sets of data are presented in Figure 14 under the caption "Curve B." One set of data was collected shortly after the pump was exposed to the auxiliary diffusion pump system (x-x) and the second set was collected after 15 days of pumping by the getter-ion pump (...). Note the increase in total pressure with anode voltage immediately following exposure to the diffusion pump (x-x) and the lack of increase in total pressure with anode voltage after the extended pumping period (...). This change in pressure response to anode voltage after extended pumping indicated that initially the total pressure in the system was limited by desorption of adsorbed gases within the getter-ion pump at the higher anode voltages. After extended pumping the data indicated that the pump had cleaned itself and that the total pressure was limited by system desorption throughout the entire range of anode voltages studied. These results indicate that significant benefit can be gained from baking getter-ion pumps which operate at high voltages.

2. Characteristics of Penning type discharge: The operation of cells utilizing a Penning type gaseous discharge has been examined. A new interpretation has been formed regarding the significant change of the discharge which occurs in the ultrahigh vacuum range. By recording data from two separate regions of the discharge, it was possible to observe an extinction of the central electron cloud. Such a cloud between the cathode

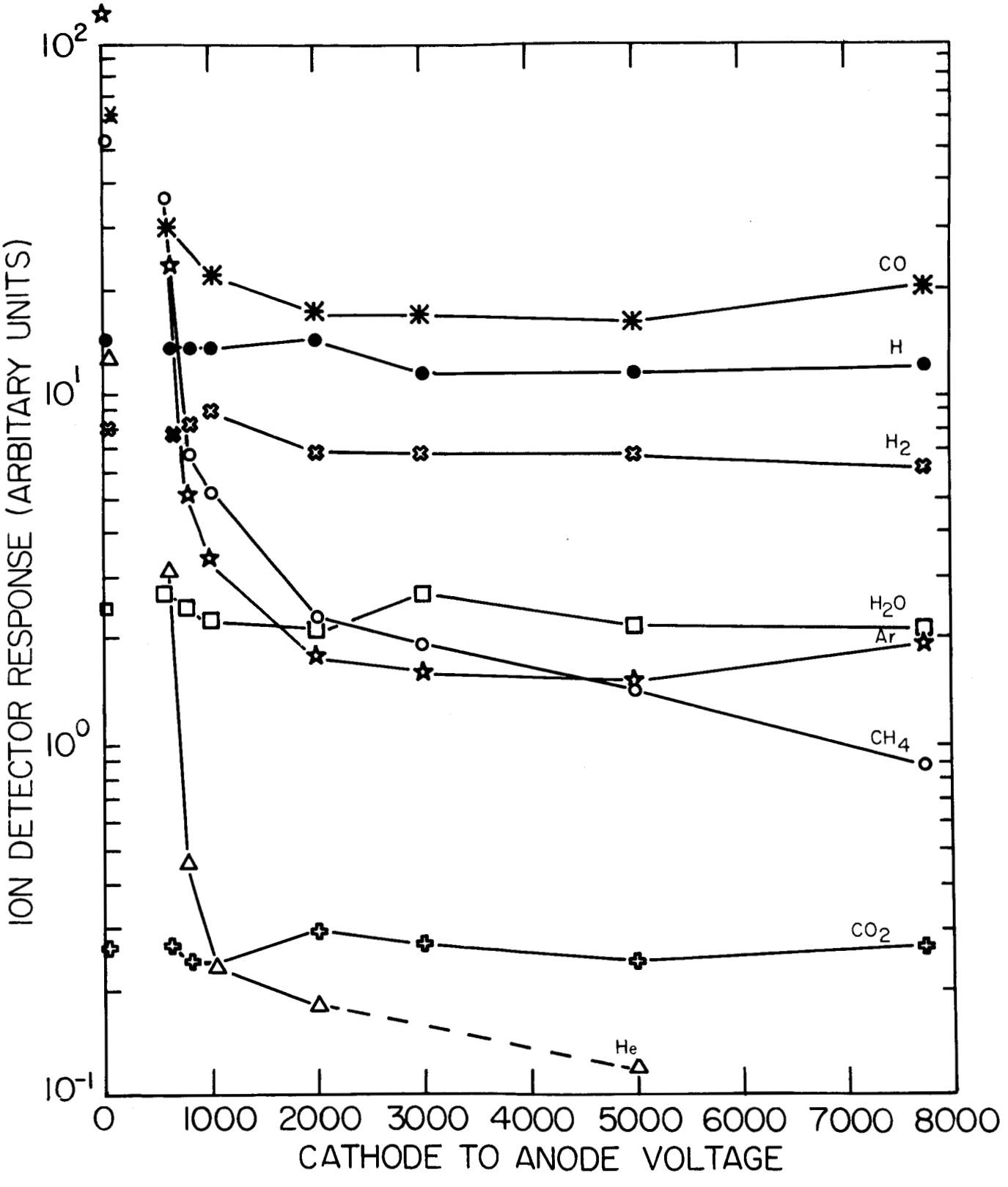

Figure 17 - Summary Plot of the Residual Gases Found in a UHV System Operating at Various Cathode to Anode Voltages. The system was evacuated by a Getter-Ion Pump.

end plates was referred to by Helmer and Jepsen (Ref. 1) as a "virtual cathode." The loss of this central discharge concentration results in lower pump speeds (gauge sensitivity) of devices utilizing a Penning discharge.

Ions produced in a Penning cell are normally accelerated to the center of the cathode end plates. Evidence of ion impact is seen from the sputtering erosion of titanium which occurs at the center of getter-ion pump cathodes. Evidence of ion burial may also be seen as a discoloration effect on the stainless steel cathode plates in Penning cell gauges. In both cases the ion trajectories indicate the existence of an electron cloud concentrated axially between the two cathode end plates.

Results have been obtained with a Penning cell vacuum gauge for the pressure range from 1×10^{-3} torr to 8×10^{-12} torr as shown in Figure 18. Discharge intensity, I/P in amps/torr, is plotted as a function of pressure. The solid line data plot shows the response curve obtained for a gauge with a 1.25 cm. diameter Penning type cell operating at 2-kv. anode potential with a 1-kg. magnetic field. The data shown as a dashed line were reported by Rutherford (Ref. 9) for a vacuum pump utilizing an array of 1.25 cm. Penning cells operating with 3 kv. and 1 kg. It is interesting to note the similarity of the operating characteristics for the two systems (see Figure 18).

The similar characteristics include a maximum discharge intensity near 10^{-5} torr and a major decline of the discharge as pressure decreases to 10^{-8} torr. An interesting change occurs in the discharge curve as evidenced by a dip near the 10^{-9} torr range indicating a real change of the discharge itself. Following this change, a pressure dependent discharge still exists within the Penning cell but with a relatively low intensity.

Further insight regarding the change in discharge activity has been gained by operating an experimental Penning cell in which the current at the center of the cell can be measured independently of the current at the outer circumference of the cell. Two sets of cathodes (see Figure 19) are employed, viz., a center or axial set called the main cathodes and an annular set near the anode edge called auxiliary cathodes.

The experimental Penning cell constructed for this program (see Figure 20) has shown evidence of ion burial at the center of the main cathode plates for pressures above 10^{-8} torr and evidence of ion burial at the auxiliary cathodes for pressures below 10^{-8} torr adjacent to the anode edge. Thus, we may conclude that the predominant discharge activity shifts from the concentrated axial cloud (virtual cathode) to a ring shape adjacent to the anode edges as pressure is reduced below about 10^{-8} torr.

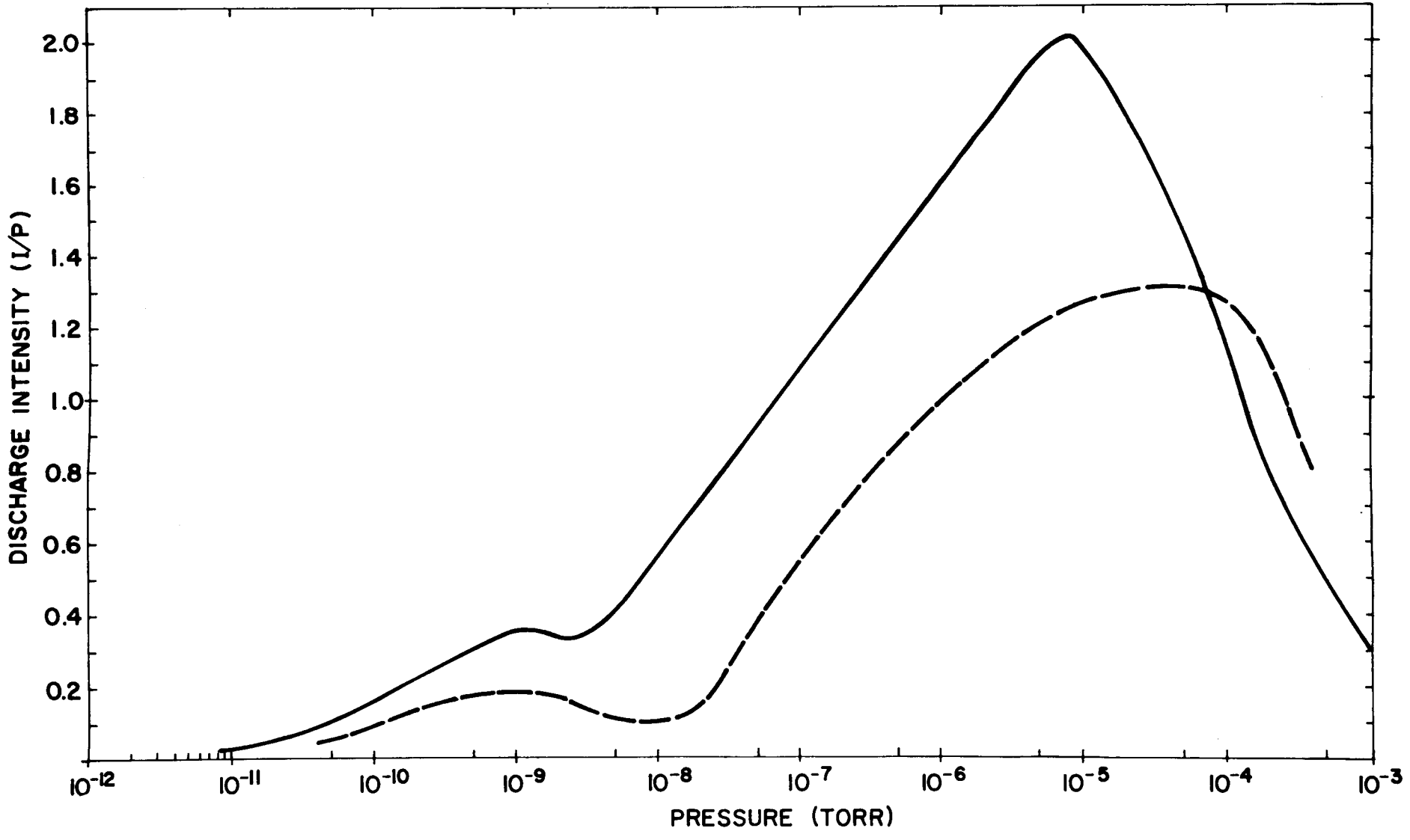

Figure 18 - A plot of the Ratio of Current to Pressure vs. Pressure for 1.25 cm. Penning Cells (Dashed Line Data from Ref. 9). Maximum response occurs near 10^{-5} torr; the main discharge extinguishes below 10^{-8} torr leaving a lower intensity response; see text.

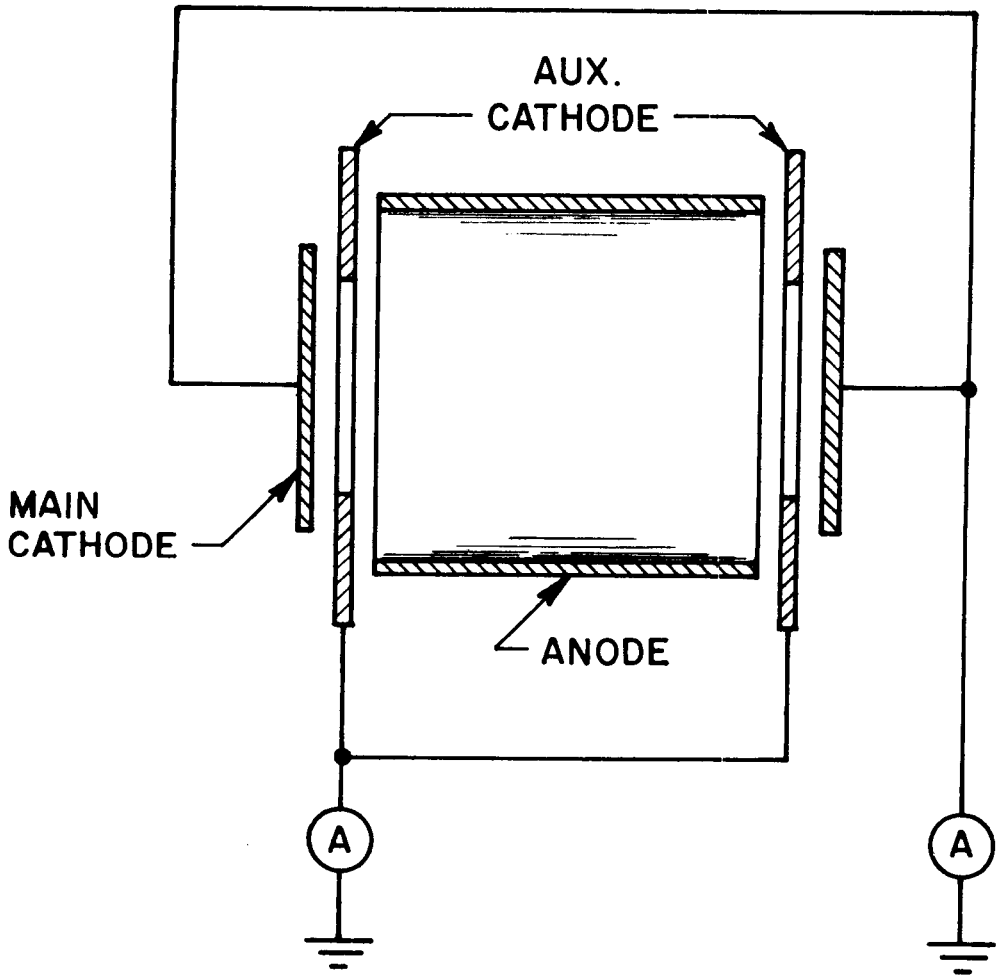

Figure 19 - Schematic Diagram of Experimental Penning Cell Used to Study Discharge Geometry. Current to the auxiliary cathodes is measured independently of current to the main cathodes.

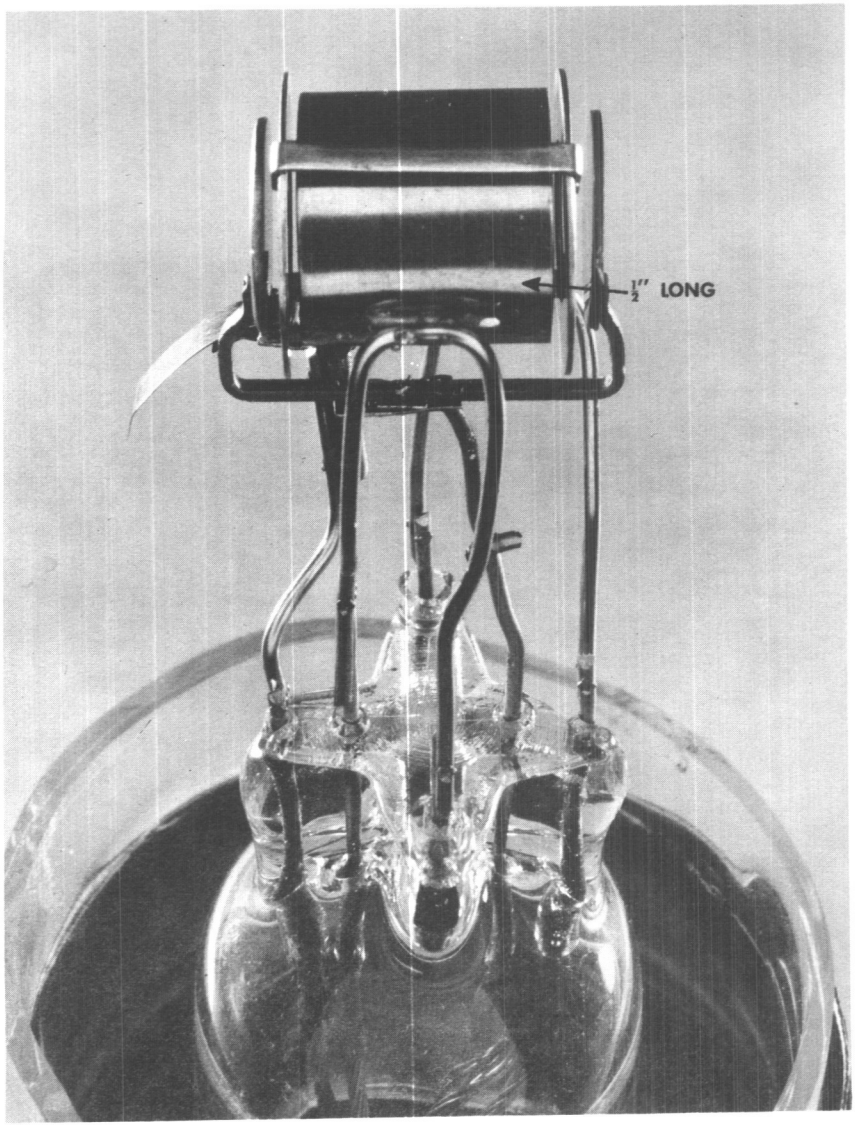

Figure 20a - Special Design Penning Cell with Double Cathode Arrangement, Electrode Structures: Center Cylinder, Anode; Adjacent Rings, Auxiliary Cathodes; Outer Plates, Main Cathodes; Clip on Left, Grounded Shield Contact.

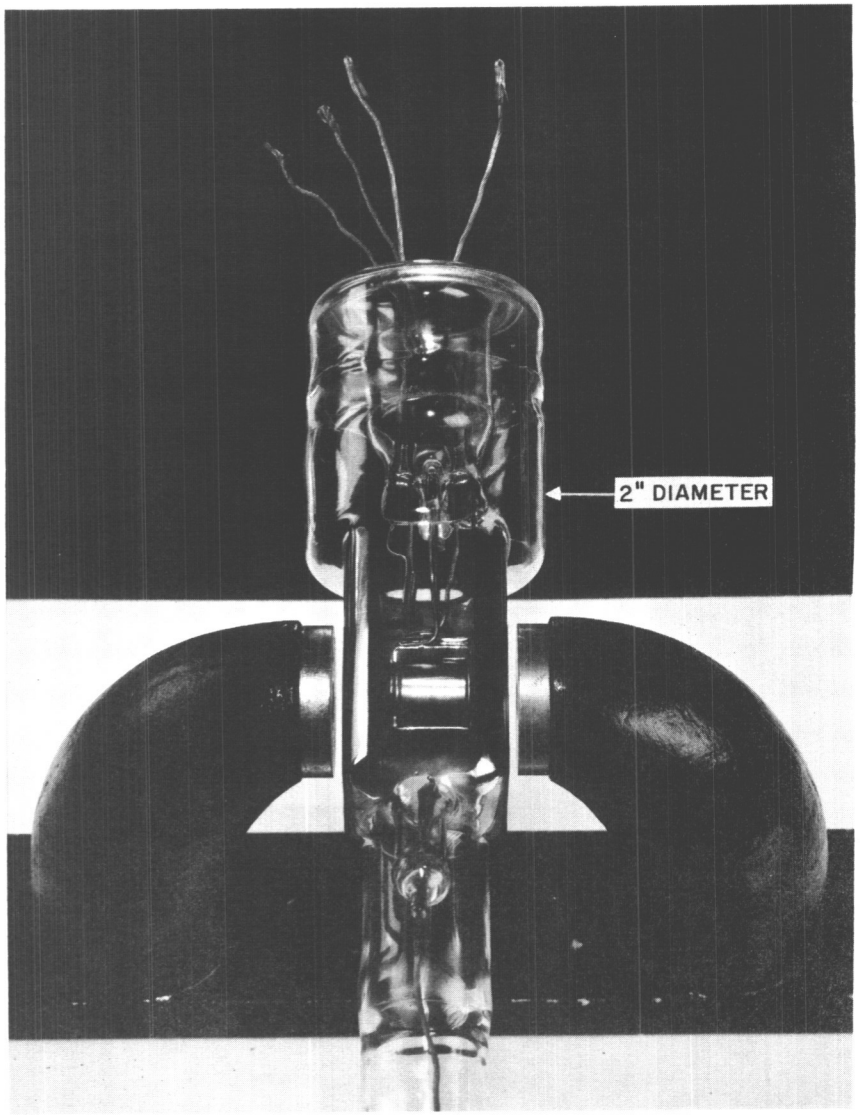

Figure 20b - Dual Cathode Penning Cell. Current flow to the main and auxiliary cathodes may be monitored separately.

The special dual cathode Penning cell referred to above is capable of separating ion current arriving at the main cathode region from current to the annular auxiliary cathode region near the anode. Thus data have been collected which directly record the shift of discharge activity from the axial region to the anode ring vicinity as pressure decreases below 10^{-8} torr.

Figure 21 is a plot of the currents measured by the auxiliary cathode set and by the main cathode set independently. For the higher pressure range above 10^{-8} torr the main cathode collects over 70 percent of the ion current although the areas of the two cathode sets are nearly equal. Thus, the concentration of ion current in the center of the cylindrical cell attests to the existence of the axial electron cloud described above. Whereas the sharp decline of main cathode current below 10^{-8} torr, as seen in Figure 21, indicates a loss of the virtual cathode discharge.

Current recorded by the main cathodes is predominantly ion current. However, current to the outer auxiliary cathodes may consist of field emission current or leakage current as well as ion current. Thus, three different currents may be significant to the auxiliary cathodes and under certain conditions any one could be predominant. Although the three different contributions are not separable by the total current meter, a comparison of the electric field-current relationship with those expected for ion, field emission, and leakage currents can be made.

Results obtained from the dual cathode Penning cell also have shown that the sensitivity is lowered by the loss of the central electron cloud (virtual cathode). The data given in Figure 18, from a single cathode Penning cell with the same operating parameters, also show a similar loss of sensitivity. Most notably the loss of the virtual cathode occurred at the same pressure for which Figure 18 showed the noticeable change in discharge intensity. Thus, the spatial distribution of ion current recorded by the dual cathode gauge and the discharge intensity data of Figure 18, both confirm the space charge phenomenon described above.

The phenomenon mentioned above is apparently the same effect as observed by Rutherford (Ref. 9) and referred to as the low intensity mode of the discharge which continues below the cut-off pressure value. Using both single cathode and dual cathode Penning cells, we now have obtained an explanation for the cut-off and lower mode phenomena. Cut-off of the discharge corresponds to extinction of the virtual cathode space charge. The lower mode corresponds to a low intensity discharge which continues near the anode edges.

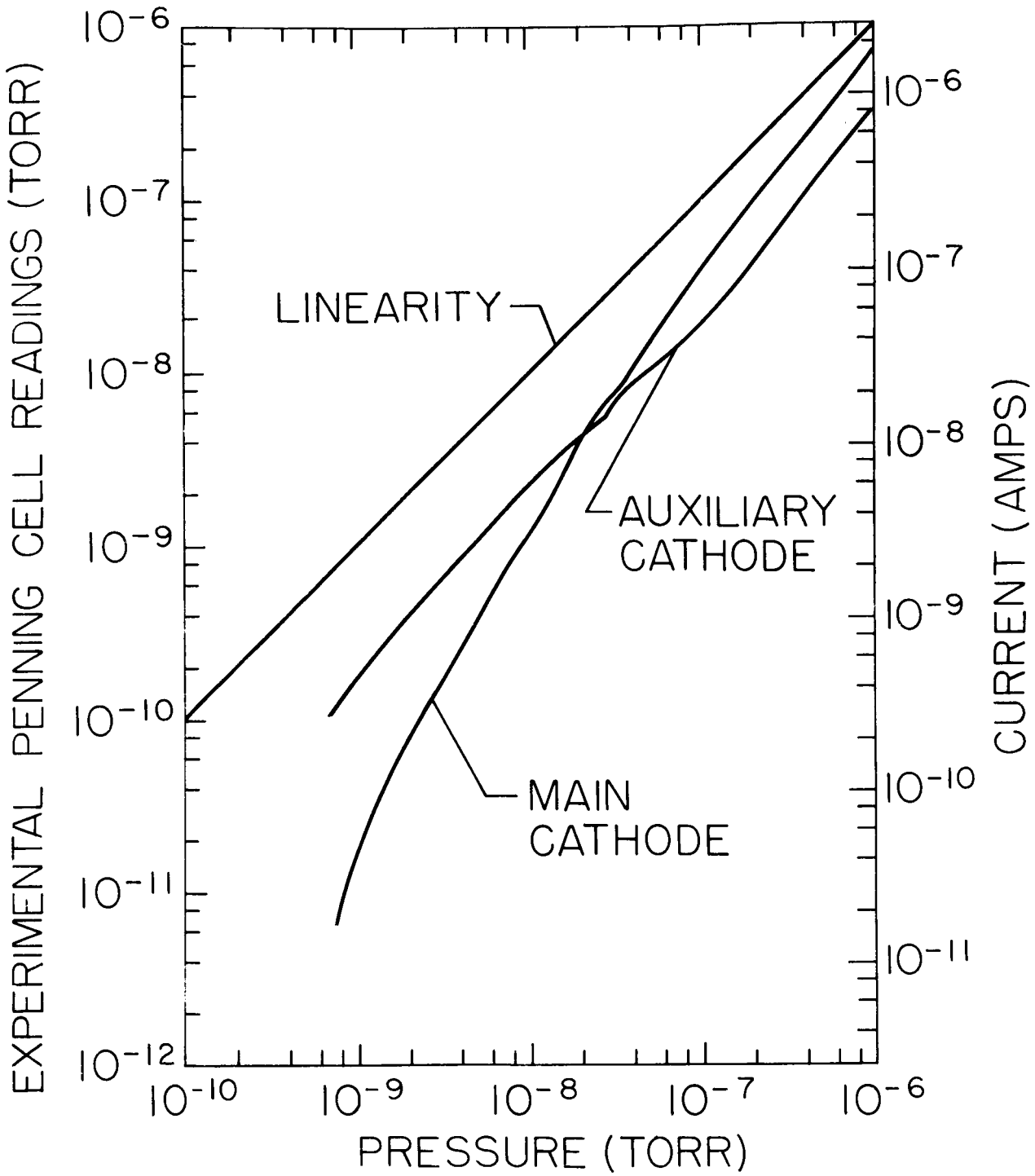

Figure 21 - A Plot of Ion Current Recorded at the Center of a Penning Cell Discharge (Main Cathode) and Near the Outer Edge of the Cell (Auxiliary Cathode)

C. Improved Diffusion Pump Operation by Use of a Dual-Expansion Nozzle

A dual-expansion nozzle has been constructed and evaluated for diffusion pump operation. A significant increase in pumping speed was maintained while operating at elevated boiler temperatures. Thus yielding an improved combination of pumping speed and back diffusion rates.

1. Diffusion pump operation: The operational cycle of a vapor pump can be described as follows: The working fluid (Hg in this case) is heated in a boiler to increase the vapor pressure in the jet stack and to impart kinetic energy to the evolving gas. The pump vapor then flows through a tube to a nozzle assembly where it undergoes an expansion into a pumping region thus forming a vapor jet. The geometry and orientation of the jet is such that the pump vapor collides with a cold surface, where it condenses. This condensate is then returned to the boiler assembly for recirculation.

The pumping effect of the diffusion pump is based on a transfer of momentum from the expanding jet to (1) incoming molecules from the vacuum chamber and (2) gas molecules which are back diffusing through the jet region into the vacuum chamber. The vector sense of the momentum transfer is such that the direction of gas flow is established away from the vacuum chamber.

The first process, viz., molecule entrainment by the vapor jet, determines the pumping speed. The critical parameter in this operation is the degree of uniformity with which momentum is transferred from the vapor jet to incoming gas molecules. This is particularly true at the upper boundary of the jet where the incoming gas first encounters the vapor stream. If there is turbulence at this boundary, significant amounts of gas can be repelled back into the vacuum chamber. The amount of such turbulence is a function of nozzle design and vapor density, viz., lower density jets generate less turbulence.

The second process, viz., back diffusion determines the pressure drop which can be maintained across the vapor jet. Back diffusion reduction is highly dependent on the vapor density, viz., higher density jets can maintain a greater pressure differential.

A dilemma arises when back diffusion is reduced by increasing boiler pressure, because the corresponding increase of turbulence in the vapor jet reduces the ability to entrain gases. It has been postulated that a dual expansion nozzle would aid in resolving the dilemma (Refs. 2 and 3). Such a nozzle should generate a high density main jet surrounded by a low density umbrella jet. Therefore, it is the purpose of the present work to determine the relative pumping efficiency of a dual expansion nozzle versus a single expansion nozzle when operating at high boiler pressure.

2. Dual-expansion nozzle experiment: A schematic diagram of the nozzle assembly design for this work is shown in Figure 22. This assembly consists of a movable end cap which is used to form a low density umbrella jet, and a fixed deflection skirt used to form a high density main jet. The thin-walled stainless steel tube which supports the end cap is attached to a screw driving assembly outside the vacuum system via a bellows in the bottom of the mercury boiler, as shown in Figure 23. This tube can be used to increase or decrease the gap between the end cap and the top of the jet stack. For this study, the gap was opened to $\sim$ 0.010 in. when the nozzle was used in the dual expansion mode. The temperature at the boiler and various positions along the jet stack including the exit aperture at the nozzle is monitored by a series of thermocouples which have been placed within the thin-walled stainless steel tube.

The nozzle assembly is inserted into a glass UHV test chamber (see Figure 24) via a 2-1/2 in. I.D. metal flange. The test stand is equipped with appropriate gauges, LN_2 traps and helium diffusers. As shown in the block diagram of Figure 24 to permit measurements of (1) the pumping speed of a test nozzle, and (2) the ratio of pressures which can be maintained across a test nozzle.

Pumping speed determinations were based on the following calculation:

$$S = \frac{Q}{P_1} \tag{12}$$

where S = pump speed of the test nozzle assembly, Q = gas flowing into the test chamber, and P_1 = pressure above the test nozzle. The gas flow through a conductance C is given by the equation:

$$Q = C(P_2 - P_1) \tag{13}$$

where C = conductance of the orifice, and P_2 = pressure at gauge 2 (see Figure 24). Substituting Eq. (13) into Eq. (12) gives:

$$S = C\left[\frac{P_2}{P_1} - 1\right] . \tag{14}$$

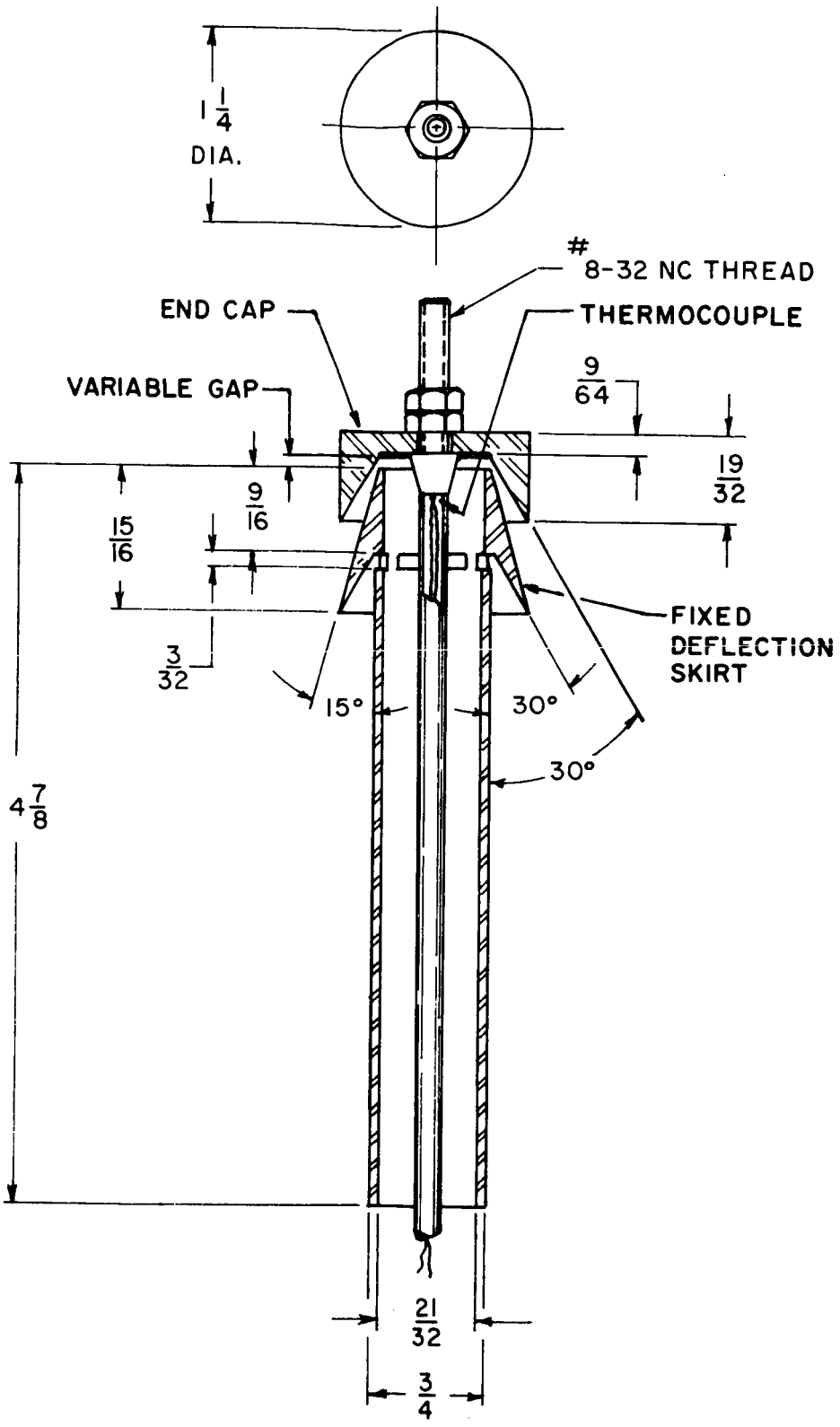

Figure 22 - Schematic Diagram of a Dual Expansion Nozzle Assembly. An umbrella jet can be formed or eliminated by opening or closing the gap between the main assembly and the adjustable end cap.

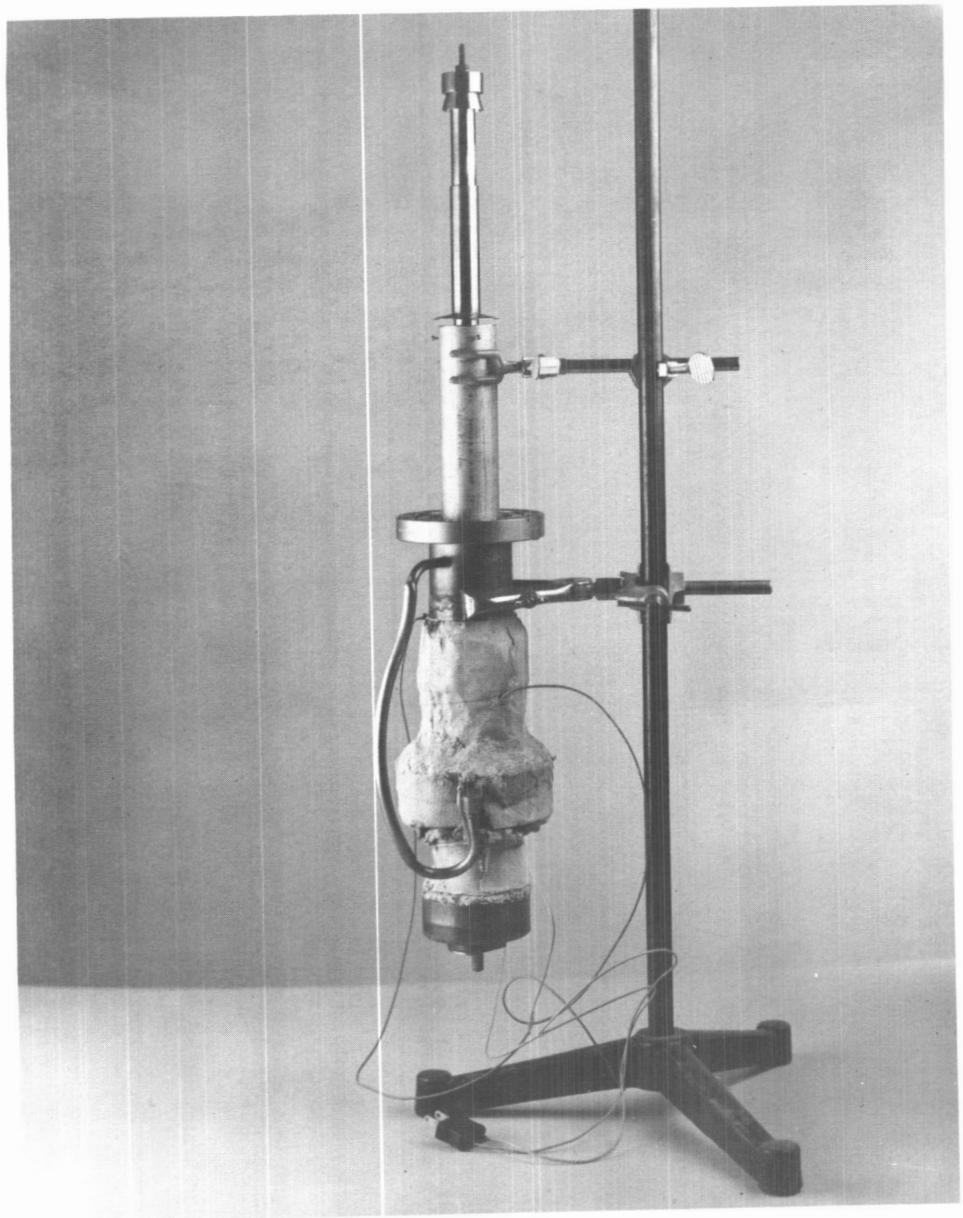

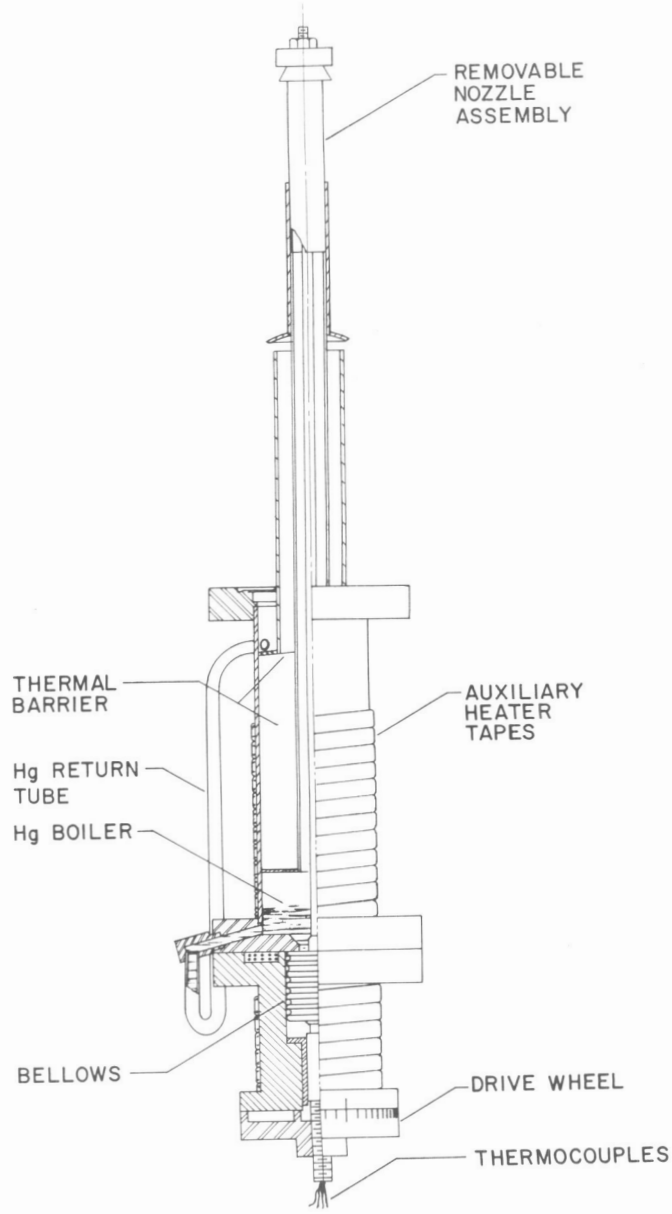

Figure 23 - Schematic Diagram (right) and Photograph (left) of the Special Test Apparatus for Evaluation of Dual Expansion Diffusion Pump Nozzles. The drive mechanism provides for continuous variation of nozzle gap during operation.

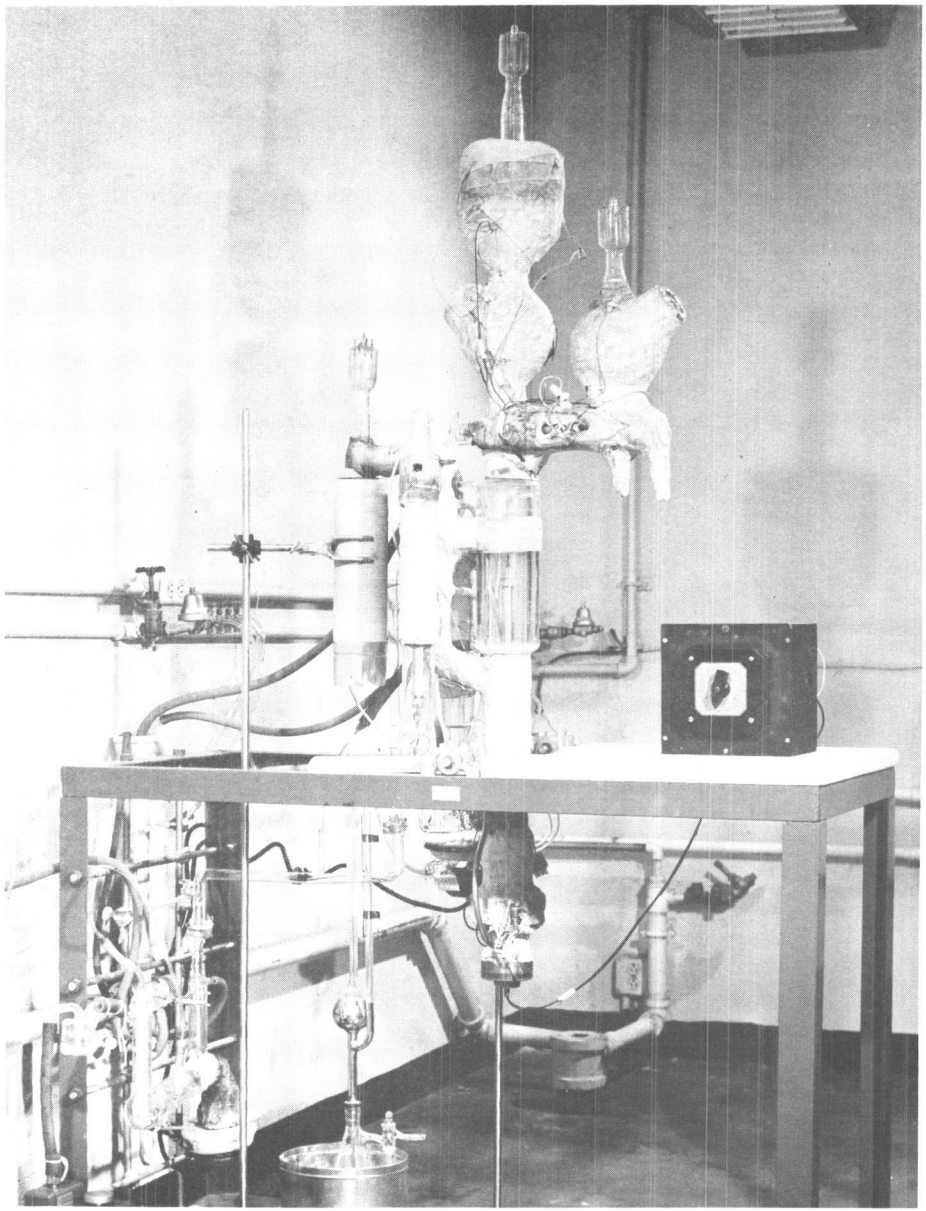

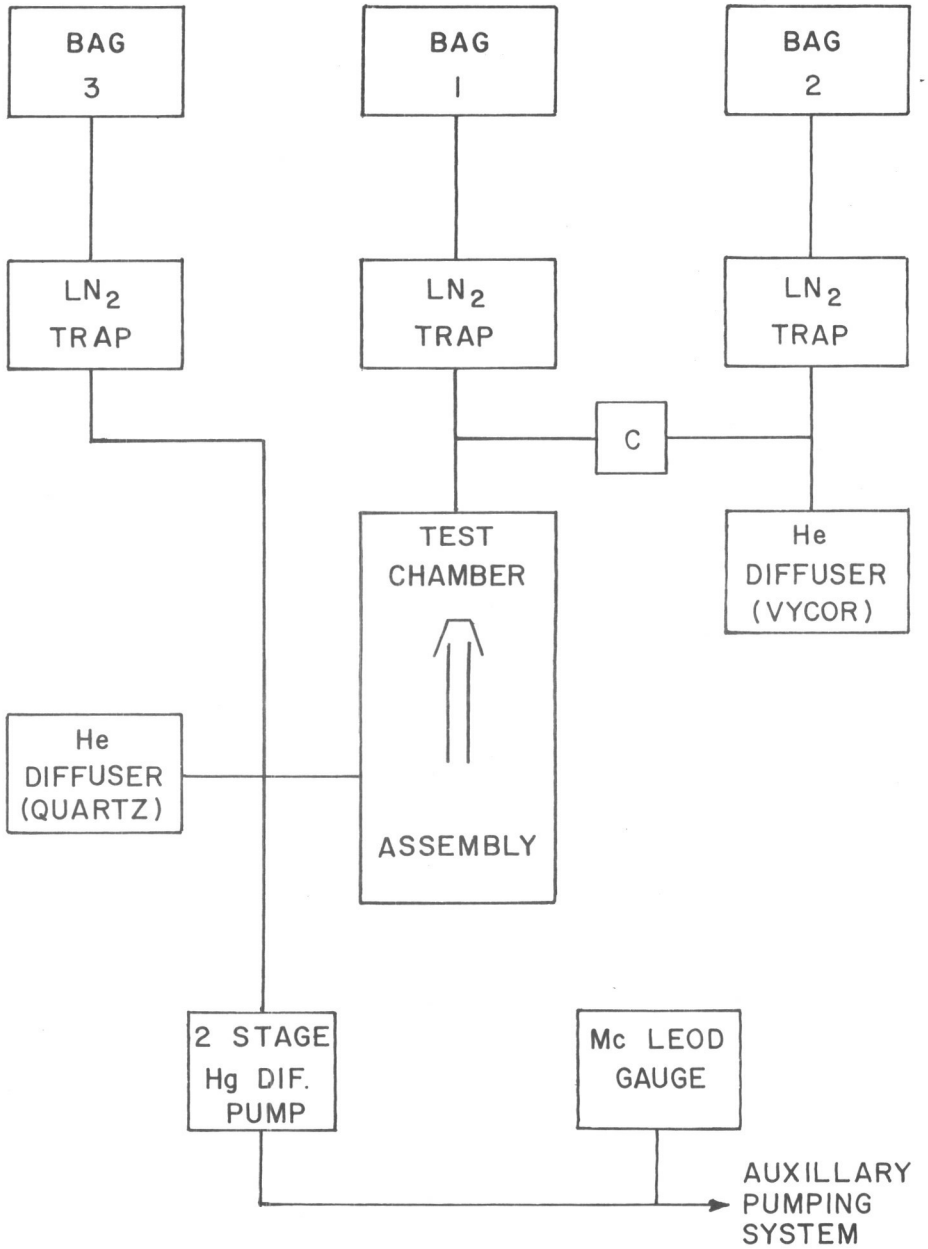

Figure 24 - Schematic Diagram (right) and Photograph (left) of the Vapor Jet Test System Showing Three Reference Gauges (top) and Test Nozzle (center)

The conductance (C) is determined by the equation:

$$C = 3.638\ KA\left(\frac{T}{M}\right)^{1/2} \text{ liters/sec} \qquad (15)$$

where K = Clausing or variational factor, A = cross-sectional area of the orifice (cm^2), T = temperature (°K), and M = gram molecular weight of the flowing gas.

Helium is used as the test gas in these measurements, therefore M = 4. This gas is supplied via a 6-in. vycor diffuser which is mounted close to the orifice (C). The heat generated when operating the diffuser establishes an orifice temperature of 455°K during the test. The area (A) of the orifice is 0.148 cm^2 and K = 0.5814. Substituting these values in Eq. (15), C is determined to be:

$$C = 3.3 \text{ liters/sec} \quad .$$

Finally, Eq. (14) can be written as

$$S = 3.3\left[\frac{P_2}{P_1} - 1\right] \text{ liters/sec} \quad .$$

The ratio of pressures maintained across the jet region is also calculated for the range of boiler temperatures studied. Helium is again used as the test gas; however, a larger source is required because of the pumping speed of the two-stage backing diffusion pump. Therefore, a large quartz diffuser is used to supply up to 1 micron liter per second of pure helium.

Data are presented graphically in Figures 25 and 26 for both the umbrella and nonumbrella jet configurations. The boiler temperature was varied slowly from 24°C to 232°C. However, above 197°C severe pressure fluctuation occurred and quite often the electronic protection circuits would shut off the gauges. Therefore, no data are presented for this unstable operating range. The data below approximately 115°C show the effect of the two-stage diffusion pump which backs the test chamber. Above this temperature the vapor jet begins to form and intensifies with increasing boiler temperature (increasing vapor pressure). The pump speed for the configuration without an umbrella peaks near 170°C and subsequently falls off. In this region (170°C) the density of the gas has increased to the point where the Reynolds number has exceeded a critical value and,

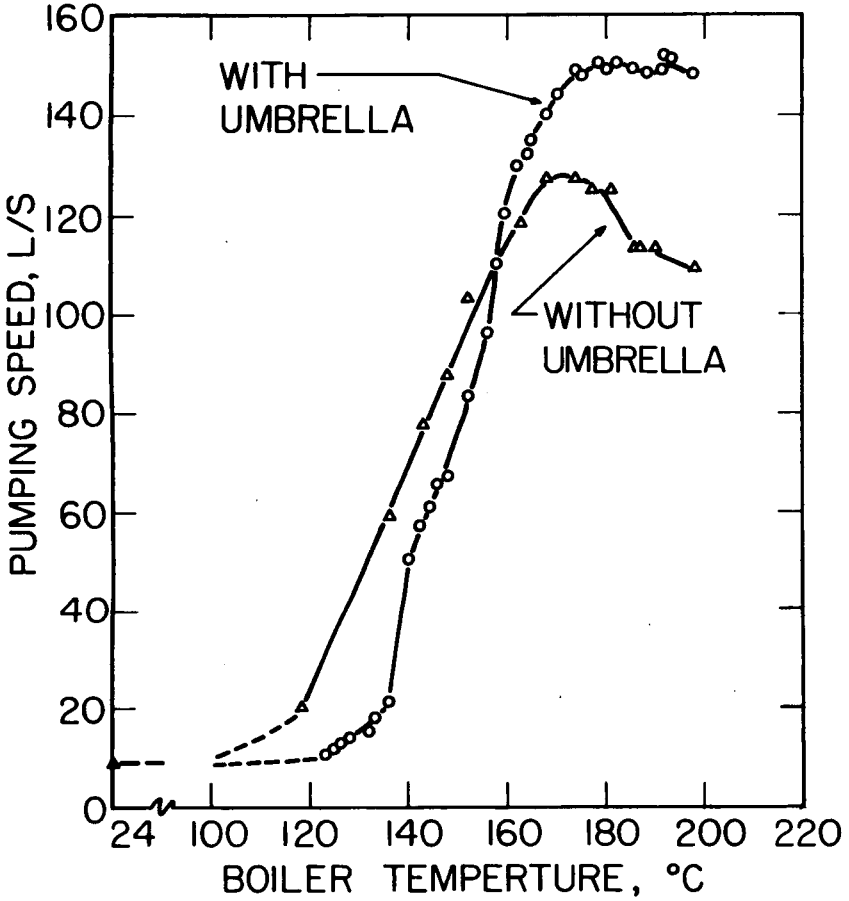

Figure 25 - Pumping Speed for Single and Dual Expansion Nozzles vs. Boiler Temperature. The pump speed for both nozzle designs increase with boiler temperature to 175°C. Above this temperature the dual expansion nozzle maintains a high pump speed, whereas the pump speed for the single-expansion nozzle falls off.

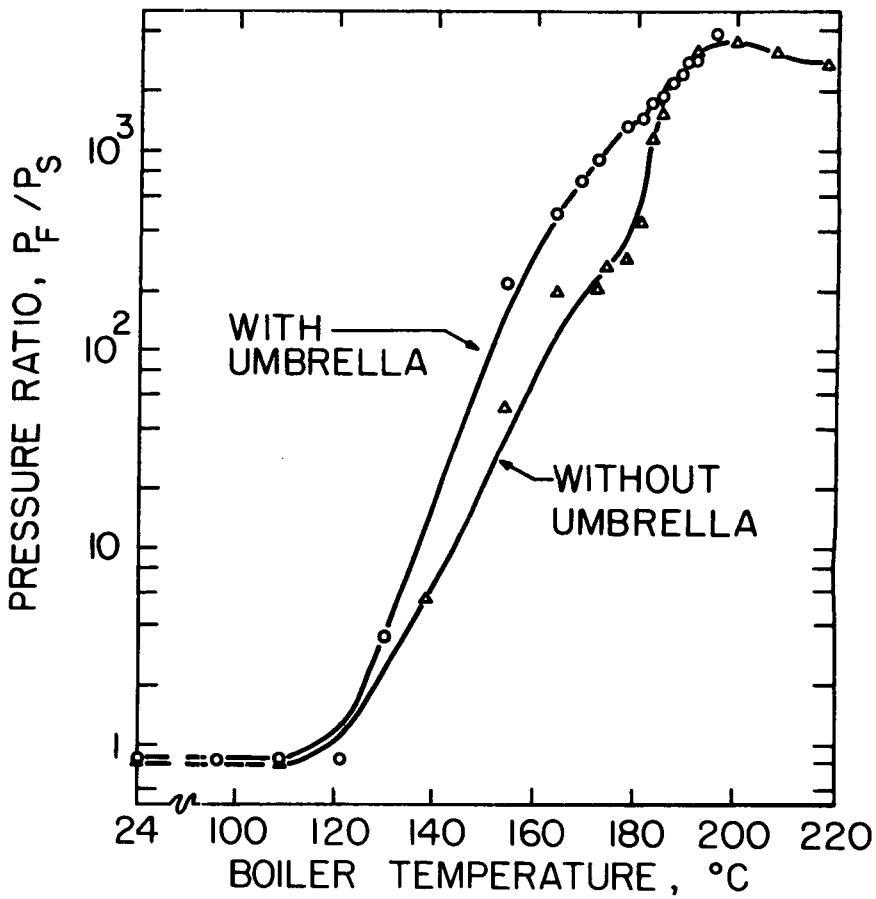

Figure 26 - Pressure Ratio Maintained Across the Jet Region for Both Nozzles vs. Boiler Temperature. Note that the maximum pressure ratio has been established at 195°C.

therefore, a turbulent flow has been established within the jet. Note that the peak pumping speed for the umbrella configuration is at about the same boiler temperature as for the nonumbrella situation; however, the peak has a greater value and does not fall off in the range presented. This behavior can be explained by noting that the umbrella jet has not yet reached a density sufficient to set up a turbulent flow condition; therefore, incoming gases are initially interacting with a more uniform flow condition than would be encountered if they interacted initially with the main jet.

The desirability of operating the main jet at a density corresponding to a turbulent flow condition can be deduced from the pressure ratio curve. At boiler temperatures below 195°C, the pressure ratio which can be maintained across the jet region has not yet peaked for either nozzle configuration. Therefore, to minimize the back diffusion of gases from the high pressure side of the vapor pump, the boiler temperature is above the critical temperature corresponding to a turbulent flow in the main jet stream. However, the over-all pumping speed can be maintained if a low density umbrella jet is established over the main high density jet. The dual expansion nozzle has therefore shown significant improvements over the single nozzle design.

III. EXTREME VACUUM MEASUREMENT TECHNIQUES INCLUDING A FIELD EMISSION MICROSCOPE STUDY AND CALIBRATION OF SELECTED GAUGES EMPLOYING A PENNING DISCHARGE

Extreme vacuum measurement techniques have been severely limited by the lack of pressure standards below the useful range of the McLeod gauge. Under this task, efforts have been made to develop another means to confirm the pressure ratio technique of extending vacuum gauge usefulness into the high and ultrahigh vacuum range, and to determine correction techniques for cold cathode gauges which depart from linearity or even quasi-linearity in the ultrahigh vacuum range. The use of a LN_2 cooled field-emission microscope tip and xenon gas has permitted a determination of mean strike rate of the gas on a surface. The strike rate determination is in agreement with the theoretical striking rate based on corrected cold cathode magnetron gauge (NRC 552) pressure readings. The gauge response vs. pressure for various cold cathode gauges is also presented.

A. Independent Verification of Low Pressure Measuring Techniques by Means of Field Emission Microscope Experiments

A series of field emission microscope experiments were conducted to study the gas dynamics of xenon at low pressures. Small diameter tungsten tips were prepared and a special microscope tube was used with liquid nitrogen cooling of the tip, see Figure 27. Thus, the xenon to tungsten sticking probability was sufficiently high and the rate of xenon gas adsorption from a low pressure gas phase was sufficiently slow to permit the observation of fractional monolayer buildup of xenon.

Tungsten oxide and other contaminants were removed from the tip by the standard technique of resistance heating from the holder. A clean tungsten emission pattern is shown in Figure 28 and the pattern from an oxide coated tungsten tip is shown in Figure 29. The first condition, namely a clean tungsten tip of small diameter, was found to be the best for observing xenon adsorption. Individual spots of enhanced emission were observable on the clean tungsten pattern when a controlled amount of xenon was allowed to adsorb. An estimation of the number of adsorption sites indicated that the emission spots were originating from individual sites.

The time duration of the emission spots was of the order of a few seconds, thus the sticking probability was not unity. To reduce the temperature of the tip a larger diameter holder was used to give improved thermal contact to the buss bar supports. The steady buildup of absorbed xenon was correlated with gas dynamics to give a value for gas pressure as described below.

Data obtained directly from the field emission microscope are in the form of counts per second. That is, the number of new images occurring on a given area of the microscope screen during a given time interval. This data must be converted to a number of strikes on unit area of the emitter tip in unit time so that a gas dynamics calculation of pressure may be carried out. Several parameters must first be determined: The radius of the emitter tips, the magnification ratio of the microscope, and thus the area of tip corresponding to a given area of the screen. A determination of each of these parameters is given below.

The radius of a spherically symmetric electron field emitter may be determined from experimental values for applied voltage and emission current with the aid of the Fowler-Nordheim equation. With values for the tip's radius and the radius of the spherical screen the magnification ratio can be obtained along with the area magnification from tip to screen.

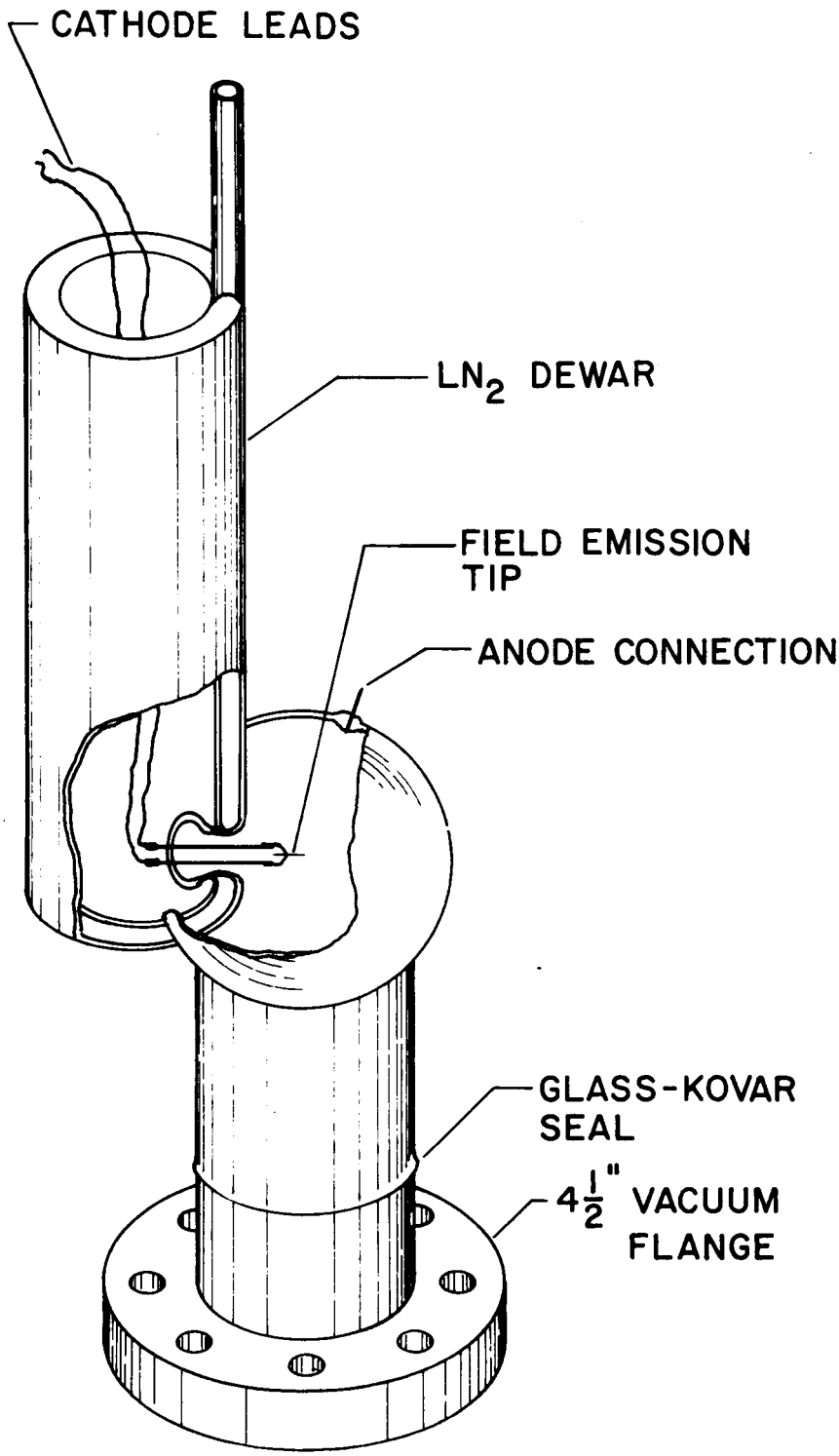

Figure 27 - Electron Field Emission Microscope; Metal Tip May Be Selectively Cooled without Significantly Cooling Inner Wall or Changing Equilibrium Gas Pressure.

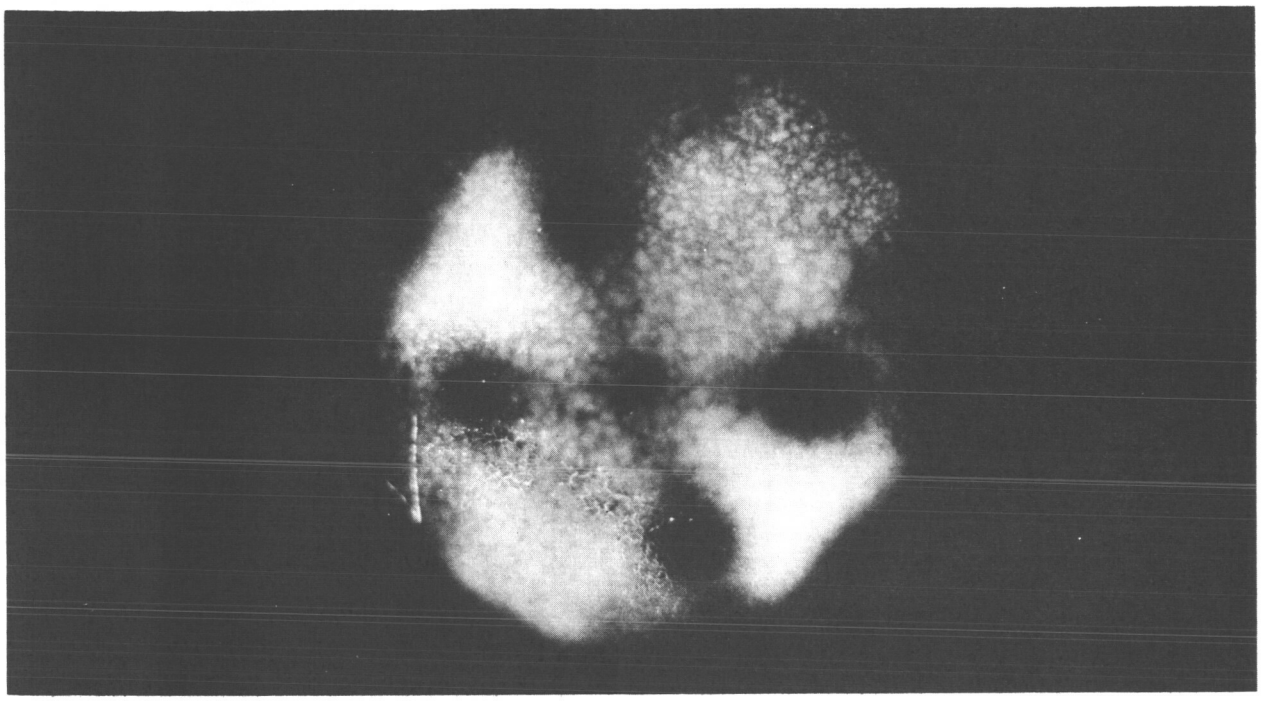

Figure 28 - Electron Field Emission Pattern from a Clean Tungsten Tip

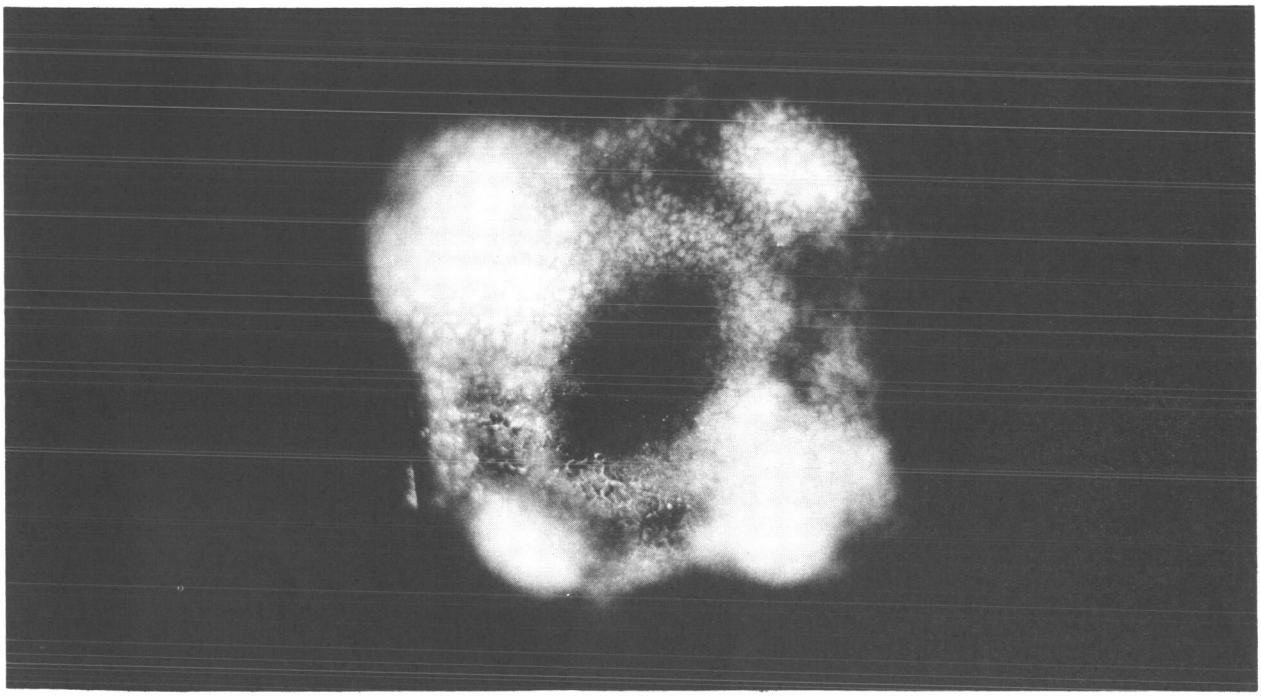

Figure 29 - Emission Pattern of a Tungsten Tip with Oxygen Contamination. Individual spots are due to grains in the fluorescent screen.

The Fowler-Nordheim equation relates field emission current density (i) to: the applied field (F) or voltage (V), the work function (ϕ) and Fermi energy (μ) of the emitter material as follows:

$$i = 6.2 \times 10^6 \frac{(\mu/\phi)^{1/2}}{\mu+\phi} F^2 \exp\left[-6.4 \times 10^7 \frac{\phi^{3/2}}{F}\right] \text{ amp/cm}^2 \quad . \qquad (16)$$

The electric field strength around a spherical conductor of radius (r) with an applied voltage (V) is simply

$$F = V/r$$

and with the Nordheim image correction factor (α) and the field compression factor (k) due to the distortion effect of the shank:

$$F = V/\alpha kr \quad .$$

The field emission current (i) per unit area is given by Eq. (1). When (i) is multiplied by the emitting area (A) a value of total emission current (I) is obtained. A plot of I/V^2 versus $1/V$ is called a Fowler-Nordheim plot. Such a plot may be formed directly from experimental data for total emission current (I) and applied voltage (V). A Fowler-Nordheim plot for one of the tungsten tips used in this experimental program is given in Figure 30.

The field emitter tip radius may be obtained empirically from the plot of Figure 30. The relation for the slope of the Fowler-Nordheim plot is:

$$S = -b' \phi^{3/2}$$

where

$$b' = 6.4 \times 10^7 \alpha kr \quad . \qquad (17)$$

The value 6.4×10^7 is the critical field strength in volts/cm required to draw electron emission from cold tungsten. Equation (17) may be written in terms of the desired tip's radius (r) as follows:

$$r = -S/\phi^{3/2} (6.4 \times 10^7) \alpha k \quad . \qquad (18)$$

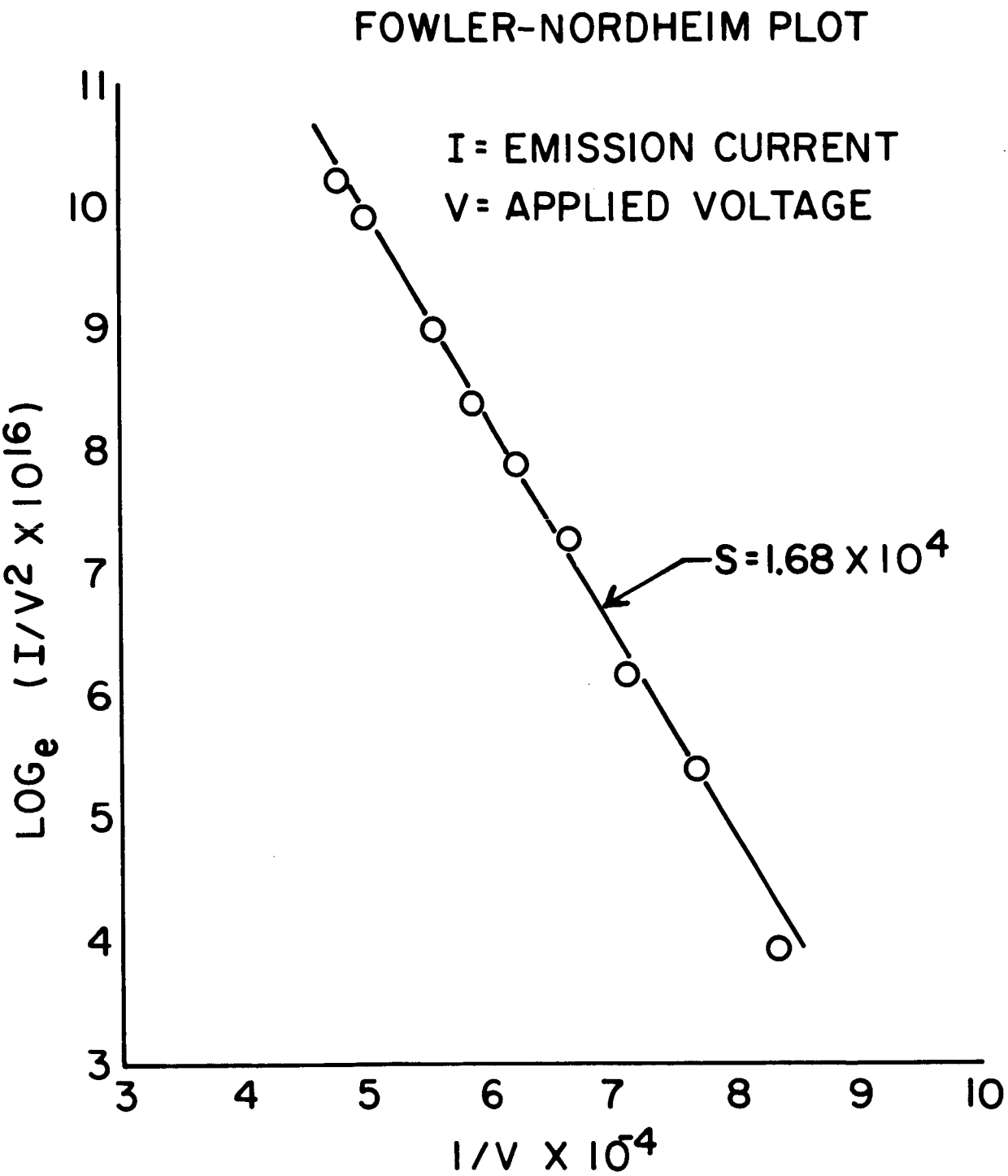

Figure 30 - A Field Emission Plot Which Gives the Necessary Information for a Determination of the Emitter Tip Size.

A value for S was determined by the plot of Figure 30; a value for (ϕ), the work function of tungsten, is given in the literature; and reasonable values for the correction factors α and k are 1 and 5, respectively. Thus the solution for emitter tip's radius from Eq.(18) is:

$$r = 1.68 \times 10^4/(5.96)^{3/2}\ (6.4 \times 10^7)5 \ ,$$

$$= 3.4 \times 10^{-6}\text{cm} = 340\text{Å} \ .$$

The magnification ratio (M) may now be determined by simply assuming rectilinear electron paths from the spherical tip to the concentric spherical screen. The ratio of screen radius (R) to tip radius (r) gives the magnification:

$$M = R/r \ ,$$

$$= 5/3.4 \times 10^{-6} \ ,$$

$$= 1.47 \times 10^6 \text{ times.}$$

The area magnification (M_A) is simply the square of the rectilinear magnification, for the experiment described here

$$M_A = 2.16 \times 10^{12} \text{ times.}$$

The area of the emitter tip (A_T) corresponding to a given area of the screen (A_S) is simply given by

$$A_T = A_S/M_A \ .$$

For the magnification given above a 5 cm^2 area of the screen viewed a tip area of:

$$A_T = 5/2.16 \times 10^{12} \ ,$$

$$= 2.34 \times 10^{-12}\text{cm}^2 \ .$$

The number density of xenon atoms in a given pressure state may be calculated from the ideal gas law:

$$P = nkT \quad . \tag{19}$$

The number density (n) may be written as:

$$n = 9.66 \times 10^{18} \, P/T, \text{ for P in torr.}$$

Using the values 25°C for temperature, 0.33 gauge factor for Xe, and 8×10^{-9} torr for an assumed pressure gauge reading, we obtain:

$$n = 8 \times 10^{7} \text{ molecules/cm}^3 \text{ for the number density.}$$

A gas dynamics calculation will yield a value for the number of molecular strikes on unit area of the emitter tip in unit time. The striking rate is given by:

$$\nu = 1/4 \, n \, \bar{v} \, ,$$

where $\bar{v}$ is the average molecular velocity, and the value for xenon at 25°C is 2.2×10^{4} cm/sec. For the xenon gauge reading of 8×10^{-9} torr, as described above, the striking rate on unit area in unit time is:

$$\nu = 4.4 \times 10^{11} \text{ strikes/cm}^2\text{/sec} \quad .$$

The number of strikes (N_S) on the 5 cm^2 monitored area of the screen is given by

$$N_S = A_T \, \nu \quad ,$$

$$= (2.34 \times 10^{-12} \text{cm}^2) \; (4.4 \times 10^{11} \text{ strikes/cm}^2\text{/sec}) \, ,$$

$$= 1.0 \text{ strike/sec} \quad .$$

A gauge reading for xenon of 8×10^{-9} torr was chosen for this example since it produces the 1/sec striking rate. Experiments were conducted with this value (8×10^{-9}) and multiples thereof so that the following striking rates could be checked: 1 strike/2 sec, 2 strikes/sec, and 3 strikes/sec. Striking rates approximately equal to those predicted by the above method of calculating were observed on the screen area of the field emission microscope. Photographic recordings of the spot images were made, but because of the low intensity (no image intensity amplifier was available) and variations of the images, the recordings were not as useful as visual sightings.

The interesting result from the field emission microscope program is the agreement between this absolute method of observing molecular strikes and the readings from a corrected vacuum gauge at low pressures. The pressure ratio technique was used (Ref. 10) to compare and correct an NRC model 552 Redhead gauge from higher pressures where the absolute McLeod gauge is a valid standard down to low pressure ($\sim 10^{-9}$ torr) where the field emission microscope method is operable. Both ends of the pressure range from 10^{-4} torr to 10^{-9} torr show agreement thus establishing confidence in the pressure ratio method.

B. Response Characteristics for Three Cold Cathode Gauges

A description of cold cathode magnetrons and Penning cells operating as gauges has been developed in terms of the conditions for establishing a discharge and the effects of space charge buildup. Pressure response curves for three commercial gauges (Redhead, Kreisman and trigger discharge types) were determined by a conductance-regulated, pressure-ratio method using Bayard-Alpert type gauges for reference. The pressure-ratio technique was verified by comparison to a field emission microscope standard.

Four characteristics are predicted for magnetrons from a consideration of the discharge mechanism and from a correlation with test data: (1) an out-of-strike state characterized by a steady pressure-independent background reading of about 5×10^{-14} torr; (2) a minimum pressure threshold for operation (2.7×10^{-12} torr for Redhead, 1.7×10^{-10} torr for Kreisman); (3) a range of nonlinear pressure-dependent response above threshold in which the sensitivity rise with pressure is moderated by space charge buildup; followed by (4) a range of near linear response (slope of 1.04 for Redhead, 1.11 for Kreisman types on a log pressure-log current plot) corresponding to the region of nearly saturated space charge. Differences in response values are correlated with differences in electrode elements, spacings, and voltages for the two magnetron gauge tube designs.

Response characteristics have been determined for G.E. trigger discharge gauges. Four characteristics have been identified from test data and described in terms of the discharge process: (1) a pressure insensitive state below 10^{-11} torr in which the predominant current is due to either leakage, field emission, or a combination thereof; (2) a pressure-dependent increase of ion current above 10^{-11} torr; (3) a discontinuous jump (by a factor of about 2) in ion current near the 10^{-9} torr range corresponding to the establishment of an electron cloud virtual cathode, and the conversion to a magnetron type discharge which increases non-linearly with pressure but with space charge moderation along a 1.15 slope; and (4) a saturation phenomenon near 10^{-4} torr due to the establishment of a glow discharge and ion recombinations.

1. Cold cathode gauge operation based on a magnetron type discharge: A Penning type discharge cell (Ref. 11) generally consists of a cylindrical or rectangular anode cage with two end plate cathodes which are not concentric with the anode. The G.E. trigger discharge gauge (Ref. 12) employs a 1/2-in. Penning type cell with some modifications such as a cylindrical rather than a C-shaped magnet and small holes in the end plates for the passage of electrons from a filament mounted just outside of the cell. The operation of a Penning cell such as used in the trigger gauge is similar to that of a magnetron since the electron cloud forms a virtual cathode concentric with the anode. This report therefore concentrates upon the description of magnetron type discharges. This section presents a history and discussion of gaseous discharges as applied to cold cathode vacuum gauge operation.

A magnetron may be defined as an assembly of two concentric cylindrical electrodes operated in an axial magnetic field. When used as a pressure gauge, the electric and magnetic fields are chosen such that the bulk of the cavity is beyond magnetron cutoff. That is, electrons are not able to travel from cathode to anode unless they lose energy by colliding with gas molecules (see Figure 31). The gauge, therefore, remains in an out-of-strike state, unless the gas pressure is high enough to support a discharge. The present report investigates this phenomenon as well as the basic operation of magnetron gauges. There are two commercially available gauges which may be described as magnetrons: the NRC Redhead gauge and the GCA Kreisman gauge.

In 1952, Beck and Brisbane (Ref. 13) reported a series of experiments using both normal and inverted magnetron arrangements. A central wire and a cylinder with several bulkhead discs were employed as electrodes. The sensitivity was high when used as an inverted magnetron. The device had two disadvantages: a background current due to field emission, which was equivalent to about 10^{-8} torr; and a power law rather than a linear relation

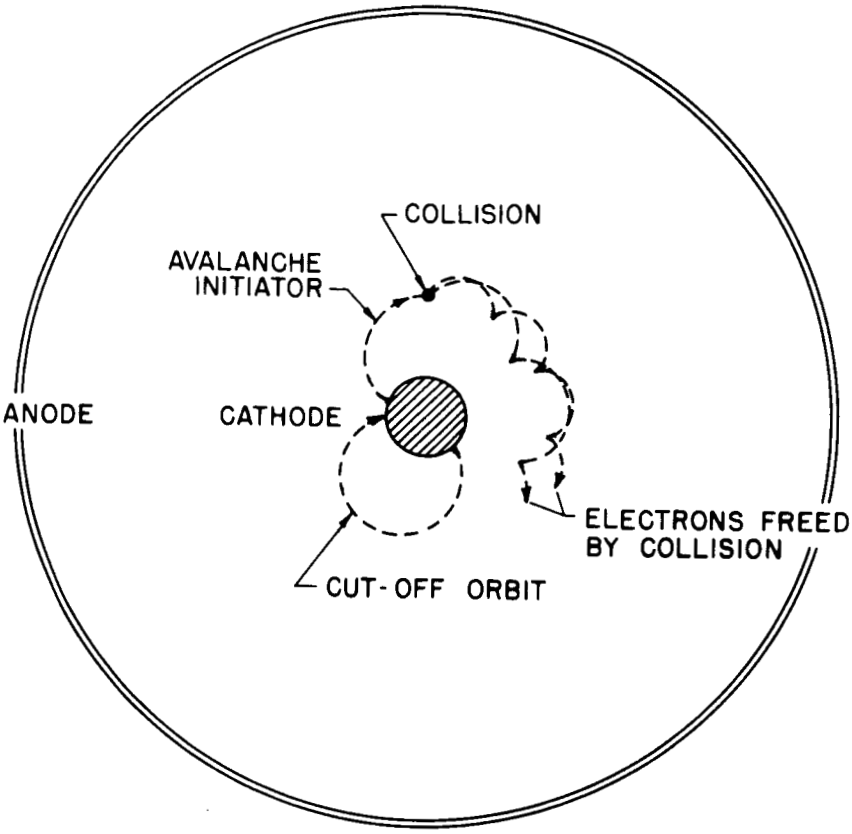

Figure 31 - Electron Orbits in a Coaxial Magnetron Structure. Electrons either return to the cathode or collide with gas molecules to change their momentum and in event of ionizing collisions to release secondary electrons.

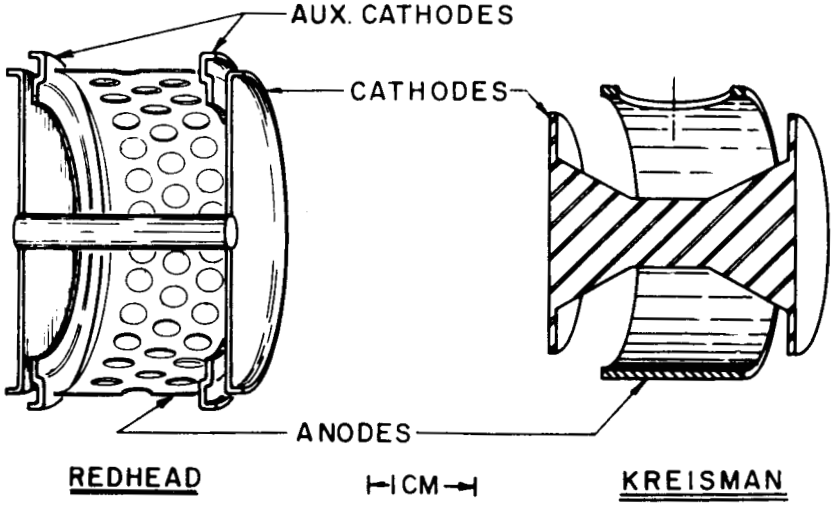

Figure 32 - Electrode Configurations of Commercial Magnetron Gauges, Shown to Scale in Cutaway; Anode Diameters: Redhead 3.0 cm., Kreisman 2.5 cm.

between cathode current and gas pressure. However, a useful gauge circuit was designed using proper resistance values and a nonlinear meter scale.

Haefer (Ref. 14) developed a magnetron for an investigation of striking characteristics of a gaseous discharge in transverse electric and magnetic fields. The magnetron was found to strike at pressures below the sustaining discharge level for Penning cells designed up to that time. Much of the existing theory of magnetron gauge operation has been adapted from Haefer's work, which was based on the assumption of a negligible space charge and a uniform electric field. The first assumption holds only prior to striking, and the second does not hold for the electrode arrangements used in pressure gauges.

The next advance in magnetron pressure gauges was made by Hobson and Redhead (Refs. 15 and 16). They eliminated the recording of erroneous field-emission current from the cathode by inserting auxiliary cathodes into an inverted magnetron structure. These additional electrodes shield the main cathode from the anode. Field emission from the auxiliary cathodes is independent of the ion current recording circuit. Thus an erroneous background reading was avoided. However, the linear response which Beck and Brisbane (Ref. 13) had predicted for operation near 2,500 gauss was not obtained.

Redhead (Ref. 17) also designed a modification of the normal magnetron structure with cathode end plates in contact with the central cathode bar and with large rings as auxiliary cathodes (Figure 32). Thus field emission was again removed from the ion current measuring circuit. A response near linearity (46° slope on a log current -- log pressure plot) from about 5×10^{-10} torr to 10^{-3} torr, and a departure from linearity (59° slope) below 5×10^{-10} torr was found. At extremely low pressures, additional photoelectric action was necessary to insure starting. Using this modified design, Hobson (Ref. 18) reported a limiting pressure measurement of 1.5×10^{-12} torr in a liquid helium-cooled system. The limit was assumed to be due to helium permeation through the walls of the glass system. The data actually appear to be the first published (Ref. 18) indication of the threshold phenomenon as described in this report.

Kreisman has devised several versions of cold cathode normal magnetrons (Refs. 19, 20 and 21) placed in metal envelopes to avoid a breakage problem. One of these models (Ref. 21) (GCA 1410), which does not employ auxiliary cathodes (see Figure 32), is available commercially. Also, the NRC magnetron gauge design was modified for flight tests (Ref. 22) by removing the auxiliary cathodes; a significant alteration of response occurred, as described later.

Rutherford's results (Ref. 9) on the behavior of Penning cells at low pressures show a large change of sensitivity as evidenced by a change of operating mode. These data for Penning cells are similar to the behavior of magnetron gauges at low pressures as reported here. However, the description (Ref. 12) of a triggered Penning cell does not report a similar response.

In this report, the expected characteristics of a magnetron gauge, with the space charge necessary to operate as an ionization gauge are discussed. Then a pressure-ratio technique used to test commercial magnetron gauges is described. The quantitative results of these tests are correlated with the qualitative features expected for space charge limited operation. The pressure response curves are then compared with the design features of the regular Redhead gauge, incorporating auxiliary cathodes, as well as with a special flight gauge and Kreisman design, both without auxiliary cathodes.

Jepsen (Ref. 23) has developed a theory which gives extensive consideration to the existence of a fully developed space charge of uniform density in both normal and inverted magnetron arrangements. The present consideration of space charge buildup with increasing pressure is treated qualitatively since the electron loss mechanisms are not well known. The basic electron loss mechanism has been assumed to be their arrival at the anode after several collisions. In the extremely high vacuum range, orbital lifetimes of electrons traveling from cathode to anode may extend to hours, (Refs. 14 and 16) if electronic oscillations do not interfere. When the cycloidal behavior of the electrons is considered, these long lifetimes and the velocity differences of the electrons could lead, for example, to slipping stream instabilities which could return some electrons to the cathode and send others to the anode without the electron-molecule interactions postulated in the Townsend discharge theory.

Redhead has further investigated (Ref. 24) the "region of instability" reported earlier (Ref. 17). Two operating states are reported for magnetic fields above and below a critical value. RF oscillations were found in the higher field state and sporadic noise in the lower or normal state. The maintenance of a maximum value of space charge was found in the linear response region. These important discoveries (Ref. 24) emphasize the role of space charge effects upon magnetron operation.

The qualitative picture of space charge moderated operation of a magnetron gauge will now be given. At sufficiently low pressure, electron loss mechanisms exceed the pressure dependent source of electrons to preclude the maintenance of a discharge. However, a background current (due to insulator leakage) gives an indicated pressure reading. These low pressure indications are not affected by removal of the magnet, a fact which confirms the lack of ion current in this cutoff state.

Electrons emitted from the cathode will describe short cutoff orbits starting from and ending on the cathode. (As Redhead (Ref. 17) indicates, these paths can cover a significant part of the cathode-anode distance.) However, the electron density in the gauge volume will be negligible until the number of electron-molecule interactions becomes significant.

For pressure values above a lower operating threshold, there are enough gas phase collisions to release electrons to cathode-independent paths at a rate which exceeds the total loss rate. A space charge then begins to build (see Figure 31). The ions produced are detected at the cathode and the electrometer reading will change rather suddenly from a steady background value to a threshold ion current plus background reading when the discharge strikes.

As the space charge increases, the secondary electrons caused by ion bombardment of the cathode cylinder will see a lower electric field; and, although the number should increase with increasing ion current, the maximum kinctic energy in a complete cycloidal arc and the arc length will be reduced. The increase of space charge may eventually lead to a complete inactivation of the central portion of the cathode as an electron source. Thus, the cathode end plates or cones (Figure 32) become increasingly important in defining the gamma coefficient for the discharge as pressure increases.

Finally, the electron space charge saturates and becomes nearly pressure independent so that a near constant gas ionization probability is maintained for further pressure rise. Thus the basically pressure-dependent discharge is constrained by saturation to be constant and produce a linear ion current to pressure response. The onset of this desirable feature near 10^{-9} torr defines the transition from nonlinear to linear response.

In summary, we would expect magnetron gauge operation to exhibit the following characteristics as pressure rises: (1) absence of a discharge below some low pressure level; (2) a threshold ion current at a pressure dependent on gauge geometry and voltage; (3) a greater-than-linear rise of ion current with pressure due to the pressure-dependent rise of the electron density itself; and (4) a saturated electron space charge (above about 10^{-9} torr) giving a linear ion current to pressure response.

2. Response curves for Redhead, Kreisman, and trigger discharge gauge types: The characteristic response of ion current to pressure for cold cathode magnetron gauges was determined by a conductance-regulated, pressure-ratio method (Ref. 25). This technique provided continuous operation of a reference Bayard-Alpert type hot-filament ionization gauge

(BAG) located at a pressure two orders of magnitude above the pressure at the test magnetron gauge position (Ref. 3). Thus the linear response of a BAG with constant emission current was used to obtain a continuous plot of the response curve for the magnetron gauges without the necessity of lowering the BAG to the level of residual collector current. The constancy of the pressure ratio was confirmed by using two BAG tubes on either side of the known conductance. Of course, the downstream BAG was then required to operate to a pressure below the X-ray photo current value. When corrections for total residual current were made (using the modulation technique (Ref. 26), changes of the downstream gauge were found to remain linear with changes of the upstream gauge within gauge reading error.

The characteristic current-to-pressure response for each type studied (G. E. trigger, NRC Redhead, and GCA Kreisman gauges) was determined to its lowest operating value. The pressure-ratio method was employed for each gauge type. In addition, the Kreisman gauges were studied by direct comparisons to BAG, since the commercial BAG type employed (Varian model UHV-12) covers the full operating range of the commercial Kreisman gauge. The response curve for Kreisman gauges determined by direct comparison, with corrections for residual current in the BAG readings, agreed with the response curve obtained by the pressure ratio method. No correction for residual current in the BAG was required for the set of pressure ratio data, since the two order-of-magnitude ratio permitted operation to the low pressure limit of the Kreisman gauge without operating the BAG below 10^{-8} torr.

Output currents from the BAG, used as reference gauge, and the cold cathode gauges were simultaneously plotted on a uniform time base, established by operating a two-channel, strip-chart recorder using the recorder output terminals from the commercial control units. Ion currents and background currents were measured with a Cary model 35 vibrating reed electrometer. High voltages were set at the specified values of 4,800 volts for the Redhead type, 4,000 volts for the Kreisman type and 2,000 volts for the G. E. trigger type and regularly monitored with a sensitive Electrostatic Voltmeter. Magnetic field strengths of the permanent magnets were also checked periodically with a gauss meter and found to remain near the specified values. The BAG tubes (Varian model UHV-12) were operated with a grid potential of 130 volts, and an emission current of 4 ma, so that the sensitivity was 25/torr. Therefore, all operating parameters were carefully maintained at the values specified by the manufacturers of each type gauge tube.

The characteristic response curves, determined from a large amount of data using the methods described above, are plotted in Figures 33 through 38.

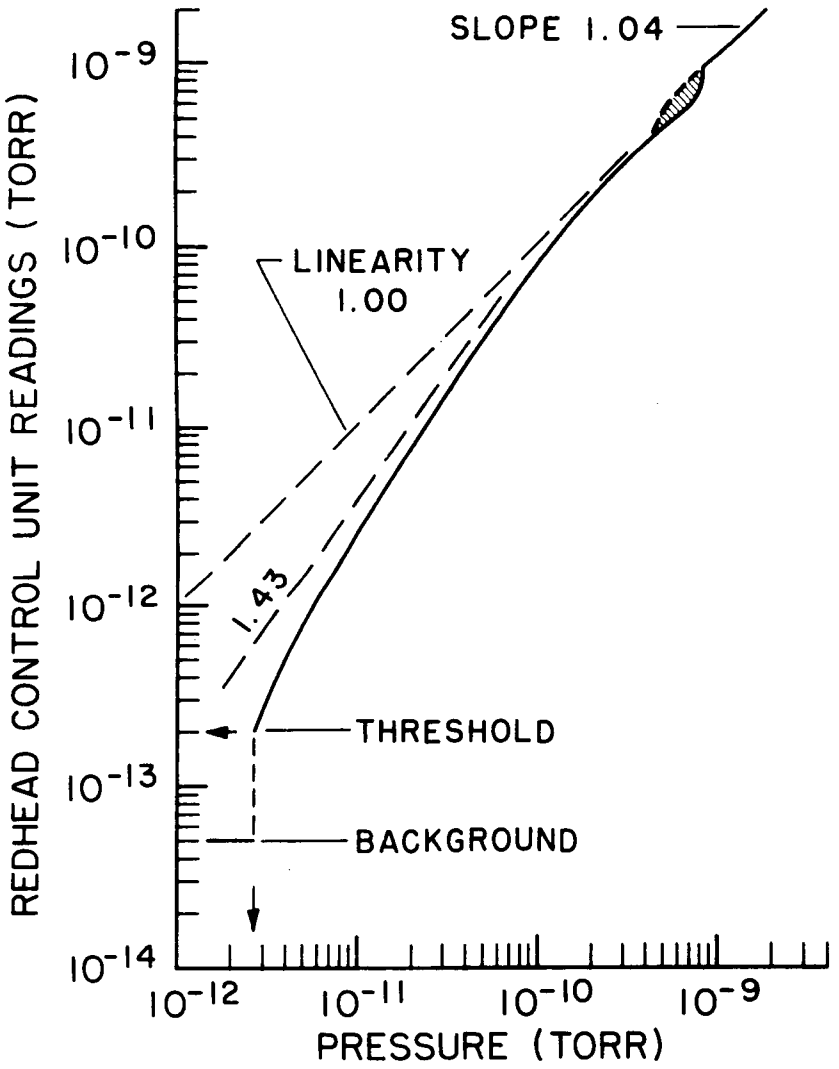

Figure 33 - Characteristic Response of Clean Redhead (NRC 552 glass envelope) Gauges. Ultrahigh vacuum range shows: a background reading below threshold; a sensitivity rise with pressure; an unstable region around 7 x 10^{-10} torr; and a near linear response above the unstable region.

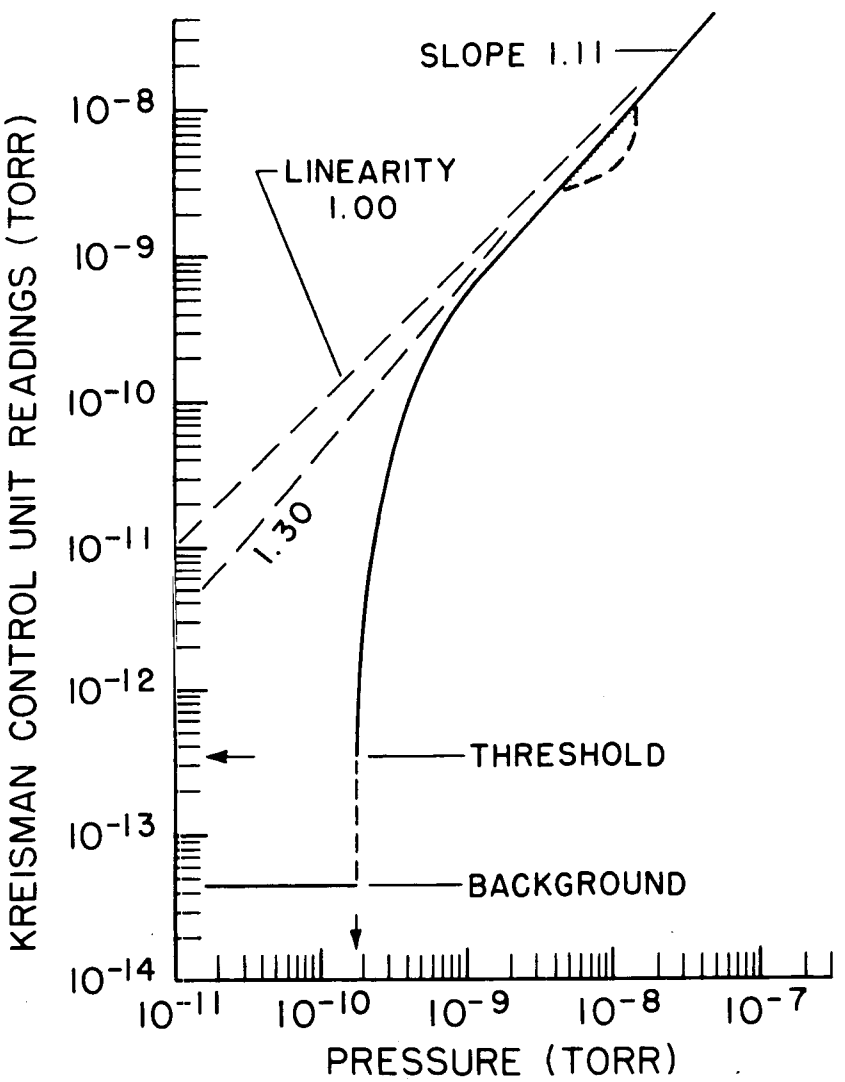

Figure 34 - Characteristic Response of Clean Kreisman (GCA) 1410 Gauges. Ultrahigh vacuum range shows: a background indicating 10^{-14} torr range for pressures below threshold of 1.7 x 10^{-10} torr; a rapid buildup; a possible unstable region near 10^{-8} torr; and a steady sensitivity rise along a 1.11 slope.

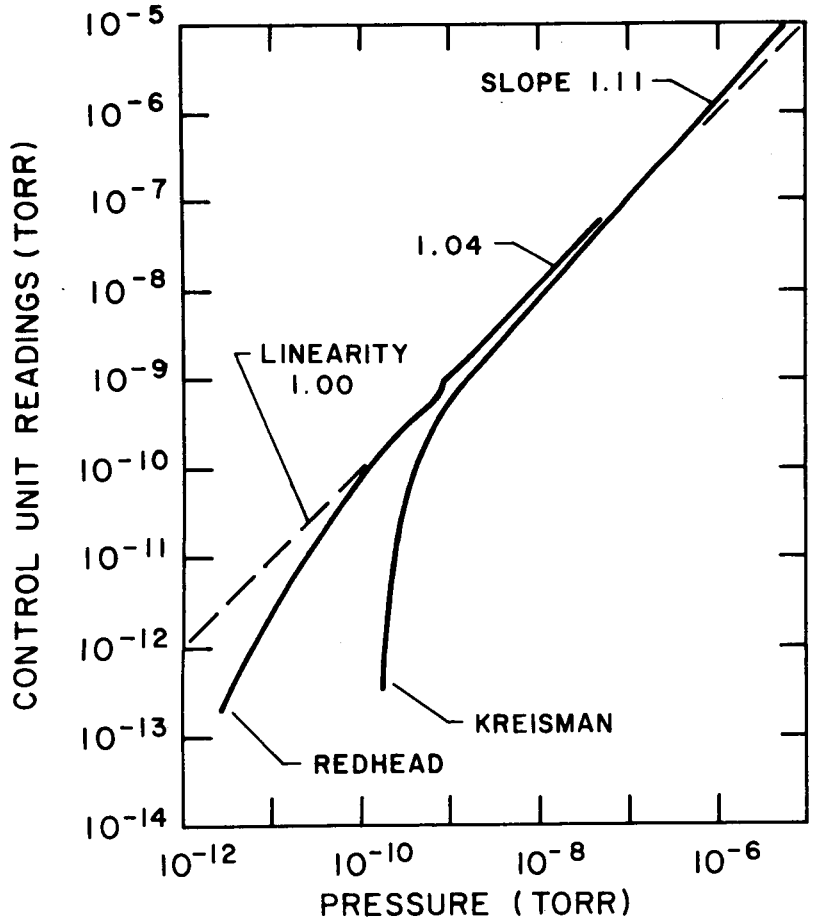

Figure 35 - Characteristic Response Curves for Two Magnetron Gauge Models (upper portion of Redhead curve omitted) Showing Differences Which Result from Variations in the Designs.

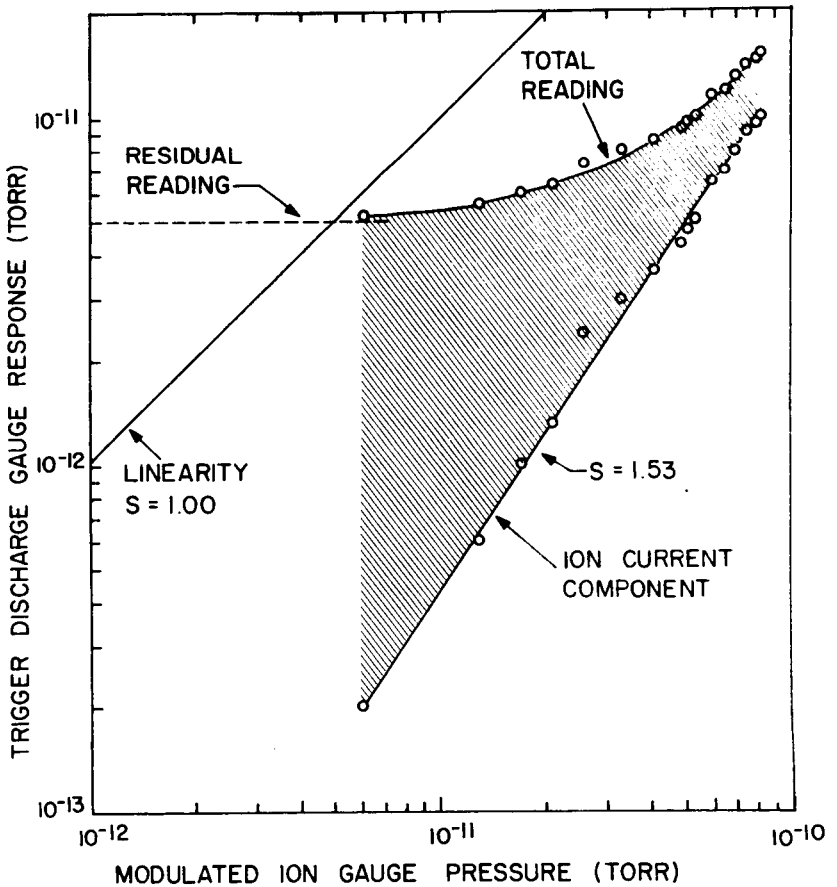

Figure 36 - An Example of Trigger Discharge Gauge, TDG, (G. E. Model 22 GT 214) Response Showing an Asymptotic Approach to a Residual Reading Which Distorts the Ion Current Response. Correction for the apparent background reading gives an estimate of ion current; other TDG tests may vary as indicated in Figure 37.

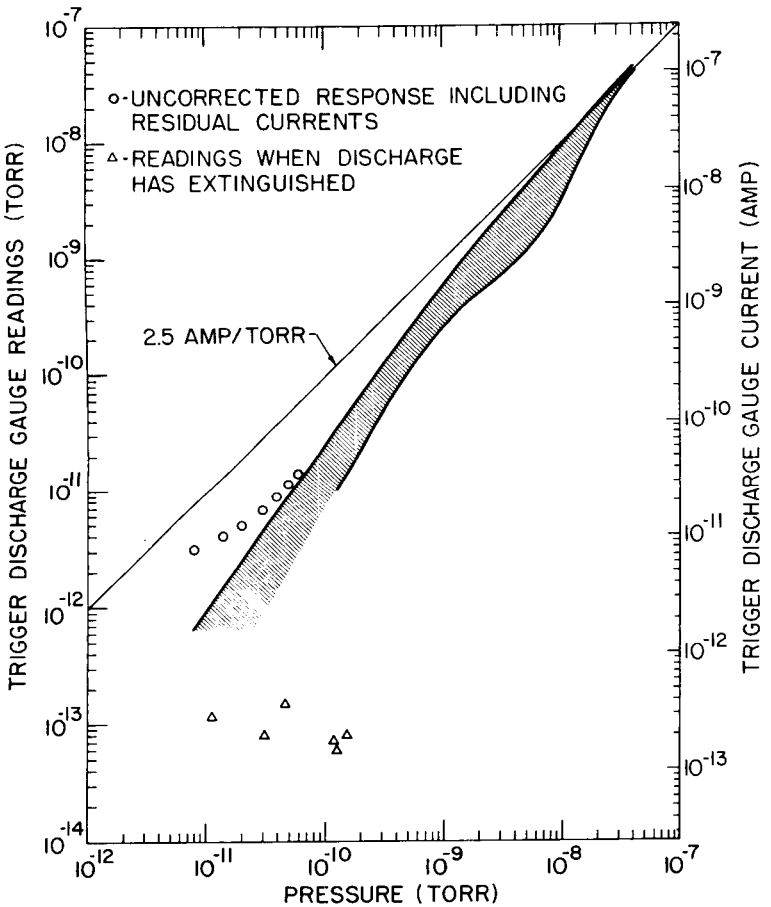

Figure 37 - TDG Response for the UHV Range; the Ion Current Component Lies within the Shaded Region; Residual or Background Currents Can Give Higher Total Readings, e.g., see Circular Data Points; Loss of the Discharge and Ion Current May Give Lower Readings, e.g., see Triangular Data Points.

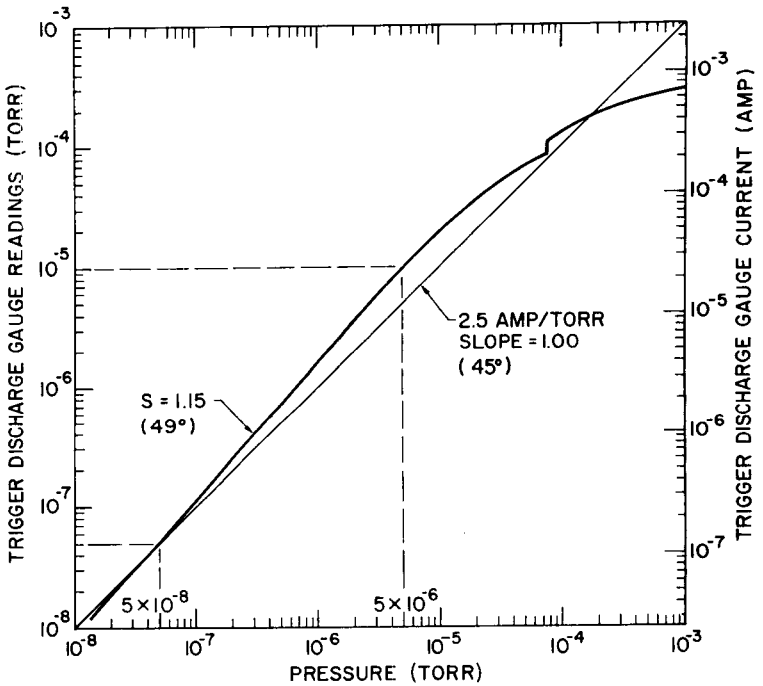

Figure 38 - TDG Response Above 10^{-8} Torr Giving Direct Readings from Gauge Control Unit with 2.5 Amp/Torr Sensitivity. The nonlinear TDG readings reach a factor of two greater than linear response around 5 x 10^{-6} Torr, then approach saturation above 10^{-4} Torr.

Actual pressure values in dry air equivalent are plotted on the abscissae, and indicated pressures from the cold cathode gauge control units are plotted on the ordinates. Ordinate values may be converted to ion current values by multiplication with the dry air sensitivity factors (4.5 amps/torr for the NRC 552 gauge, 2.0 amps/torr for the GCA 1410 gauge and 2.5 amps/torr for the G. E. trigger discharge gauge), since the control unit circuits (NRC 752, GCA 1400, and G. E. 22GC 201) are designed on the assumption of linear response, i.e., constant sensitivity.

The ultrahigh vacuum portion of the response curve for NRC type 552 glass envelope (Redhead) gauges (Figure 33) shows the following characteristics: (1) a background leakage current corresponding to an indicated pressure reading of 5×10^{-14} torr when the real pressure is below the threshold for operation; (2) a total current value of 9×10^{-13} amps for initiation of a sustaining discharge; this threshold level corresponds to an indicated pressure of 2×10^{-13} torr and a real pressure of about 2.7×10^{-12} torr; (3) a non-linear response curve for values above threshold with a continuously changing slope approaching linearity near 10^{-9} torr; this is presumably due to the continuous buildup of space charge toward a saturated value, i.e., the sensitivity of the gauge increases as space charge increases until a nearly saturated state is reached at 10^{-9} torr; (4) a region of instability or resonance around 7×10^{-10} torr characterized by oscillations in the output current; and (5) a response curve above 10^{-9} torr which has a nearly linear slope of 1.04 with a slow rise in sensitivity, due to additional buildup of the essentially saturated space charge. The 46° slope reported by Redhead (Ref. 17) for the response curve above 10^{-10} torr is essentially identical to the value given here. The data below 10^{-10} torr agree closely with the data points given by Feakes and Torney (Ref. 27), except for two differences of interpretation: (1) a theory invoking space charge buildup and saturation is proposed to explain the continuously moderated response, rather than fitting straight line segments to the data; and (2) the pressure-independent readings below 10^{-12} torr are ascribed to leakage current in an out-of-strike state rather than to ion current. The data presented in Figure 33 represent the response of clean Readhead gauges operated with the recommended potential of 4,800 volts and a magnetic field of 1,040 gauss.

The ultrahigh vacuum portion of the response curve for clean GCA Model 1410 (Kreisman) gauges (Figure 34) shows the following characteristics: (1) a background leakage current corresponding to an indicated pressure reading of about 4.5×10^{-14} torr for any real gas pressure value below 1.7×10^{-10} torr; i.e., for pressures below operating threshold, the gauge remains in the out-of-strike state; (2) a total current value of 7×10^{-13} amps for initiation of a discharge; this threshold level corresponds to an indicated pressure reading of 3.5×10^{-13} torr and a real pressure of 1.7×10^{-10} torr; (3) a nonlinear response curve for values above threshold with

a continuously moderated slope, due to the self-moderation of space charge buildup; (4) a region of instability around 10^{-8} torr; and (5) a sensitivity above 10^{-8} torr which continues to increase with pressure along a response curve of slope 1.11; thus a linear response is not achieved over any portion of the pressure range. This latter feature is also found (Ref. 22) for a Redhead flight gauge from which auxiliary cathodes have been removed.

Kreisman reported (Ref. 21) the current-pressure characteristics of two standard GCA Model 1410 gauges. The first gauge exhibited linear response over one decade of pressure from 5×10^{-8} to 5×10^{-7} torr. The second gauge gave a nonlinear response curve (of slope 1.10) for the pressure range from 6×10^{-9} to 1×10^{-6} torr, no data were given for pressures below the 10^{-9} torr range. Thus, the data in the range reported (Ref. 21) for the second gauge agree with the response curve, Figure 34, given here.

The threshold phenomenon may be repeatedly observed by raising and lowering the real pressure around the value necessary to sustain a discharge, i.e., 2.7×10^{-12} torr for NRC 552 and 1.7×10^{-10} torr for GCA 1410 gauges. To accomplish small pressure changes around the threshold values, the helium flow rate was slightly increased and decreased by varying the Vycor-helium diffuser temperature. Although the small pressure changes are recorded by the reference ion gauge, large step-wise changes from the background to the threshold value are indicated by the magnetron gauges. In addition, the magnetron gauges do not respond to pressure changes below their threshold pressure levels; i.e., the steady background leakage current values are indicated without an ion current component for all pressures below the threshold level.

Qualitatively, at least, the threshold phenomenon may be thought of in terms of the minimum number of avalanche initiating electrons required for a sustaining discharge. Figure 31 illustrates the process by which electrons may escape from the cathode and enter the trapping region as avalanche initiators. An avalanche initiating electron may make an ionizing collision, for example, with a gas molecule, and lose sufficient energy so that it will travel in an approximately hypercycloidal path which does not intersect the cathode. The secondary electron produced by the ionization normally is also trapped in the discharge. However, for magnetron devices operated below cutoff, as is the case for both gauges discussed herein, electrons emitted from the cathode will execute approximately hypercycloidal paths which intersect the cathode on the first orbit (see Figure 31) unless a collision occurs, leading to a high probability of recapture. For the electric and magnetic field values employed in these gauges, an avalanche will not develop unless a sufficient number of gas molecules exists inside the anode cage to provide the threshold number of avalanche initiating collisions.

The total cathode current corresponding to threshold for the magnetron gauges is between 7 and 9 x 10^{-13} amps, including currents from avalanche initiating electrons, ions and background. Since this total value is four to seven times greater than the background alone, there is a clearly distinguishable difference between operation of the gauges above and below threshold. Even the cleanest tubes exhibit this threshold phenomenon.

The real pressure corresponding to threshold is about 60 times different for the two magnetron designs (see Figure 35), which suggests a possible difference in the number of electrons available for avalanche initiation. Differences between at least two parameters of these gauges lead to a prediction of different electric field values at the cathode surfaces: (1) the recommended operating potential is 800 volts lower for the GCA 1410 gauge; and (2) the central cathode radius is about double that used in the NRC 552 gauge (see Figure 32). Whether or not these differences alone are sufficient to account for the difference in threshold pressures is an open question.

The continuously modified, nonlinear-response curve above threshold and the approach to linear response due to space charge saturation are two additional qualitative characteristics observed experimentally for both magnetron gauges. However, we again note that quantitative values are different (see Figure 35) for the two commercial designs. The nonlinear response above the threshold is steeper for the Kreisman tube, beginning with a slope of about 14 and reaching 1.11, whereas the Redhead response curve begins with 2.2 and reaches a nearly linear slope of 1.04. These differences may be viewed alternatively in terms of an increase with pressure of the ionization probability or the number of ionizing electrons in the contained discharge.

The containment of space charge appears to be relevant to the attainment of linear response. The unique feature of auxiliary cathodes in the Redhead design permits a much closer spacing between cathode and anode electrodes; thus, the anode cage is tightly enclosed electrostatically and the space charge is apparently contained within this fixed volume at a more closely saturated value. It is interesting to note, in closing, that calibration of the flight model NRC magnetron design (Ref. 22), in which no auxiliary cathodes are used gave a response curve with a slope of 1.15. That is, the flight model magnetron response was similar to the 1.11 slope of the Kreisman design for normal operation above 10^{-10} torr. Thus the data for flight gauges (Ref. 22) and Kreisman gauges both without auxiliary cathodes show only an approach to saturation and linearity. On the other hand, the response (1.04 slope) of regular Redhead gauges with auxiliary cathodes and the electrostatically tight anode cage which results exhibits almost complete fulfillment of the space charge saturation hypothesis for linear response, which is described in this report.

The Redhead and Kreisman gauge designs may be described as magnetrons operated below cutoff since electrons may not energetically travel from cathode to anode without gas molecule interactions. A residual electron current across the electrode gap is forbidden in these designs by the electrode and magnetic field arrangements.

The trigger discharge gauge arrangement does not absolutely exclude electron flow from cathode to anode. Electrons may travel parallel to the magnetic field from the cathode plates to the edge of the anode cylinder, a distance of 0.8 mm. Earlier Penning cell designs were limited by such a residual current background; however, the trigger discharge gauge appears to be operating at the threshold for such residual current. The individual condition and history of a gauge tube can significantly affect the residual current. Thus the operation of a magnetron gauge generally yields a recognizable drop at the low pressure end, as seen in Figures 33, 34, and 35, corresponding to a loss of ion current. Whereas, trigger gauge operation is often confused by residual current as seen in Figure 36.

Two general cases exist for the trigger discharge gauge response below 10^{-9} torr. In the first case the tube loses the ion current component near 10^{-10} torr and drops to a background current of about 10^{-13} amps (see Figure 37). The second case in which ion current is maintained for gas pressures below 10^{-10} torr is characterized by the presence of some spurious current, Figures 36 and 37. Ion current is present whenever the discharge exists as should be expected. In the second case another source of current becomes significant. This source is in addition to the leakage current background. The probable sources for this erroneous current are electron field emission from cathode to anode and secondary electron emission from the cathode under ion bombardment. Figures 36 and 37 show the variations which may occur in the trigger discharge gauge response. No single response curve is followed for pressures below 10^{-8} torr. Figure 38 gives a response curve for pressures above 10^{-8} torr showing a nonlinear increase of ion current with pressure until a glow type discharge and ion recombinations limit response near 10^{-4} torr.

IV. RESULTS AND CONCLUSIONS

The results of this research program can be readily applied to the two major areas of concern in UHV technology: (1) the production of evacuated environments and (2) the measurement of the degree of evacuation which exists within each environment.

In the area of evacuation, we have studied three techniques: cryopumping, getter-ion pumping, and diffusion pumping. The following major conclusions can be drawn from the vacuum pumping studies:

1. Cryopanels of type 304 stainless steel operating at 4.2°K can be used effectively to pump helium gas. Saturation of the panel for extreme-high vacuum ($< 5 \times 10^{-11}$ torr) application begins to occur at approximately one-half monolayer coverage of the panel.

2. Cryopanels of type 304 stainless steel operating in a temperature range of 18 to 21°K can be used to pump hydrogen gas. Saturation of the panel for extreme-high vacuum ($< 5 \times 10^{-11}$ torr) begin to occur at approximately one-half monolayer coverage of the panel.

3. The two pumping modes observed for getter-ion pump at pressure above and below 10^{-8} torr have been related to the discharge activity within the Penning cells of the pump. Above 10^{-8} torr a dense electron cloud (virtual cathode) exists at the center of the cell extending from cathode to cathode. Below 10^{-8} torr the dense electron cloud extinguished and the only remaining major discharge activity is around the periphery of the anode. This latter condition constitutes the second mode of pumping.

4. The pumping speed of a getter-ion pump is not greatly affected by changes in anode voltage between 7,700 v. and 1,000 v. for H, H_2, H_2O, CO, Ar, and CO_2. However, the pumping speed for He and CH_4 increase with increasing anode voltage.

5. Discharges can be established in a getter-ion pump quickly at pressures below 10^{-8} torr by using an anode voltage of at least 4,000 v.

6. A getter-ion pump can be a major source of gas within a system, however, this effect can be greatly reduced by simultaneous baking of the pump with the UHV portions of the system to 400°C while evacuated.

7. The use of a dual expansion nozzle in mercury diffusion pumps permits the operation of the pump at higher boiler temperatures resulting in a 19 to 34 percent increase in pumping speed and a reduction in back diffusion by approximately one order of magnitude for helium gas.

In the area of vacuum measurement, the following major conclusions have been drawn:

1. Images generated by individual molecules have been observed with a field emission microscope (FEM). The arrival rate of molecules at the tip of a FEM can thereby be determined by monitoring the spot patterns which appear on the screen of the FEM.

2. An independent pressure determination has been accomplished by employing a FEM to determine the striking rate of xenon molecules in the 10^{-9} torr range. The pressure can then be calculated by means of applying the kinetic gas theory to the striking rate data.

3. The pressure determined by the FEM has been compared to pressure readings from an NRC Model 552 magnetron gauge. Agreement was found between the striking rate and the gauge reading.

4. The FEM technique is an independent verification of the validity of the various gauge calibration techniques such as the pressure ratio technique which was used to determine the ion current to pressure response characteristics for the NRC Model 552 magnetron used above.

5. Four pressure-dependent discharge characteristics have been observed and identified for magnetron gauge operation. These characteristics are: (a) an absence of a discharge below some low pressure level; (b) a threshold ion current at a pressure dependent on gauge geometry and voltage; (c) a greater-than-linear rise of ion current with pressure due to the pressure-dependent rise of the electron cloud density itself; and (d) a saturated electron space charge (above 10^{-9} torr) giving a linear ion current to pressure response.

6. The pressure response characteristics for a clean NRC Model 552 (Redhead) magnetron gauge operating at 4,800 v. in a magnetic field of 1040 gauss are: (a) a background leakage current corresponding to an indicated pressure reading of 5×10^{-14} torr when the real pressure is below the threshold for operation; (b) a total current value of 9×10^{-13} amps for initiation of a sustaining discharge; this threshold level corresponds to an indicated pressure of 2×10^{-13} torr and a real pressure of about 2.7×10^{-12} torr; (c) a nonlinear response curve for values above threshold with a continuously changing slope approaching linearity near 10^{-9} torr; this is presumably due to the continuous buildup of space charge toward a saturated value, i.e., the sensitivity of the gauge increases as space charge increases until a nearly saturated state is reached at 10^{-9} torr; (d) a region of instability or resonance around 7×10^{-10} torr characterized by oscillations in the output current; and (e) a response curve above 10^{-9} torr which has a nearly linear slope of 1.04 with a slow rise in sensitivity, due to additional buildup of the essentially saturated space charge.

7. The pressure response characteristics for a clean GCA Model 1410 (Kreisman) gauge operating at 4,000 v. in a magnetic field of 1040 gauss are: (a) a background leakage current corresponding to an indicated pressure reading of about 4.5×10^{-14} torr for any real gas pressure value below

1.7×10^{-10} torr; i.e., for pressures below operating threshold, the gauge remains in the out-of-strike state; (b) a total current value of 7×10^{-13} amps for initiation of a discharge; this threshold level corresponds to an indicated pressure reading of 3.5×10^{-13} torr and a real pressure of 1.7×10^{-10} torr; (c) a nonlinear response curve for values above threshold with a continuously moderated slope, due to the self-moderation of space charge buildup; (d) a region of instability around 10^{-8} torr; and (e) a sensitivity above 10^{-8} torr which continues to increase with pressure along a response curve of slope 1.11; thus a linear response is not achieved over any portion of the pressure range.

8. No single response curve can be given for the G. E. trigger discharge gauge for the pressure range below 10^{-8} torr. However, below 10^{-9} torr two general types of response can exist. In the first case the tube loses the ion current component near 10^{-10} torr and drops to a background current of about 10^{-13} amp. In the second case ion current is maintained for gas pressures below 10^{-10} torr, but the gauge response is characterized by the presence of some non-ion current. The probable sources for this erroneous current are electron field emission from cathode to anode and secondary electron emission from the cathode under ion bombardment.

REFERENCES

1. Helmer, J. C., and R. L. Jepsen, Proc. I.R.E., 49, 1920 (1961).

2. Florescu, N. A., Australian J. Appl. Sci., 8, 305 (1957).

3. Bryant, P. J., C. M. Gosselin, and W. W. Longley, NASA CR-324 (1965).

4. Bryant, P. J., C. M. Gosselin, and L. H. Taylor, NASA CR-84 (1964).

5. Taylor, L. H., W. W. Longley, and P. J. Bryant, J. Chem. Phys., 43, 1184 (1965).

6. Simpson, P. A., and A. H. Morgan, N.B.S. Report 6080 (October 1959).

7. Lichtman, D., J. Vac. Sci. Tech., 2, 70 (1965).

8. Dushman, S., and J. M. Lafferty, Scientific Foundations of Vacuum Technique (John Wiley & Sons, Inc., New York, 1962) Table 1.6.

9. Rutherford, S. L., Trans. Natl. Vac. Symp., 10, 185 (1963).

10. Bryant, P. J., W. W. Longley, and C. M. Gosselin, J. Vac. Sci. Tech., 3, 62 (1966).

11. Penning, F. M., Physica, 3, 873 (1936).

12. Young, J. R., and F. P. Hession, Trans. Natl. Vac. Symp., 10, 234 (1962).

13. Beck, A. H., and A. D. Brisbane, Vacuum, 2, 137 (1952).

14. Haefer, R., Acta Physica Austriaca, 7, 52 and 251 (1953); 8, 213 (1954).

15. Redhead, P. A., Can. J. Phys., 36, 255 (1958).

16. Hobson, J. P., and P. A. Redhead, Can. J. Phys., 36, 271 (1958).

17. Redhead, P. A., Can. J. Phys., 37, 1260 (1959).

18. Hobson, J. P., Can. J. Phys., 37, 300 (1959).

19. Kreisman, W. S., and R. Herzog, G.C.A. Technical Report No. 61-18-N (1961).

20. Kreisman, W. S., G.C.A. Technical Report No. 64-8-N (1964).

21. Kreisman, W. S., G.C.A. Technical Report No. 64-17-N (1964).

22. Newton, G. P., D. T. Pelz, G. E Miller, and R. Horowitz, Trans. Natl. Vac. Symp., 10, 208 (1963).

23. Jepsen, R. L., J. Appl. Phys., 32, 2619 (1961).

24. Redhead, P. A., Can J. Phys., 43, 1001 (1965).

25. Roehrig, J. R., and J. C. Simons, Trans. Natl. Vac. Symp., 8, 511 (1961).

26. Redhead, P. A., Rev. Sci. Instr., 31, 343 (1960).

27. Feakes, F., and F. L. Torney, Trans. Natl. Vac. Symp., 10, 257 (1963).

	Addressee	No. of Copies
80.	Atomic Energy Commission Research Division Washington, D. C. 20025 Attn: W. C. Gough	1
81.	Rome Air Development Center Headquarters--Air Force Systems Command Griffiss AFB, New York 13442 Attn: RALTP	1
82.	U. S. Naval Postgraduate School Monterey, California 93942 Attn: Professor N. L. Oleson	1
83.	Swiss Federal Institute of Technology Zurich, Switzerland Attn: The Library	1
84.	Nagoya University, Chikusa-ku Institute of Plasma Physics Nuclear Fusion Research Group Research Information Center Nagoya, Japan Attn: Y. Y. Terashima	1
85.	Air Force Plant Representative Hughes Aircraft Company Culver City, California 90230 Attn: RWRAAC-2 RWRAPS-9	1 1
86.	Airospace Power Division Wright Patterson AFB, Ohio 45433 Attn: Jack W. Geis-AFAPL/APIT	1

	Addressee	No. of Copies
72.	SED Laboratories 800 Rahway Avenue Union, New Jersey 07083 Attn: J. A. Sloom	1
73.	S.E.R.L. (Admiralty) West Road Harlow Essex, England Attn: M. O. Bryand	1
74.	University of Sheffield Department of Electrical Engineering Mappin Street Sheffield 1, England Attn: A. L. Cullen	1
75.	Services Electronics Research Laboratories Baldock, Herts, England Attn: Dr. Boot	1
76.	Standard Telephone Laboratories Harlow, Essex, England Attn: E. A. Ash	1
77.	U. S. Atomic Energy Commission Oak Ridge, Tennessee 37830 Attn: Dr. Luce	1
78.	The University Department of Electrical Engineering Mayfield Road Edinburgh 9, Scotland Attn: Dr. B. Meltzer	1
79.	Auburn University Department of Electrical Engineering Auburn, Alabama 36830 Attn: C. H. Holmes	1

	Addressee	No. of Copies
64.	University of Michigan 3506 East Engineering Building Ann Arbor, Michigan 48106	
	Attn: Electron Tube Laboratory	1
	R. J. Leite	1
65.	Microwave Associates, Inc. Burlington, Massachusetts 02103	
	Attn: M. Allen	1
66.	The Royal Institute of Technology Stockholm 70, Sweden	
	Attn: B. Agduv	1
67.	Stevens Institute of Technology Department of Physics Hoboken, New Jersey 07030	
	Attn: W. H. Bostick	1
68.	University of Washington Department of Electrical Engineering Seattle, Washington 98105	
	Attn: H. Golde	1
69.	Bell Telephone Laboratories Murray Hill, New Jersey 07971	
	Attn: Dr. Buchsbaum	1
70.	University of British Columbia Department of Electrical Engineering Microwave Laboratory Vancouver 6, British Columbia, Canada	1
71.	Boeing Scientific Research Laboratories Boeing Airplane Company Plasma Physics Laboratory P. O. Box 3707 Seattle, Washington 98124	
	Attn: J. W. Drummond	1

	Addressee	No. of Copies
55.	Litton Industries Beverly Hills, California 90213 Attn: A. S. Penfold	1
56.	Space Sciences Corporation Natick, Massachusetts 01760 Attn: A. Winston	1
57.	Lockheed/Missile Systems Division Palo Alto, California 94301 Attn: D. Berghader	1
58.	Astronautics Newport Beach, California 92660 Attn: S. R. Bryon	1
59.	General Electric Company Missile and Space Division Space Sciences Laboratory P. O. Box 8555 Philadelphia, Pennsylvania 19101 Attn: P. Gloevsen	1
60.	California Institute of Technology 1201 East California Street Pasadena, California 91109 Attn: Professor R. W. Gould	1
61.	University of California Laurence Radiation Laboratory Livermore, California 94550 Attn: S. A. Colgate	1
62.	University of California Radiation Laboratory Berkeley, California 94720 Attn: R. K. Wakerling	1
63.	University of Illinois Department of Electrical Engineering Urbana, Illinois 61801 Attn: L. Goldstein	1

	Addressee	No. of Copies
46.	Case Institute of Technology 10900 Euclid Avenue Cleveland, Ohio 44106 Attn: Professor O. K. Mawardi	1
47.	Rensselaer Polytechnic Institute Troy, New York 12180 Attn: E. H. Holt	1
48.	Northrop Corporation Hawthorne, California 90250 Attn: P. Lenn	1
49.	Astrosystems, Inc. 82 Naylon Avenue Livingston, New Jersey 07039 Attn: R. E. Wiech, Jr.	1
50.	Reaction Motors Division Thiokol Chemical Corporation Denville, New Jersey 07834 Attn: W. Courtney	1
51.	Grumman Aircraft Engineering Corporation Bethpage, Long Island, New York 11101 Attn: P. Grinoch	1
52.	The Martin Company P. O. Box 5837 Orlando, Florida 32801 Attn: Engineering Library MP30	1
53.	Space Sciences, Inc. 301 Bear Hill Road Waltham, Massachusetts 02154 Attn: J. M. Proud	1
54.	AVCO Corporation Research and Advanced Development Division 201 Lowell Street Wilmington, Massachusetts 01887 Attn: R. R. John	1

	Addressee	No. of Copies
38.	Massachusetts Institute of Technology Naval Supersonic Laboratory Cambridge, Massachusetts 02139 Attn: E. E. Covert	1
39.	Astro-Electronics P. O. Box 800 Princeton, New Jersey Attn: W. H. Hendel	1
40.	General Technology Corporation 3510 Torrance Boulevard Torrance, California 90503 Attn: S. Ridgeway	1
41.	Republic Aviation Corporation Plasma Propulsion Laboratory Farmingdale, Long Island New York 11735 Attn: A. Kunen	1
42.	United States Air Force Office of Scientific Research Washington, D. C. 20025 Attn: M. Slawsky	1
43.	Naval Research Laboratory Washington, D. C. 20025 Attn: A. C. Kolb	1
44.	Office of Naval Research Power Branch - Room 2509 Washington, D. C. 20025 Attn: J. A. Sotkowski	1
45.	Cornell University Graduate School of Aeronautical Engineering Ithaca, New York 14851 Attn: E. L. Resler, Jr.	1

	Addressee	No. of Copies
30.	North American Aviation, Inc. 12214 Lakewood Avenue Downey, California 90241 Attn: Technical Information Office Department 4096-314	1
31.	NASA-Langley Research Center Langley Field Station Hampton, Virginia 23365 Attn: Technical Library	1
32.	Colorado State University Fort Collins, Colorado 80521 Attn: L. Baldwin	1
33.	Rocketdyne 6633 Canoga Avenue Canoga Park, California 91304 Attn: J. F. Hon	1
34.	MSA Research Corporation Callery, Pennsylvania 16024 Attn: R. C. Werner	1
35.	U. S. Atomic Energy Commission P. O. Box 62 Oak Ridge, Tennessee 37830 Attn: Division of Technical Information Extension	1
36.	AVCO-Everett Research Laboratory A Division of AVCO Corporation 2385 Revere Beach Parkway Everett, Massachusetts 02149	1
37.	Allison Division General Motors Corporation Indianapolis, Indiana 46206 Attn: T. Rosebrock	1

	Addressee	No. of Copies
22.	NASA-Ames Research Center Moffett Field, California 94035 Attn: T. W. Snouse	1
23.	Astro Met Associates, Inc. 500 Glendale-Milford Road Cincinnati, Ohio 45215 Attn: J. W. Graham	1
24.	Princeton University Department of Aeronautical Engineering Princeton, New Jersey 08540 Attn: Professor J. B. Fenn	1
25.	University of California Space Science Laboratory Berkeley, California 94720 Attn: H. P. Smith	1
26.	Nuclide Corporation 642 East College Avenue State College, Pennsylvania 16801 Attn: D. V. Marshall	1
27.	The Garrett Corporation Airesearch Manufacturing Division 402 South 36th Street Phoenix, Arizona 85034 Attn: L. Six	1
28.	United Aircraft Corporation Research Laboratories East Hartford, Connecticut 06108 Attn: R. G. Meyerand, Jr.	1
29.	Aerojet-General Nucleonic Division San Ramon, California 94583 Attn: J. S. Luce	1

	Addressee	No. of Copies
14.	TRW Inc. New Product Research 23555 Euclid Avenue Cleveland, Ohio 44117 Attn: R. T. Craig	1
15.	General Electric Space Flight Propulsion Laboratory Cincinnati, Ohio 45215 Attn: M. L. Bromberg	1
16.	Hiram College Department of Physics Hiram, Ohio 44234 Attn: Professor L. Shaffer	1
17.	General Dynamics/Convair P. O. Box 1128 San Diego, California 92112 Attn: G. D. Magnuson	1
18.	Field Emission Corporation 611 Third Street McMinnville, Oregon 97128 Attn: L. W. Swanson	1
19.	Litton Precision Products 910 Industrial Road San Carlos, California 94070 Attn: G. K. Wehner	1
20.	Varian Associates 611 Hansen Way Palo Alto, California 94304 Attn: Technical Library Y. E. Strausser	1 1
21.	Battelle Memorial Institute 505 King Avenue Columbus, Ohio 43201 Attn: J. Anno Defense Metals Information Center	1 1

	Addressee	No. of Copies
6.	AFWL Kirtland AFB, New Mexico 87417 Attn: WLPC/Capt. C. F. Ellis	1
7.	Aerospace Corporation P. O. Box 95085 Los Angeles, California 90045 Attn: Library/Technical Documents Group	1
8.	Jet Propulsion Laboratory 4800 Oak Grove Drive Pasadena, California 91103 Attn: J. J. Paulson	1
9.	Hughes Research Laboratories 3011 Malibu Canyon Road Malibu, California 90265 Attn: G. R. Brewer	1
10.	Electro-Optical Systems, Inc. 300 North Halstead Street Pasadena, California 91107 Attn: I. Katz G. Kuskevics	1 1
11.	Ion Physics Corporation South Bedford Street Burlington, Massachusetts 02103 Attn: Sam Nablo	1
12.	TRW Inc. TRW Systems One Space Park Redondo Beach, California 90278 Attn: H. Shelton	1
13.	Westinghouse Astronuclear Laboratories Electric Propulsion Laboratory Pittsburgh, Pennsylvania 15234	1

DISTRIBUTION LIST FOR FINAL REPORT

CONTRACT NAS3-8914

	Addressee	No. of Copies
1.	National Aeronautics and Space Administration Washington, D. C. 20546	
	Attn: J. W. Keller (RV-1)	1
	Attn: Conrad P. Mook (RV-1)	2
2.	NASA-Lewis Research Center 21000 Brookpark Road Cleveland, Ohio 44135	
	Attn: Spacecraft Technology Procurement Section (M.S. 54-2)	1
	Attn: Technology Utilization Office (M.S. 3-19)	1
	Attn: Technical Information Division (M.S. 5-5)	1
	Attn: Library (M.S. 60-3)	2
	Attn: Spacecraft Technology Division	
	a. C. C. Conger (M.S. 54-1)	1
	b. F. Kavanagh (M.S. 54-3)	1
	c. D. Briehl (M.S. 54-3)	12
	Attn: Electric Propulsion Laboratory	
	a. W. Moeckel (M.S. 301-1)	1
	b. H. R. Kaufman (M.S. 301-1)	1
	c. J. Ferrante (M.S. 302-1)	1
	d. H. Monk (M.S. 301-1)	1
	e. G. Wise (M.S. 301-1)	1
	f. S. Obloy (M.S. 301-1)	1
	g. R. Steiner (M.S. 301-1)	1
	Attn: Report Control Office (M.S. 5-5)	1
3.	NASA Scientific and Technical Information Facility P. O. Box 33 College Park, Maryland 20740	
	Attn: NASA Representative RQT-2448	6
4.	NASA-Marshall Space Flight Center Huntsville, Alabama 35812	
	Attn: Ernest Stuhlinger (M-RP-DIR)	1
5.	Research and Technology Division Wright-Patterson AFB, OHIO 45433	
	Attn: AFAPL (APIE-2)/R. F. Cooper	1